INVESTIGATION ON THE SYNTHESIS AND CONDUCTIVITY MECHANISM OF GRAPHENE BASED ISOTROPIC CONDUCTIVE ADHESIVES

By

RICHARD ANG GIAP LENG

A dissertation submitted to the Department of Mechanical and Materials Engineering,
Lee Kong Chian Faculty of Engineering & Science,
Universiti Tunku Abdul Rahman
in partial fulfillment of the requirements for the degree of
Master of Engineering Science
December 2016

DEDICATION

Specially dedicated to Paktaulo, Alison, and Edwin.

ABSTRACT

INVESTIGATION ON THE SYNTHESIS AND CONDUCTIVITY MECHANISM OF GRAPHENE BASED ISOTROPIC CONDUCTIVE ADHESIVES

Richard Ang Giap Leng

Isotropic Conductive Adhesives (ICA) offer a promising alternative to conventional tin/lead solders which are prohibited under regulations such as the EU's Restriction of Hazardous Substances Directive (RoHS). This research effort investigates graphene based ICA as a novel interconnects solution for the electronic packaging and assembly industry. Graphene is a 2-dimensional carbon allotrope with superlative mechanical, electrical and thermal properties. It is intrinsically stronger than diamond and is electrically more conductive than copper. Graphene oxide (GO) was synthesized via Huang's method and then reduced with hydrazine via Stankovich's method to produce graphene or more precisely reduced graphene oxide (RGO) in the form of an agglomerated solid cake. The synthesized RGO samples were analysed with FTIR and XPS spectroscopy and confirmed with Raman spectroscopy and HRTEM imaging to be predominantly multiple layered graphene which contained lattice defects and heteroatomic impurities. Semi-wet RGO particles were dispersed by hand stirring in DGEBA epoxy resin and subjected to rheological flow and oscillatory experiments with the Anton Parr MCR301 rheometer. This innovative technique led to the finding that the liquid matrix is very stable and resistant to shear destruction and exhibited Newtonian like behaviour at low filler loadings below 4% weight but demonstrated a step wise rheological transformation displaying strong thixotropic behaviour at 4% loading. The samples were cured with EDA.

FESEM images of fractured sample surfaces successfully revealed the morphology of the network of conductive pathways formed by the dispersion of RGO particles. The electrical percolation threshold level was found to be 0.7% filler by weight at a bulk resistivity reading of 1.50E+05 Ω cm. With the minimum bulk resistivity extrapolated at 1.00E+01 Ω cm this value is still five orders in magnitude higher than that of Sn/Pb solder. Based on this finding, the RGO filled epoxy matrix is not conductive enough to be used as a replacement for Sn/Pb type solder.

ACKNOWLEDGEMENT

Firstly, I would like to express my gratitude to Universiti Tunku Abdul Rahman for granting the funds for this research effort.

To my supervisor Professor Dr Rajkumar Durairaj and co-supervisor Dr Chen Kah Pin, thank you very much for your vision, guidance and patience without which this project would not have come to fruition and completion. I am also especially grateful to Professor Dr Raj for giving me the chance to pursue my candidature at UTAR.

I would also like to express my appreciation to Mr. Lim Eng Cheong, Cik Sharifah, Mr. Khor, Puan Ros, Ms Chew Chee Sean, Ms Kang, Ms Heng, Ms Samantha and other helpful laboratory and administrative staff of Universiti Tunku Abdul Rahman for their assistance. Special mention goes out to Judson, Yuan Ling, and Cheow Hoong. Thanks for the memories.

Last but not least I am eternally grateful to my family and parents who supported me throughout the journey. Thanks for the love and encouragement.

APPROVAL SHEET

This dissertation entitled "**INVESTIGATION ON THE SYNTHESIS AND CONDUCTIVITY MECHANISM OF GRAPHENE BASED ISOTROPIC CONDUCTIVE ADHESIVES"** was prepared by RICHARD ANG GIAP LENG and submitted as partial fulfillment of the requirements for the degree of Master of Engineering Science at Universiti Tunku Abdul Rahman.

Approved by:

_____

(Prof. Dr. Rajkumar Durairaj)
Date:
Professor/Supervisor
Department of Mechanical and Materials Engineering
Lee Kong Chian Faculty of Engineering & Science
Universiti Tunku Abdul Rahman

_____

(Dr. Chen Kah Pin)
Date:
Assistant Professor/Co-supervisor
Department of Mechanical and Materials Engineering
Lee Kong Chian Faculty of Engineering & Science
Universiti Tunku Abdul Rahman

LEE KONG CHIAN FACULTY OF ENGINEERING & SCIENCE

UNIVERSITI TUNKU ABDUL RAHMAN

Date: _____

SUBMISSION OF DISSERTATION

It is hereby certified that Richard Ang Giap Leng (ID No: 13UEM08466) has completed this dissertation entitled "**INVESTIGATION ON THE SYNTHESIS AND CONDUCTIVITY MECHANISM OF GRAPHENE BASED ISOTROPIC CONDUCTIVE ADHESIVES**" under the supervision of Professor Dr. Rajkumar Durairaj from the Department of Mechanical and Materials Engineering, Lee Kong Chian Faculty of Engineering & Science, and Dr. Chen Kah Pin (Co-Supervisor) from the Department of Mechanical and Materials Engineering, Lee Kong Chian Faculty of Engineering & Science.

I understand that University will upload softcopy of my dissertation in pdf format into UTAR Institutional Repository, which may be made accessible to UTAR community and public.

Yours truly,

_____

(Richard Ang Giap Leng)

DECLARATION

I hereby declare that the dissertation is based on my original work except for quotations and citations which have been duly acknowledged. I also declare that it has not been previously or concurrently submitted for any other degree at UTAR or other institutions.

_____

Richard Ang Giap Leng

Date: _____

TABLE OF CONTENTS

LIST OF TABLES

LIST OF FIGURES

LIST OF ABBREVIATIONS AND NOTATIONS

3D	Three dimensional
Å	Angstrom
δ	Phase angle
δ	Loss tangent
γ	Strain
$\dot{\gamma}$	Shear rate
η	Viscosity
η^*	Dynamic viscosity
η'	Real viscosity
η''	Imaginary viscosity
θ	Wave incident angle
λ	Wavelength
π	Radian
π bond	Pi bond

ρ	Bulk resistivity
σ	Shear stress
σ bond	Sigma bond
φ	Phase volume
ω	Angular frequency of oscillation
Ω	Ohm
A	Area
ACA	Anisotropic conductive adhesive
Ag	Silver
Al	Aluminium
ATR	Attenuated total reflectance
C	Carbon
$C_2H_4(NH_2)_2$	Ethylenediamine
cm	Centimetre
CNT	Carbon nanotubes
C=O	Carbonyl
C-O-C	Epoxide

COOH	Carboxylic
Cu	Copper
CVD	Chemical vapour deposition
d	Crystal interplanar lattice distance
DGEBA	Diglycidyl ether of Bisphenol A
DLVO	Deryagin, Landau, Vewey, and Overbeek
DMF	Dimethylformamide
EC	European Commission
ECA	Electrically conductive adhesive
EDA	Ethylenediamine
EDX	Energy-dispersive x-ray
EEW	Epoxide equivalent weight
ESCA	Electron Spectroscopy for Chemical Analysis
EU	European Union
eV	Electronvolt
FESEM	Field effect scanning electron microscope
FTIR	Fourier transform infrared

G	Shear modulus of rigidity
l	Complex modulus
G'	Storage (elastic) modulus
G"	Loss modulus
GIC	Graphite intercalated compound
GO	Graphene oxide
GrO	Graphite oxide
H	Hydrogen
h	Height
H_2O_2	Hydrogen peroxide
H_2SO_4	Sulphuric acid
H_3PO_4	Phosphoric acid
HCL	Hydrochloric Acid
HNO_3	Nitric acid
HOPG	Highly oriented pyrolytic graphite
HRTEM	High resolution transmission electron microscope
hv	Energy (Planck's constant x frequency)

I	Intensity
iNEMI	International Electronics Manufacturing Initiative
IC	Integrated circuit
ICA	Isotropic Conductive Adhesive
Kα	K-alpha
$KClO_3$	Potassium chlorate
$KMnO_4$	Potassium permanganate
l	Length
LCD	Liquid crystal display
LPE	Liquid phase exfoliation
MIMOS	Malaysian Institute of Microelectronic Systems
MW	Molecular weight
N	Nitrogen
N	Number of layers
NH_2	Amine
N_2H_4	Hydrazine hydrate
NNI	National Nanotechnology Initiative

O	Oxygen
OH	Hydroxyl
Pa	Pascal
Pc	Percolation threshold
PCBA	Printed circuit board assembly
PET	Polyethylene terephthalate
phr	Parts by weight per hundred parts
R	Resistance of specimen
RGO	Reduced graphene oxide
RoHS 1	Restriction of Hazardous Substances Directive 2002/95/EC
RoHS 2	Restriction of Hazardous Substances Directive 2011/65/EU
SAED	Selected area electron diffraction
SAOS	Small amplitude oscillatory shear
SEM	Scanning electron microscope
Si	Silicon
SiC	Silicon carbide

SLG	Single layered graphene
Sn	Tin
Sn/Pb	Tin/lead
t	Time
TTS	Time-temperature superposition
UTAR	Universiti Tunku Abdul Rahman
UV-Vis	Ultraviolet-Visible
v	Velocity
WEEE	EU Waste Electrical and Electronic Directive 2012/19/EU
wt.	Weight
XPS	X-ray photoelectron spectroscopy
XRD	X-ray diffraction

CHAPTER 1

INTRODUCTION

1.1 Background and Research Rationale

Lead is a heavy metal found in basic tin/lead solder. It is a substance toxic to humans. The production processes involved in the usage of lead based solder and the ensuing user discarded electronic end-waste products are polluting to the environment. Isotropic Conductive Adhesives (ICAs) provide a potential lead-free and green alternative to eliminate this environmental hazard. For this research effort, graphene was synthesized and applied as the conductive filler in epoxy resin to form the ICA composite material under study. This is a novel approach and may offer a viable solder substitute for the microelectronics packaging and printed circuit board assembly (PCBA) industry.

1.1.1 Lead-Free Solder Initiative

Tin-lead (Sn/Pb) alloy is a fusible material used to join together metal objects. It is a class of solder material used primarily for attaching through-hole and surface mounted components to printed circuit boards at the advent of the electronics industry. The eutectic composition of Sn/Pb alloy is 63%/37% by mass with a melting point of 183 °C. This composition and variants thereof promote excellent joint wetting and provides the necessary electrical conductivity, tensile and shear strength required for the interconnection of

electronic components in the PCBA industry with years of proven field reliability (Kang, 1999).

Unfortunately lead is toxic. It is a heavy metal and accumulates in the body through inhalation or ingestion. Upon exposure, health deteriorates slowly due to damage to internal organs, bones, the brain and the central nervous system leading to death in some cases. Children are especially vulnerable to the toxicological effects of lead (Bellinger and Bellinger, 2006). From an occupational safety point of view, workers can be exposed to dangerous levels of lead during the manufacturing and production processes. Air, soil and ground water can also be contaminated with lead from commercially discharged waste and landfill leachate. Recognizing this as an important health and environmental issue, the European Union (EU) proceeded to constitute controls on the use and disposal of hazardous material in electrical and electronic goods. As a result, the Restriction of Hazardous Substances Directive 2002/95/EC (RoHS 1) and the EU Waste Electrical and Electronic Directive 2012/19/EU (WEEE) were enacted and came into effect on 1 July 2006 (RoHSGuide, 2015).

The RoHS1 directive prohibits (with some exceptions) the inclusion of significant quantities of lead and other scheduled toxic material for consumer electronics produced in the EU. RoHS1 was subsequently amended to Directive 2011/65/EU (RoHS 2) to include additional electrical and electronic equipment, cable and spare part which came into effect on 2 January 2013 (RoHSGuide, 2015). On the other hand the WEEE directive complements

RoHS 2 by setting the collection, treatment and recycling targets of waste materials for all types of electrical and electronic goods. This green initiative was introduced to handle both hazardous and non-hazardous (e.g. gold, platinum, tin, copper, cadmium etc.) materials contained in the waste equipment produced prior to the directive and those currently being produced by the industry. The producer of electrical and electronics goods are required by law to facilitate the collection and recycling of the waste equipment from both industrial and household sectors.

According to Lu and Wong (2000) the electrical and electronics industry together with interested researchers were already exploring lead-free alternatives such as Isotropic Conductive Adhesive (ICA) and lead-free solder alloy before the turn of the new millennium. The industry recognized the urgency of going lead-free even before RoHS1 and RoHS2 were enacted. The earliest promising lead-free solder based alloy formulation was developed at Ames Laboratory, Iowa State University (Miller and Anderson, et al., 1994). The formulated material was a Sn-Ag-Cu ternary alloy at a composition of 93.6%Sn-4.7%Ag-1.7%Cu (wt. %). The viability of this ternary alloy was corroborated by studies conducted by Lee (1997).

By the turn of the new millennium, numerous Japanese manufacturers had switched to Pb-free ternary alloy solder (Suganuma, 2002). The International Electronics Manufacturing Initiative (iNEMI) a not-for-profit, R&D consortium of approximately 100 leading electronics manufacturers, suppliers, associations, government agencies and universities reported that the

electronics assembly industry worldwide had largely approved the Sn-Ag-Cu ternary alloy Pb-free system because it offers a viable substitute to Sn-Pb alloy with good solderability and reliability performance even though some adaptations to flux formulation, soldering equipment and process parameters were required (Handwerker 2005).

1.1.2 Isotropic Conductive Adhesives (ICAs)

Isotropic Conductive Adhesives (ICAs) is a class of polymer based electrically conductive material filled with conductive particles which can offer a promising alternative to conventional tin-lead solders. ICAs are currently widely used as the bonding material for the die-attach process in semiconductor packaging and the manual rework of PCBA assemblies. The conductive filler used in such ICAs primarily consist of silver flakes (Sancaktar and Bai, 2011).

Lu and Tong et al. (1999) showed that silver filled ICA specimens only become electrically conductive upon reaching the percolation threshold (Pc) of filler loading by % weight (wt.) when silver flakes started to make physical contact. They also showed that after the specimens were cured bulk resistivity dropped and postulated that particle to particle contact resistance was lowered as a result of post cure shrinkage of the binder material.

ICA material is unlikely to supplant the Sn-Ag-Cu ternary alloy Pb-free solder because it is currently well established as the solder system used in

expensive dedicated production lines configured for the PCBA industry. There is also no risk of the industry running out of raw material because tin, silver, and copper are abundant metals. At the present state of development, ICAs stand a better chance to be adopted as a niche alternative where the higher temperature of processing Pb-free solder at a range of 220°C to 240 °C is undesirable because of the additional thermo-mechanical stresses induced for instance. It is still remotely possible that mainstream attention could swing back to ICA if the current Pb-free solder solution develops insurmountable reliability problems. It is worth noting that the industry could be running field trials. For example Bosch which has employed ICAs under harsh environmental conditions for many years has never published the comprehensive reliability data without which real world comparisons between ICA and solder cannot be made (Morris 2007).

The positive attributes offered by ICA are no lead usage, no tin whisker growth, no intermetallic formation, no galvanic corrosion, high resolution screen printing for ultra-fine pitch device mounting, bonding of non-solderable substrates, high elasticity, and it uses an environmentally friendly no-clean process. The two most serious disadvantages are resistance drift and poor drop-test survival (Morris 2007).

Non-metal conductive materials such as carbon nanotubes (CNT) and graphene are carbon allotropes which possess intrinsic electron mobility higher than that of silver and have recently drawn a lot of interest from

researchers studying their electrical efficacy as fillers in ICAs such as Santamaria and Munoz et al (2013).

1.1.3 Graphene

Graphene is a 2-dimensional crystalline lattice of graphite. In natural graphite, each atom-thin sheet of graphene is uniformly stacked unto another and weakly held together by non-binding van der Waal forces (Dreyer and Ruoff et al., 2010).

According to orbital hybridization theory, each carbon molecule within the lattice is joined to other atoms by three sp2 hybridized covalent sigma (σ) bonds and a non-hybridized pi (π) bond (Pauling, 1931). The atoms within the lattice are separated at 120 degree angles forming fused aromatic hexagonal planar rings arranged in the repeating pattern of cells in a honeycomb pattern. This trigonal planar electron orbital structure is required in order to minimize the repulsion forces between the bonded atoms according to valence pair electron shell repulsion (VPESR) theory (Gillespie, 2004).

Figure 1.1 illustrates the covalent bond structure between the carbon atoms within a single aromatic ring.

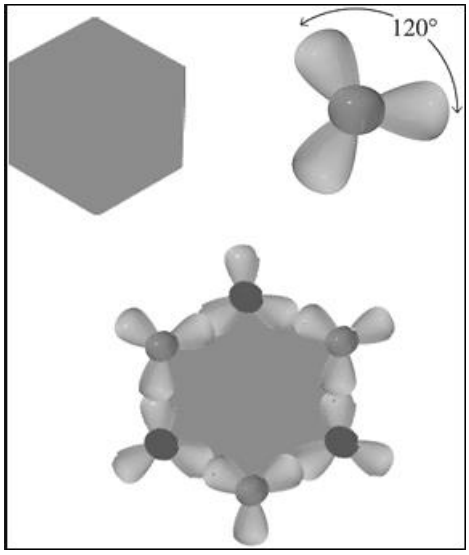

Figure 1.1: Sigma bonds arranged in-plane with an overlapping hexagonal structure per VSEPR model (Adapted from Biro and Nemes-Incze et al., 2012)

The remaining unhybridized π orbital from each atom are arranged perpendicularly to the basal plane thus forming non rotatable double bonds as shown in Figure 1.2.

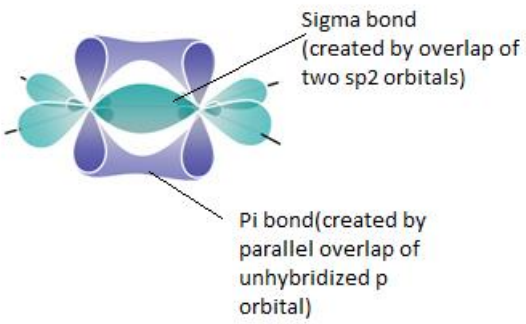

Figure 1.2: Schematic carbon double bond structure (Quora, 2015)

The conjugated double bonds allow the electrons in the valence shell to become delocalized making graphene an excellent thermal and electrical conductor. This is because pi electrons are not confined to a single double bond and can freely move to adjacent double bonds across groups of atoms. The cloud of mobile electrons can move along micron lengths of the lattice structure with virtually no scattering (unhindered by obstacles), a phenomenon known as ballistic transport (Areshkin and Gunlycke et al., 2007).

Peierls and Landau postulated from theory in 1937 that 2D crystals such as graphene could not exist because they were thermodynamically too unstable (Meyer and Geim et al., 2007). Their calculations showed that free standing large thin film of 2D crystal structures up to several layers thick degraded and eventually decomposed into small islands of disordered particles. Until Novoselov and Geim et al. (2004) isolated a single sheet of carbon from highly oriented pyrolytic graphite (HOPG) using their Scotch tape exfoliation method, it was conventional wisdom that this 2-dimensional structure could not exist. Due to a stroke of good luck, they applied the exfoliated graphene on a silicon wafer coated with a 300 nm of SiO_2 that was simply lying around in the laboratory and discovered that the otherwise invisible single-layered graphene could be seen when viewed under a conventional optical microscope.

When Meyer and Geim et al. (2007) successfully suspended single layered graphene sheets on the metalized strips of silicon substrates, they produced a material which confirmed that a free-standing single layer of

graphene membrane was indeed stable even though the edges were slightly curled and folded as shown in Figure 1.3.

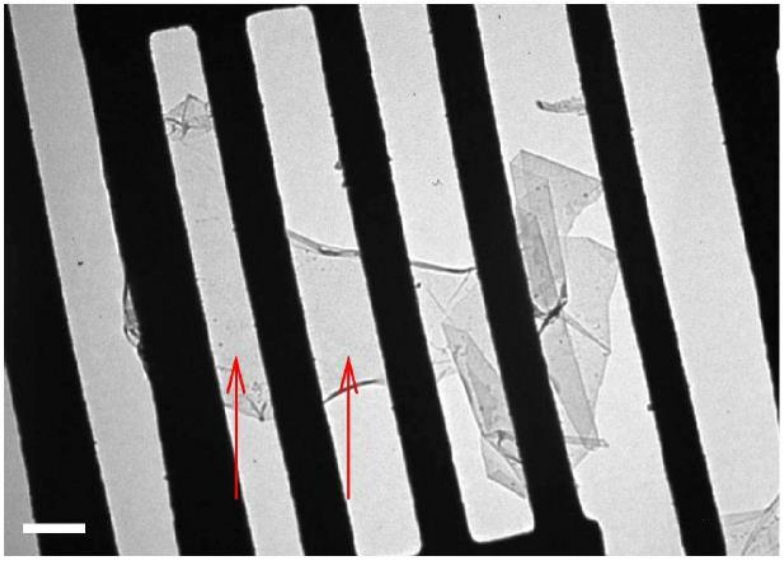

Figure 1.3: Bright field TEM image of suspended single-layered graphene. Arrows point to the relatively flat central region in comparison to the scrolled top and bottom edges and strongly folded regions on the right. Scale bar 500 nm. (Adapted from Meyer and Geim et al., 2007)

They then postulated that "microscopic corrugations" or the slight rippling of the graphene surfaces explained why free-standing graphene need not necessarily buckle or collapse into three dimensional objects. Figure 1.4 is a computer generated model showing the ripples and corrugations of the central region pointed out by the arrows in Figure 1.3.

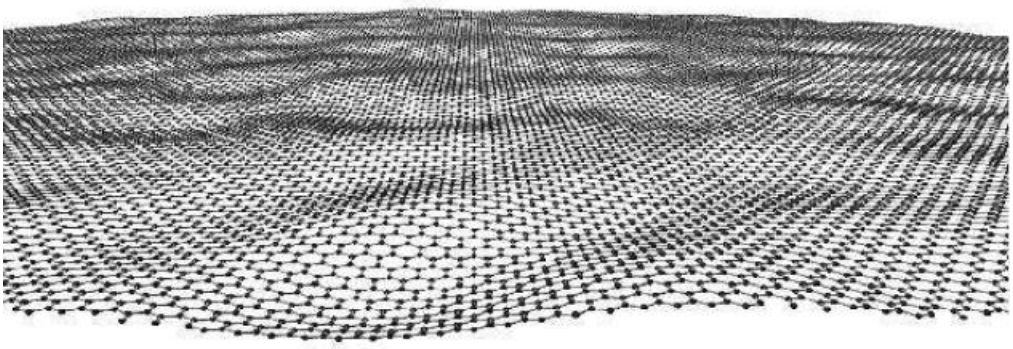

Figure 1.4: Computer model of the crumpled and corrugated structure of free standing graphene (Adapted from Meyer and Geim et al., 2007)

Graphene has superlative electrical properties. Experimental studies by Novoselov and Geim et al. (2004) showed that graphene exhibited typical electron mobility values of between 3,000 and 10,000 $cm^2/(V\ s)$. Since then Bolotin (2008) achieved experimental values in excess of 200,000 $cm^2/(V\ s)$.

1.2 Research Scope

Graphene can be produced via chemical vapour deposition (CVD), micromechanical cleavage, chemical reduction of graphene oxide (GO), and other methods according to Geim and Novoselov (2007). For this research effort, the wet process of oxidizing natural graphite flakes into GO and subsequently converting it to reduced graphene oxide (RGO) by chemical reduction was chosen because the process is high yielding and more importantly is scalable whilst the raw material used were inexpensive and the required equipment were mostly available within the university. Cost of the

sample characterization services from external parties like high resolution transmission electron microscopy (HRTEM) and Raman spectroscopy also fell within the allocated budget.

DGEBA was selected as the binder material due to its good bonding strength, thermal stability, low temperature processing ability and chemical resistance property (Skeist, 2012; Suganuma, 2002).

Laboratory work started with the synthesis of GO followed by its reduction to graphene after which a number of essential characterization tests were performed to confirm the presence of GO and graphene. The synthesized graphene were then blended with DGEBA epoxy resin and uncured liquid composite samples were subjected to rheological tests to study the dispersion stability of the graphene filled suspensions. The samples were mixed with ethylenediamine (EDA), oven cured and examined with an electron microscope. The bulk resistivity readings of samples at various filler loadings were measured to identify the electrical percolation threshold. Figure 1.5 summarizes the scope of this research effort along with the major milestones.

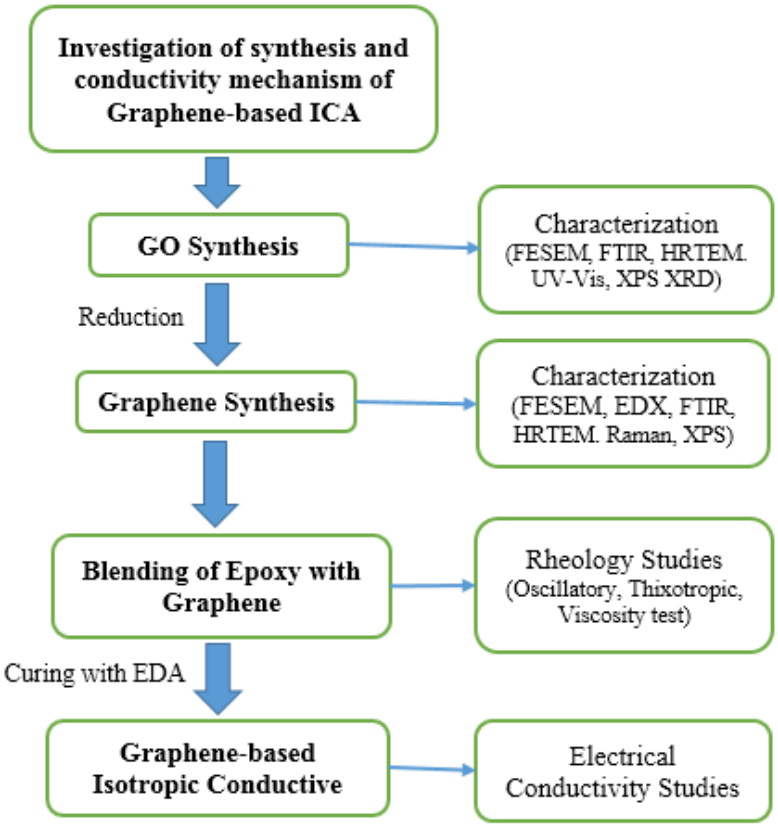

Figure 1.5: Flow chart of key research milestones

1.3 Aim and Objectives

The aim of this research effort is to synthesize and disperse graphene as the filler in epoxy resin to study the electrical property of ICAs as a Pb-free alternative for the electronics industry. The objectives of the research effort are:

a) To convert the insulating graphite oxide to graphene through a chemical reduction method

b) To investigate the dispersion behaviour of graphene in DGEBA epoxy resin

c) To investigate the electrical percolation threshold of graphene based isotropic conductive adhesives (ICAs)

CHAPTER 2

LITERATURE REVIEW

2.1 Electrically Conductive Adhesives

Electrically conductive adhesives (ECAs) are electrical insulators filled with particles of electrically conducting material. ECA composites can be further divided into anisotropic conductive adhesives (ACAs) and isotropic conductive adhesives (ICAs). Figure 2.1 illustrates the various solutions employed for achieving electrical interconnection in the semiconductor and electronics assembly industry.

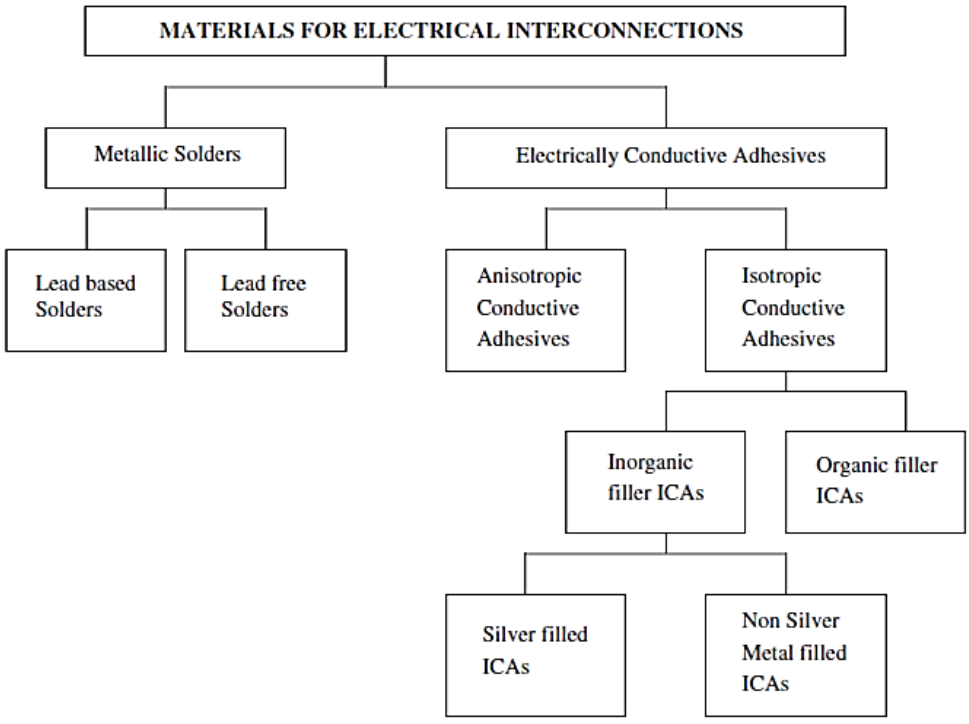

Figure 2.1: Materials used for electrical interconnections (Adapted from Mir and Kumar, 2008)

Epoxies, acrylics, urethanes and silicones are some examples of polymer binders which also play the role of the carrier vehicle for the conductive fillers in ECAs. Polymer adhesives are nonconductive because they have strong dielectric properties. Hence metallic particles such as silver, gold, copper, nickel, and indium are traditionally added to function as the conductive portion of the ECA matrix.

ACAs are designed to conduct electricity in one direction, out of the x-y plane in the z direction only. To achieve this, the liquid polymer or polymer film is loaded with an amount of micron-sized metallic particles below isotropicity (around 5% weight to 10% weight) to prevent the particles from coming into contact with one another in the x-axis and y-axis, but yet move close enough to each other to make physical contact to form a conductive pathway in the z-axis once compressive force is applied in the same direction (Mir and Kumar, 2008). Foam adhesive tapes inserted with isolated parallel strips of conducting metals arranged in the direction of the z-axis is another variant of ACA. ACAs are used extensively to assemble liquid crystal displays (LCDs) in tape automated bonding packages, to connect liquid crystal display panels to printed circuit boards (PCB) and for flip chip bonding in the semiconductor assembly industry (Li and Wong, 2006)

Also known as polymer solders, ICAs conduct electricity in all directions primarily due to the presence of a three dimensional network of conductive particles dispersed within the insulative binder material. The resistance to electrical flow of an ICA is an intensive material property and

can thus be measured in terms of bulk (or volume) resistivity ρ, as shown in Figure 2.2 where:

$$\rho = \frac{RA}{l} \tag{2.1}$$

where ρ = bulk resistivity (Ω cm)

R = resistance of specimen (Ω)

A = cross-sectional area of specimen (cm^2)

l = length of specimen (cm)

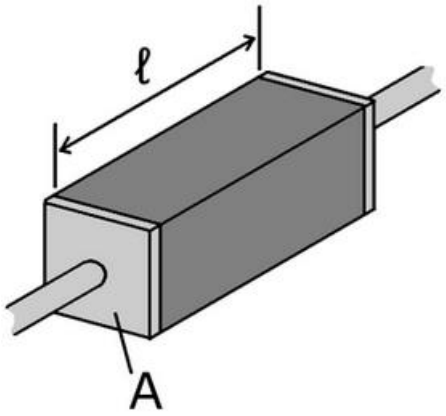

Figure 2.2: A specimen placed between two electrical contacts (Adapted from Creative Commons, 2015)

The filler concentration upon which the insulating polymer matrix becomes electrically conductive is called the percolation threshold. Increasing the filler concentration beyond this critical level will bring about an increase in conductivity only to precipitously level off at a plateau. ICAs are being widely

applied as die attach adhesive for integrated circuit (IC) chip mounting, conductive inks, thermoplastic pastes for electrostatic discharge protection, and flip chip bonding. The relevant benefits and drawbacks of epoxy type ICAs compared to Sn/Pb based solders are listed in Table 2.1.

Table 2.1: Benefits and drawbacks of epoxy type ICAs (Mir and Kumar, 2006; Morris, 2007; Li and Lu et al., 2009)

Aspect	Benefits	Drawbacks
Health and Environment	No Pb Flux free no-wash process	
Performance	Fair mechanical strength High adhesion strength Low processing temperature	Moderate heat dissipation Low current carrying capacity
During Production	Low thermal stress Ultra-fine pitch SMT Elimination of PCB solder mask No solder balls defects	Poor impact strength
Reliability		Contact resistance drift

Diglycidyl ether of Bisphenol A (DGEBA) epoxy resin was chosen as the binder for this research project due to the numerous benefits conferred by epoxy resins as summarized in Table 2.1. Even though the mechanical performance especially in terms of low impact strength (drop test survival rate was poor) and unstable contact resistance in past studies (Li and Wong, 2006)

have diminished the viability of ICAs, studies conducted by Du and Cheng (2012) produced encouraging performance improvements when graphene and carbon nanotube (CNT) were added as fillers across a variety of polymer binders including epoxy resins. Ultimately, the DGEBA based ICA is still a meaningful test vehicle for the purpose of the rheology and conductivity experimental studies designed for this research effort. Table 2.2 contrasts the important characteristics of a commercial Ag filled ICA versus Sn/Pb solder. Note that the volume (bulk) resistivity for ICA is thirty times higher than Sn/Pb solder.

Table 2.2: Comparison of generic commercial ICA with Sn/Pb solder (Adapted from Wong and Moon et al., 2010)

Characteristic	Sn/Pb Solder	ECA (ICA)
Volume Resistivity	0.000015 Ω cm	0.00035 Ω cm
Typical Junction R	10-15 mW	<25 mW
Thermal Conductivity	30 W/m-deg.K	3.5 W/m-deg.K
Shear Strength	2200 psi	2000 psi
Finest Pitch	300 µm	<150-200 µm
Minimum Processing Temperature	215 ^{o}C	<150-200 ^{o}C
Environmental Impact	Negative	Very minor
Thermal Fatigue	Yes	Minimal

2.2 Nanotechnology, Nanomaterials and Graphene

The National Nanotechnology Initiative (NNI) is a U.S. government backed research and development program and defines nanotechnology as: a science, engineering, and technology conducted at the nanoscale, which is about 1 to

100 nanometres (NNI, 2015). Since the inception of the NNI in 2001 cumulative budgeted funding from participating federal agencies totalled USD 21 billion (NSTC/CoT/NSET, 2014). Along with the U.S. government the importance of nanotechnology has also been recognised by the EU with the creation of the European Commission (EC) funded Nanofutures community organised under the European Technology Integrating and Innovation Platform (Nanofutures, 2015).

Nanomaterials feature prominently in the world of nanotechnology. For this dissertation, nanomaterials are defined as naturally occurring or man-made structures which contain at least one dimension below 100 nm. Figure 2.3 is an illustration of various objects and their relative sizes in comparison to the scale of some natural and man-made nanomaterials.

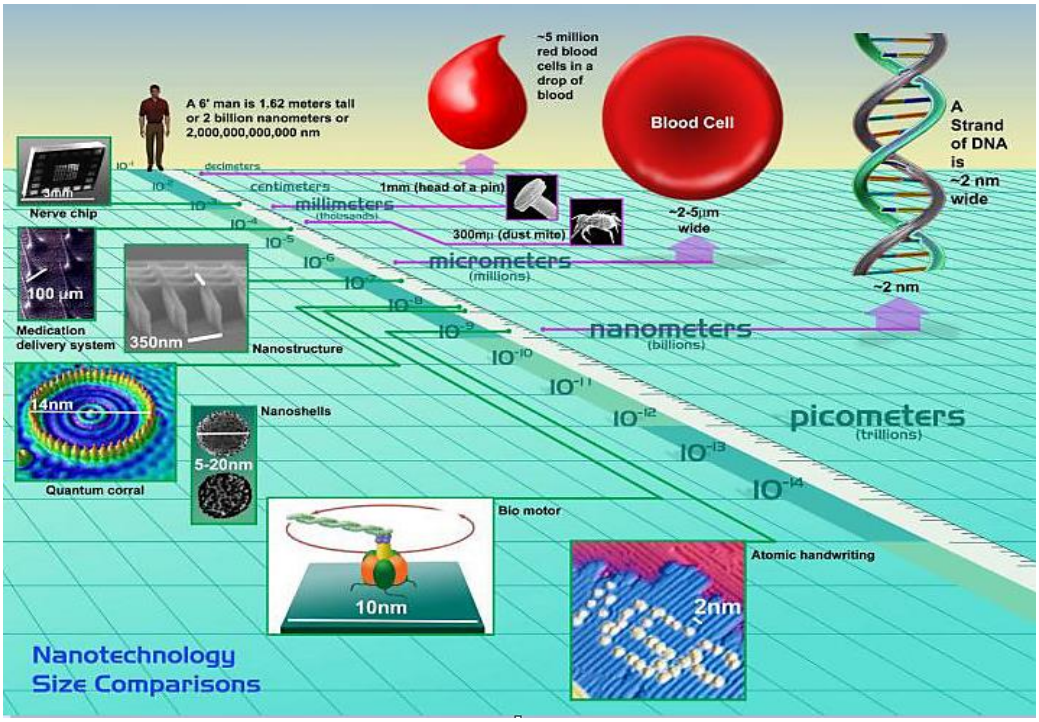

Figure 2.3: Size of nanomaterials in comparison with larger scaled objects (University of Montana, 2015)

Nanomaterials display emergent properties not seen in their bulk form due to surface and quantum effects as a result of their incredibly large surface-to-volume ratio and also due to their extremely small sizes. Graphene is a single crystalline layer of normally stacked planar graphite sheets (Roduner, 2006). It is a nanomaterial because it is only one carbon atom thick. Figure 2.4 illustrates the structural dimensions and the stacking arrangements of graphene layers in commercially available natural graphite. The ABAB sequence is the stacking structure of natural graphite even though about 10% of the material exists in the ABCABC sequence because according to Mukhopadhyay and Gupta (2012) the original ABAB stacking order were shifted by an additional layer as a result of being "subjected to high shear rates that result from milling or other industrial mechanical processes".

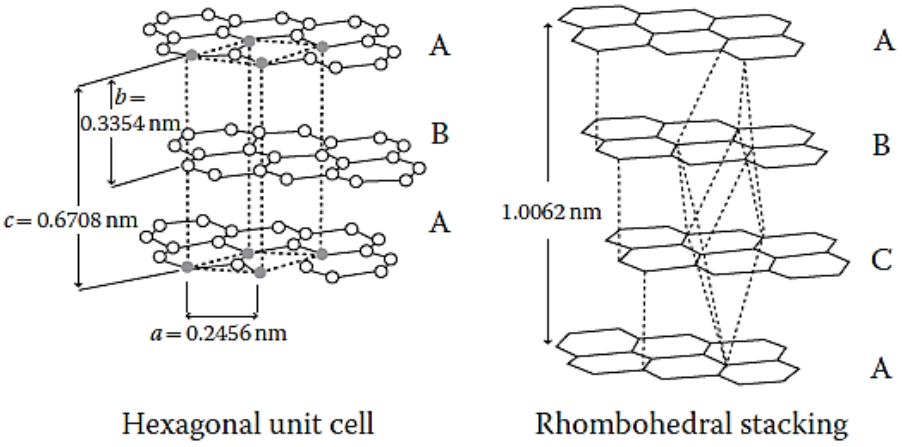

Figure 2.4: Hexagonal and rhombohedral packing of graphene layers in graphite (Adapted from Mukhopadhyay and Gupta, 2012)

When Novoselov and Geim et al. (2004) produced graphene they could only exfoliate microscopic sized particles using their novel Scotch tape

peeling method. Several years later Bae and Kim et al. (2010) reported the synthesis of roll-to-roll large sheets of graphene up to 30 inches long via chemical vapour deposition (CVD) on flexible copper substrates. Recently Kobayashi and Bando et al. (2013) managed to produce 230mm wide and 100m long rolls of CVD deposited graphene unto copper foil then laminated directly with epoxy resin coated polyethylene terephthalate (PET) films. Even though the direct synthesis of graphene on substrates by CVD has emerged as a viable large scale thin film coating tool, the yield is too low for any meaningful amount of graphene output. Other more practical means of graphene synthesis have to be used to produce enough material for the preparation of specimens required in this study and also by researchers elsewhere.

2.3 Graphene Synthesis

Since 2004, an explosion of interest and research activities was generated for the synthesis and application of graphene. Ferrari and Bonaccorso et al. (2015) listed and discussed all the known experimental methods developed to produce graphene up to the time their paper was published in 2014. Refer to Figure 2.5 below.

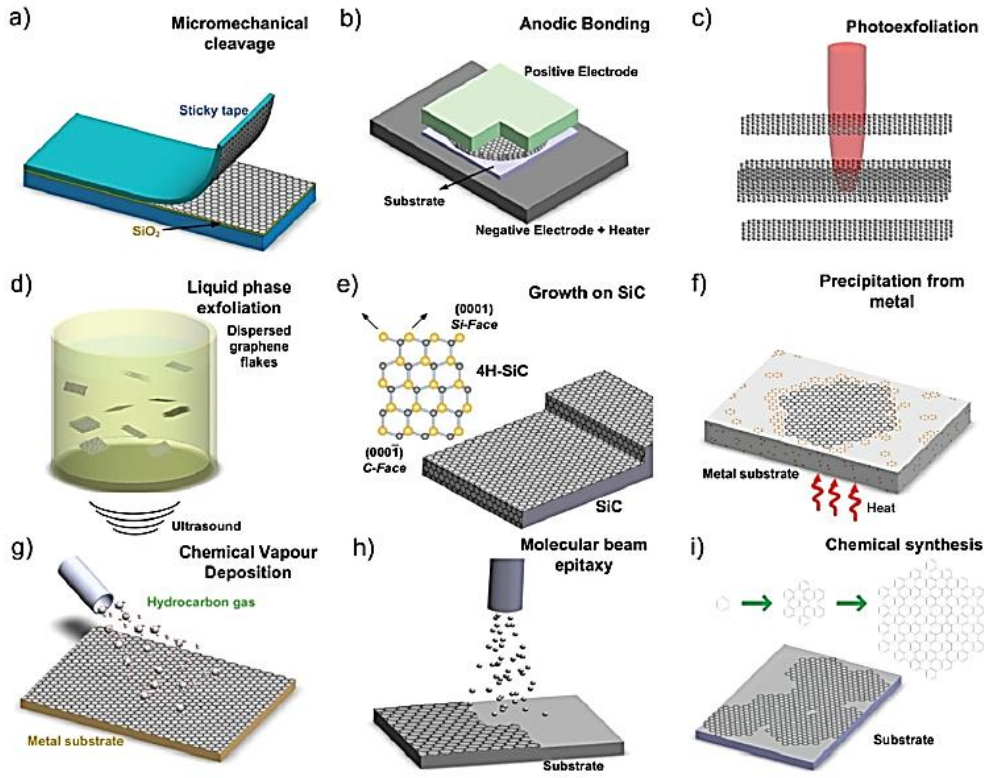

Figure 2.5: Schematic illustration of the main experimental setups for graphene production. (a) Micromechanical cleavage (b) Anodic bonding (c) Photoexfoliation (d) Liquid phase exfoliation. (e) Growth from SiC. Schematic structure of 4H-SiC and the growth of graphene on SiC substrate. Gold and grey spheres represent Si and C atoms, respectively. At elevated temperatures, Si atoms evaporate (arrows), leaving a C-rich surface tha forms graphene (f) Precipitation from carbon containing metal substrate (g) CVD process. (h) Molecular beam epitaxy. Different carbon sources and substrates (i.e. SiC, Si, etc.) can be exploited. (i) Chemical synthesis using benzene as building blocks. (Adapted from Ferrari and Bonaccorso et al., 2015)

The liquid phase exfoliation (LPE) route was selected to produce graphene used in this research effort because it is practical, inexpensive and most importantly yields enough material needed for the preparation of experimental specimens.

2.3.1 From Graphite to Graphite Oxide (GrO)

The LPE method is a top down process where individual layers of graphene are extracted from bulk natural graphite. This requires an intermediate step of first oxidizing graphite flakes to graphite oxide (GrO) to loosen the interlayer London dispersion forces - a type of van der Waals force formed by the instantaneous dipole–induced dipole interactions from the π electron orbitals - attaching the individual graphene layers together (Stankovich and Dikin et al., 2007; Dreyer and Ruoff et al., 2010).

Figure 2.6 is a schematic illustration of intercalant molecules interspaced in various staging formations within the original graphite layers resulting in a graphite intercalated compound (GIC) or GrO. For stage 1 outcomes - where the number 1 represents the staging index, single layered graphene (SLG) alternate with intercalant layers. For stage 2, double-layered graphene alternate with intercalant layers. In stage 3, triple-layered graphene alternate with intercalant layers. This staging arrangement can go beyond 3 layers up to any number of layers (N) depending on the LPE parameters used (Bonaccorso and Lombardo et al., 2012).

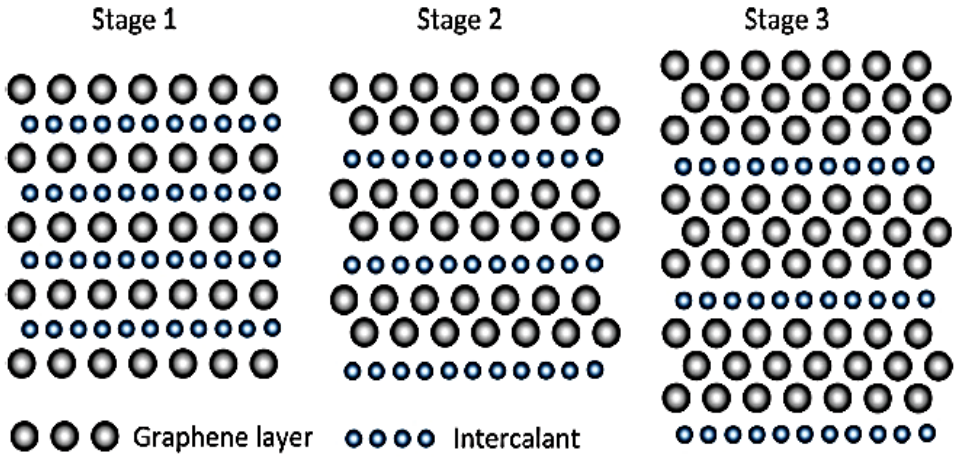

Figure 2.6: Schematic illustration of the stages 1, stage 2, and stage 3 GIC (Adapted from Bonaccorso and Lombardo et al., 2012)

2.3.2 From GrO to Graphene Oxide (GO)

The oxidation of graphite has seen a long history starting from Brodie (1859) who produced GrO by adding potassium chlorate ($KClO_3$) to a graphite slurry exposed to fuming nitric acid (HNO_3). Staudenmaier (1898) improved the process by adding $KClO_3$ in multiple aliquots over the course of the reaction all contained within a single vessel. In addition he mixed in sulphuric acid (H_2SO_4) to increase the acidity of the mixture (Dreyer and Park et al., 2010). Sixty years later Hummers and Offeman (1958) used an alternate oxidation method of reacting graphite with a mixture of potassium permanganate ($KMnO_4$) and concentrated H_2SO_4. This achieved the same level of oxidation whilst making the process much safer with the elimination of fuming HNO_3 thus avoiding the production of toxic and explosive gases. Since then, other researchers have developed slightly different methods. The method used in

this research project was developed by Huang and Lim et al. (2011) because the process is not only safer but also is an improvement over Hummers' method in that it requires less human attention and achieves a 100% conversion of graphite flakes to GrO.

Figure 2.7 illustrates the two major steps undertaken to produce graphene oxide (GO). Natural graphite is first intercalated with oxygen-containing functional groups in the wet oxidation process into GrO and when ultrasonicated will exfoliate into single sheets of GO.

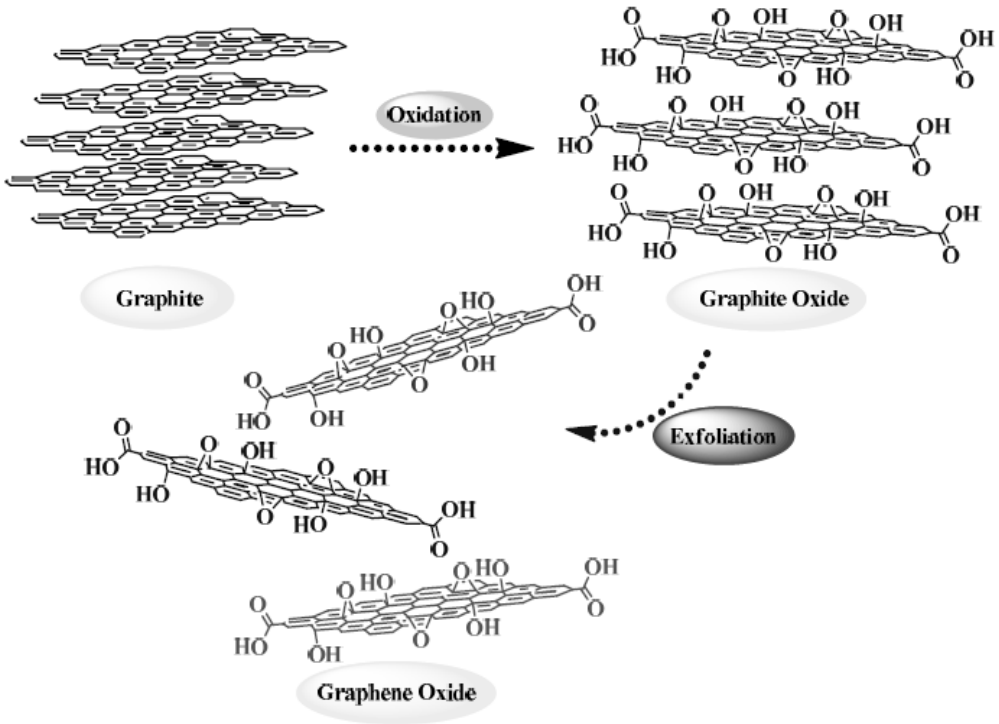

Figure 2.7: Schematic representation of the oxidation of graphite into stage 1 GrO and its exfoliation to GO (Garg and Bisht et al., 2014)

Stankovich (Stankovich and Dikin et al., 2007) suggested that the Lerf–Klinowski model (Lerf and He et al., 1998) provided a plausible description of GO particles as oxidized graphene sheets having their basal planes decorated mostly with epoxide (C-O-C) and hydroxyl (OH) groups, in addition to carbonyl (C=O) and carboxyl (COOH) groups located at the edges. Though the Lerf-Klinowski model was often reproduced by the research community (see Figure 2.7 for example), Dreyer and Park et al. (2010) stated that "the precise chemical structure of GO has been the subject of considerable debate over the years, and even to this day no unambiguous model exists." Even so, they observed that characterization techniques like Fourier transform infrared spectroscopy (FTIR) and X-ray photoelectron spectroscopy (XPS) have shed enough light to conclude the presence of epoxide, hydroxyl, carbonyl (C=O), and carboxylic (COOH) functional groups attached to the crystalline lattice of GO.

2.3.3 Reduced Graphene Oxide (RGO)

The final major step of the LPE route of graphene synthesis involves the reduction of GO. Strong reducing agents such as hydrazine and sodium borohydride are used to reduce GO to graphene (Huang and Lim et al., 2011). Dreyer and Ruoff et al. (2010) pointed out that graphene 'restored' in such a manner is referred to as reduced graphene oxide (RGO) in order to distinguish it from graphene produced via the other methods shown in Figure 2.5. The end product can be stored as either an RGO suspension in numerous solvents or as dried RGO powder or solid. This distinction to avoid using the term

'graphene' also hints to the fact that perfect RGO with a pristine hexagonal lattice structure free from oxygen-containing functional groups, heteroatomic contaminants, and edge defects have not been reported in any graphene related published literature. Bonaccorso and Lombardo et al. (2012) suggested a possible configuration of RGO as illustrated in Figure 2.8 below.

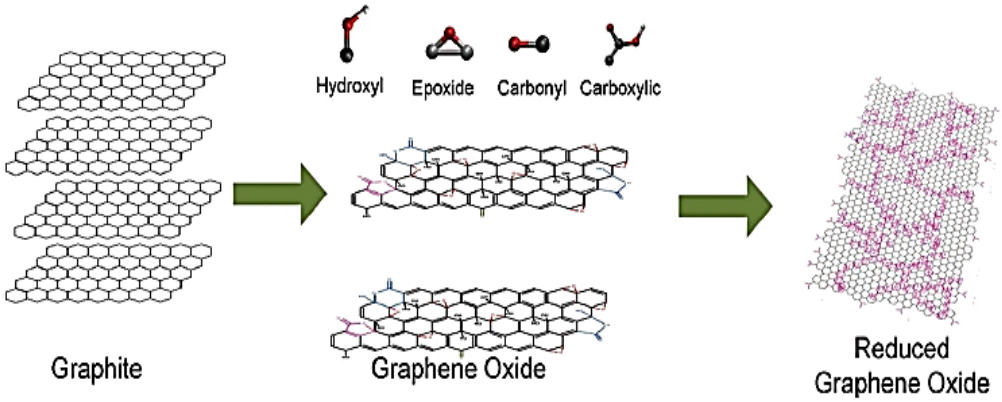

Figure 2.8: Schematic model of reduced graphene oxide (RGO) with residual oxygen-containing functional groups attached. Carbon, oxygen and hydrogen atoms are grey, red and white, respectively (Adapted from Bonaccorso and Lombardo et al., 2012)

Bagri and Mattevi (2010) proposed a more elaborate structure of the topological imperfections such as vacancies and lattice distortions found in thermally annealed RGO as shown in Figure 2.9.

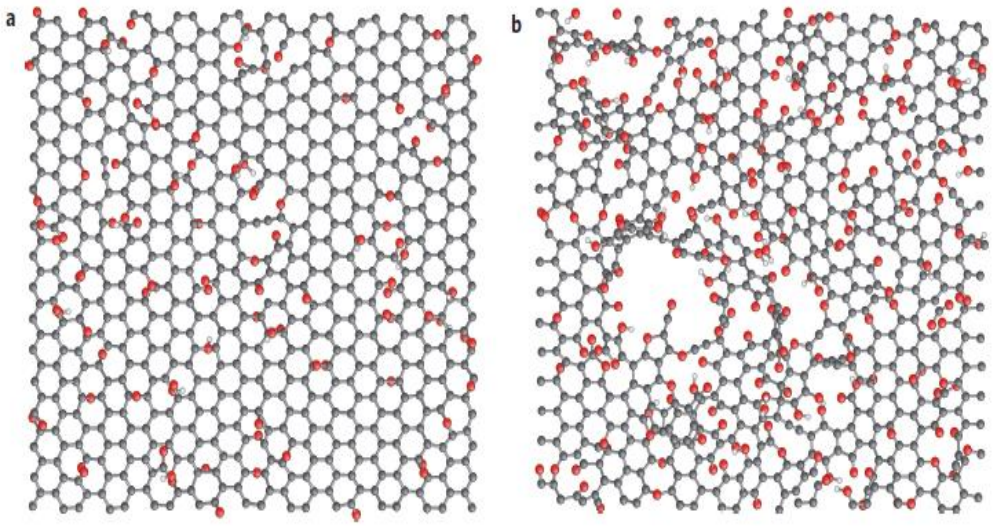

Figure 2.9: Reduced graphene oxide with residual oxygen concentration a) 20% b) 33%. Carbon, oxygen and hydrogen atoms are grey, red and white, respectively (Adapted from Bagri and Mattevi et al., 2010)

Even though the reduction of GO into RGO necessarily resulted in a myriad of defects, it is still the only scalable form of graphene production method yielding quantities sufficient enough for researchers interested in investigating the characteristics of graphene filled polymer matrices. Rajagopalan and Chung, (2014) used hydrazine as a reduction agent and reported residual oxygen-containing functional groups and nitrogen doped heteroatomic structures in the basal lattice of the synthesized RGO (refer to Figure 2.10).

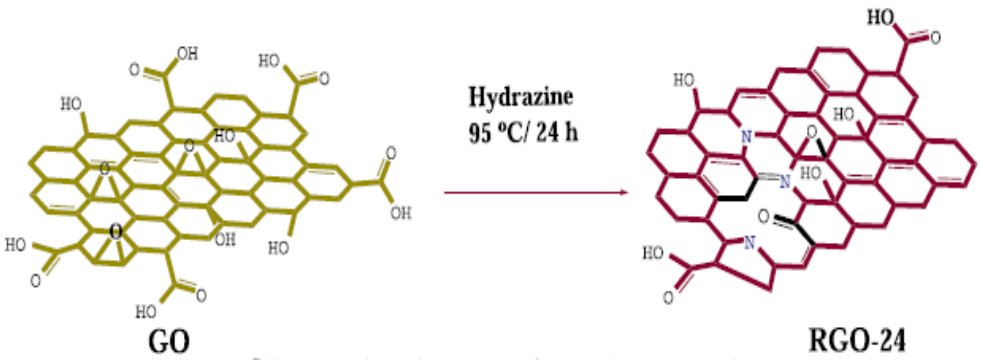

Figure 2.10: Schematic of GO to RGO synthesis via hydrazine reduction (Adapted from Rajagopalan and Chung, 2014)

In earlier experiments Stankovich and Dikin et al. (2007) and Marcano and Kosynkin et al. (2010) also used hydrazine as the reducing agent to produce graphene. They too reported the presence of residual oxygen-containing functional groups together with nitrogen atoms incorporated in the reduced end products. For this research effort the Stankovich method (Stankovich and Dikin et al., 2007) was chosen for the reduction of GO to RGO because the process published in their paper is practical and frequently cited by other researchers in this field such as Geim and Novoselov (2007).

2.4 Rheology of ICAs

The oven drying of RGO resulted in an end product in the form of a black coarse grainy powder (Stankovich and Dikin et al., 2007; Marcano and Kosynkin et al., 2010). When the particulate RGO is added into the liquid DGEBA epoxy adhesive to form the raw ICA, it is important to understand the nature of the mixture in terms of how the matrix behaves when shear stresses

are introduced during the blending process. For the case of this research effort, uncured specimens with varying weights of filler content are studied to determine their rheological characteristics in terms of how the RGO filler particles disperse within the epoxy binder material and affect the behaviour of the matrix under various deformation and shear conditions.

Rheology – a term coined by Professor Bingham of Lafayette College, Pennsylvania (Barnes and Hutton et al., 1989) is a branch of physical chemistry and the scientific study of the way matter deform and flow. Rheometry is the measuring technology used to obtain and analyze rheological data. The rheological properties of materials fall along a spectrum of two extremes; ideally viscous Newtonian fluids such as water on the one end and Hookean elastic solids such as rubber on the other extreme. Most naturally occuring substances such as blood or wet clay for example exhibit mechanical behavior with both viscous and elastic characteristics and are thus termed viscoelastic materials. Before considering the more complex viscoelastic behavior, let us first elucidate the flow properties of ideally viscous and ideally elastic materials.

2.4.1 Newtonian and Non-Newtonian Fluids

Fluid flow can be understood in terms of two basic types of relative movement - shear flow and extensional flow. According to Barnes (2000) adjacent particles move over or past each other in shear flow while the same particles

move towards or away from one another in extensional flow as shown in Figure 2.11.

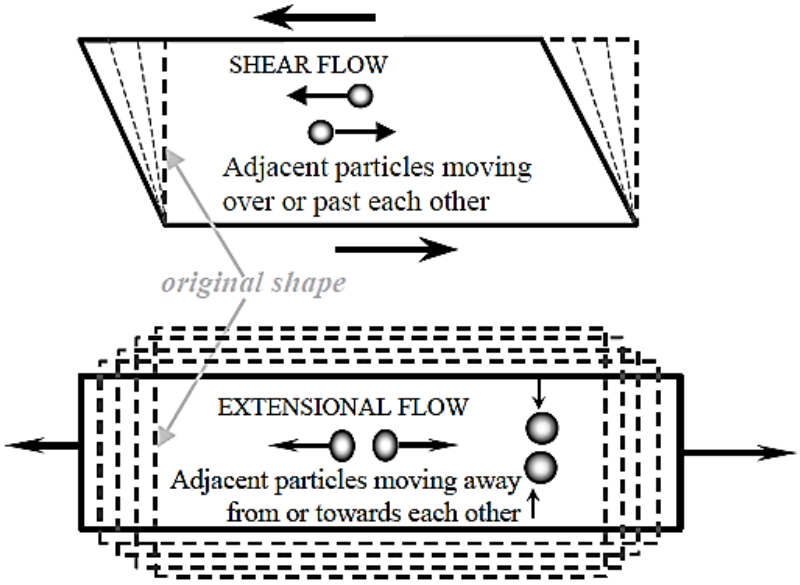

Figure 2.11: Particle motion in shear and extensional flows (Adapted from Barnes, 2000)

Viscosity is defined as a fluid's resistance to flow. For an ideally viscous fluid the shear flow rate of adjacent particles moving over or past each other vary in direct proportion to the shear stresses experienced. According to Willenbacher and Georgieva (2013), Isaac Newton described the viscosity (η) of an ideally viscous fluid as a constant of proportionality between the force per unit area or shear stress (σ) required to produce a steady simple shear flow and the resulting velocity gradient in the direction perpendicular to the flow direction or the shear rate ($\dot{\gamma}$) as shown in equation 2.2 and illustrated in Figure 2.12.

$$\sigma = \eta \dot{\gamma} \tag{2.2}$$

where σ = F/A is the shear stress (Pa)

$\dot{\gamma}$ = v/h is the velocity gradient or shear rate (s^{-1})

η = viscosity (Pa.s)

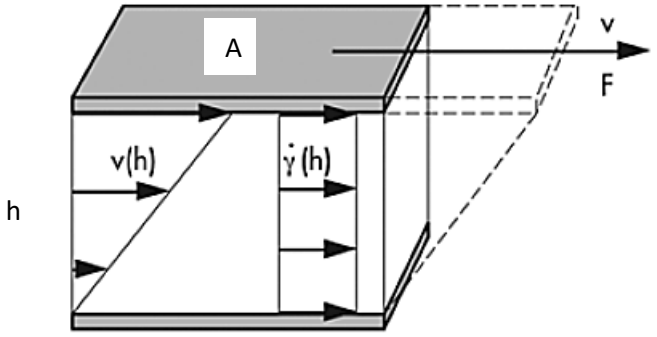

Figure 2.12: Ideally viscous fluid. Shear force F acting on the surface area A of the sheared fluid volume; h is the height of the volume element over which the fluid layer velocity v varies from its minimum to its maximum value (Adapted from Mezger, 2006)

Viscosity can thus be obtained by rearranging equation 2.2 yielding:

$$\eta = \sigma / \dot{\gamma} \tag{2.3}$$

A Newtonian fluid obeys the linear relation shown in equation 2.3 as illustrated in Figure 2.13.

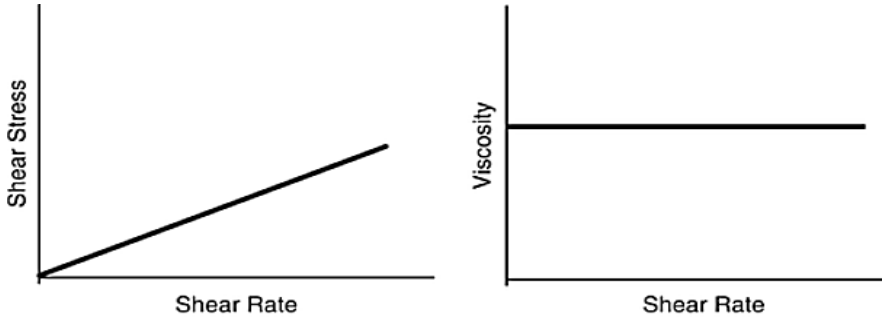

Figure 2.13: Newtonian fluid. Shear rate is directly proportional to shear stress and viscosity is constant and independent of shear rate

Furthermore, Newtonian behavior is also characterized by constant viscosity with respect to the duration of shearing and the immediate relaxation of the shear stress after cessation of flow. Subsequent shearing however long the period of rest between measurements will yield the same viscosity as previously measured.

Table 2.3 tabulates the approximate viscosities of some common Newtonian fluids measured at room temperature.

Table 2.3: Approximate viscosities of common Newtonian fluids (Adapted from Barnes, 2000)

Liquid or Gas	Approximate Viscosity (Pa.s)
Hydrogen	10^{-5}
Air	$2x10^{-5}$
Petrol	$3x10^{-4}$
Water	10^{-5}
Lubricating Oil	10^{-1}
Glycerol	1
Corn Syrup	10^{3}
Bitumen	10^{9}

An important point to take note of is that the temperature of specimens under study must be controlled because the viscosity of all simple liquids decrease with the increase in temperature. This can be largely explained by the increase in the Brownian motion of constituent molecules. In general the higher the viscosity, the greater is the rate of decrease in viscosity. For example, the viscosity of water decreases by about 3% per degree Celsius at room temperature, motor oils decrease by about 5% per degree while bitumens decrease by 15% or more per degree (Barnes, 2000).

At high enough shear rates all liquids exhibit non-Newtonian behaviour. For example, the values of the critical shear rates at which shear thinning a non-Newtonian behaviour begins to arise for glycerol and mineral oils are above 10^5 s^{-1}. Water would have to be sheared at an incredible 10^{12} s^{-1} to produce any non-Newtonian behaviour (Barnes, 2000). Figure 2.14 illustrates this phenomenon for the viscosity of a set of typical silicone oils.

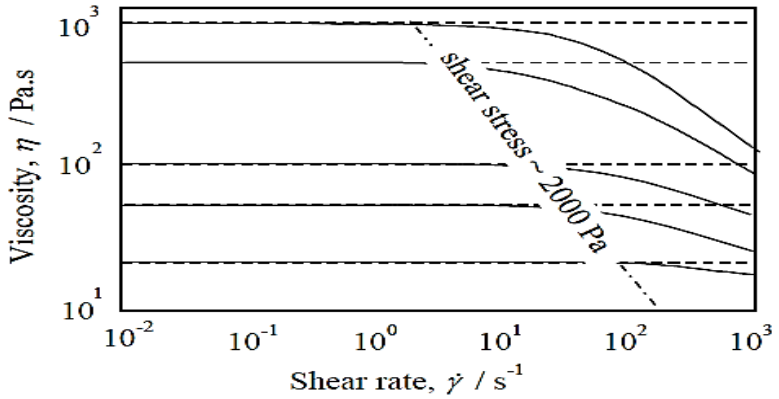

Figure 2.14: Flow curves for a series of silicone oils. Note the onset of non-Newtonian behaviour at a shear stress of ~ 2000 Pa (Barnes, 2000)

Extremely high shear rates notwithstanding, structured fluids such as suspensions, emulsions, dispersions and gels frequently exhibit flow properties distinctly different from Newtonian fluids and their viscosities may decrease or increase with increasing shear rate – behaviours which are described as shear thinning and shear thickening (dilatant) respectively. Figure 2.15 shows the general shape of a) shear stress and b) viscosity as functions of shear rate contrasting the behaviour of Newtonian fluids with non-Newtonian shear thinning and dilatant fluids.

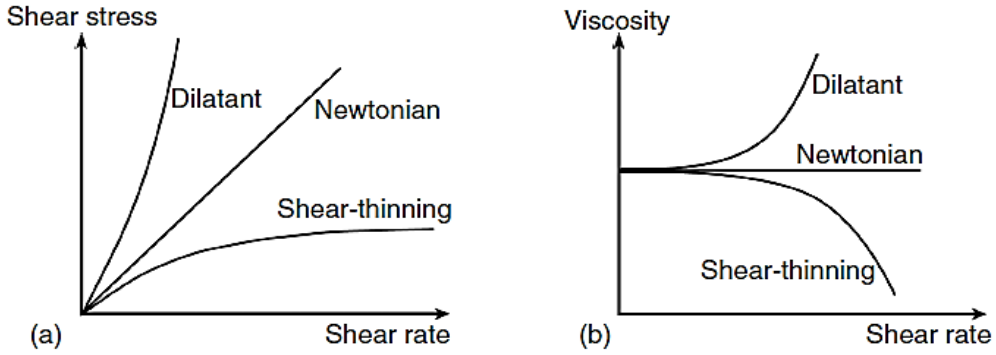

Figure 2.15: Flow curves for Newtonian, shear thinning and shear thickening (dilatant) fluids a) shear stress as a function of shear rate; (b) viscosity as a function of shear rate (Willenbacher and Georgieva, 2013)

2.4.2 Thixotropy and Viscoelastic Behaviour

When the behaviour of shear thinning fluids are measured across a wide enough shear rate, they typically undergo three distinct regions of viscosity changes as shown in Figure 2.16 (Barnes, 2000).

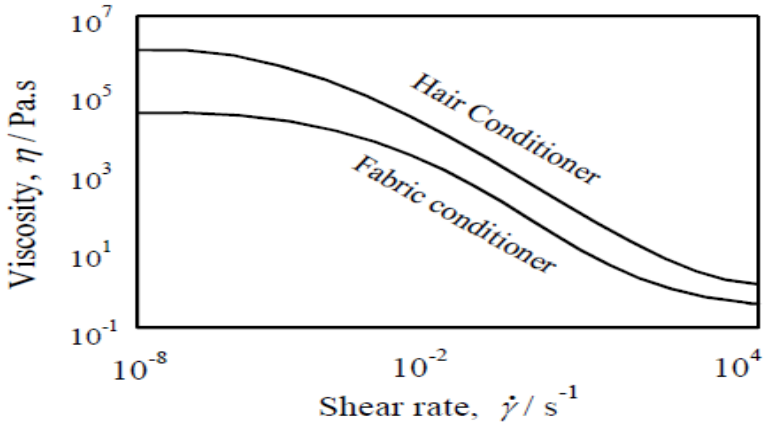

Figure 2.16: Viscosity curves of household products (Barnes, 2000)

From very low shear rates to low shear rates the viscosity is constant and upon increasing shear rates the viscosity will at some point begin to decrease steadily following which the viscosity will finally plateau into a second region of constant viscosity at higher shear rates.

Shear thinning is a common characteristic of structured fluids and can provide desirable attributes to a product, such as suspension stability in terms of not separating or drip resistance when at rest but ease of application when sufficient shear stress is applied. The typical shear rates encountered for some physical actions are shown in Table 2.4. For example the range of shear rates for hand mixing and machine stirring of a liquid epoxy blending operation can vary between 10^1 to 10^3 s^{-1}. Hence the shear thinning characteristics of structured fluids must be carefully matched with the shear rates encountered as the material is being processed and also during final application.

Table 2.4: Shear rate ranges of some physical actions (Adapted from Barnes, 2000)

Situation	Shear Rate Range (s^{-1})	Examples
Sedimentation of fine powders in liquids	10^{-6}–10^{-3}	Medicines, paint, salad dressings
Levelling due to surface tension	10^{-2}-10^{-1}	Paints, printing inks
Draining off surfaces under gravity	10^{-1}-10	Toilet bleaches, paints, coatings
Exturders	1-10^{2}	Polymers, foods, soft solids
Chewing and swallowing	10-10^{2}	Foods
Dip coating	10-10^{2}	Paints, confectionery
Mixing and stirring	10-10^{3}	Liquids manufacturing
Pipe flow	1-10^{3}	Pumping liquids, blood flow
Brushing	10^{3}-10^{4}	Painting
Rubbing	10^{4}-10^{5}	Skin creams, lotions
High speed coating	10^{4}-10^{6}	Paper manufacture
Spraying	10^{5}-10^{6}	Atomisation, spray drying
Lubrication	10^{3}-10^{7}	Bearings, engines

The viscosity of a material measured at very low shear rates is defined as the zero-shear viscosity and is effectively the viscosity while it is at rest. In the case of a suspension, a high zero-shear viscosity can play a vital role in inhibiting the sedimentation of dispersions or the creaming of emulsions.

Even as the behaviour of a substance to thin and flow under shear stress is desirable, it can also be a problem when the fluid is expected to stay in place after application. Consider the toothpaste. This ability of toothpaste to recover its original thickness is called thixotropy.

According to Barnes (1997), Schalek and Szegvari in 1923 found that aqueous iron oxide dispersions thinned out into liquid form from a gel state just by gentle shaking alone and the liquid would then solidify back to its original gel form over time. Peterfi then coined the term thixotropy to describe this particular time dependent material characteristic in a paper published in 1927. This breakdown or temporary destruction of the three dimensional (3D) structure of a thixotropic fluid can be imagined in a schematic shown in Figure 2.17.

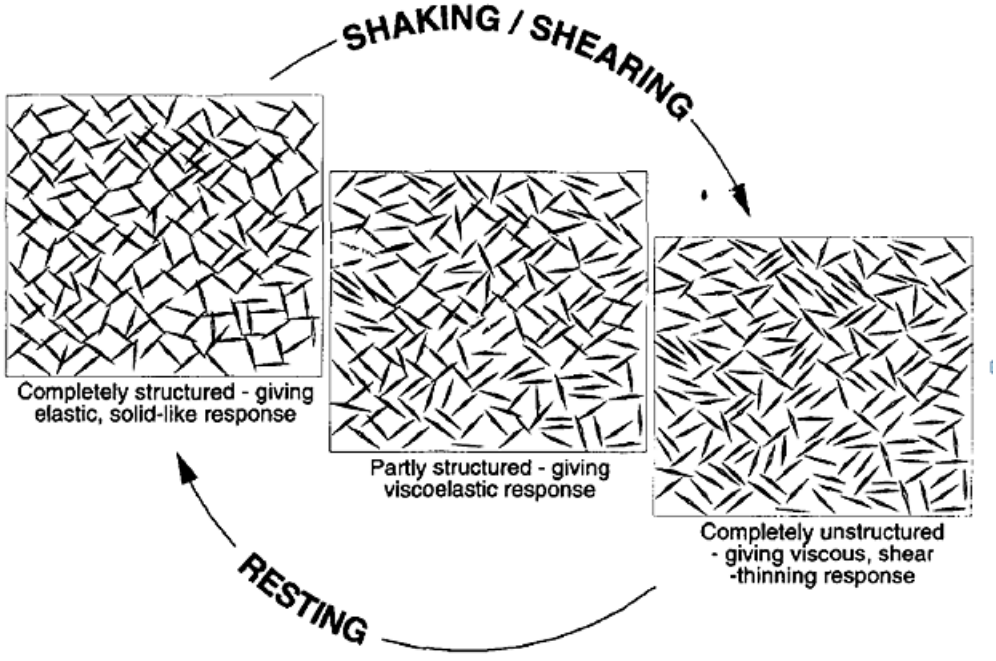

Figure 2.17: Shear destruction and recovery of 3D thixotropic structure (Adapted from Barnes, 1997)

As far as definitions go, the following passage cited directly from Barnes (1997) quoting Bauer and Collins in their 1967 review provides a good definition of thixotropy: "When a reduction in magnitude of rheological properties of a system, such as elastic modulus, yield stress, and viscosity, for example, occurs reversibly and isothermally with a distinct time, dependence on application of shear strain, the system is described as thixotropic". This definition together with the descriptions acccompanying the illustration of the process of shear breakdown shown in Figure 2.17 introduces three important ideas hitherto not discussed namely yield stress, viscoelastic response, and elastic modulus. These concepts together with other important rheological ideas will be reviewed in the sections to follow.

A material is viscoelastic when it displays elastic and viscous behaviour simultaneously when deformed. The elastic response of materials occuring under ideal shear deformation can be described by Hooke's law of elasticity for solids as shown in equation 2.4.

$$\sigma = G\gamma \tag{2.4}$$

where σ = shear stress (Pa)

γ = shear strain

G = shear modulus of rigidity (Pa)

The term 'viscoelasticity' is used to depict behaviour which falls between the ideal extremes of a Hookean elastic response and the Newtonian

viscous flow. The shear modulus of rigidity *G* for an ideal elastic solid is independent of the magnitude and duration of shear stress that it is subjected to. In other words when a deformation is applied, a corresponding stress is instantaneously sustained. However, in viscoelastic liquids stress relaxes gradually over time at constant deformation and will eventually vanish altogether. During an amplitude sweep oscillatory experiment (to be discussed further in a different section) when stress relaxation is proportional to strain, a zone known as the linear viscoelastic region can be identified. Above a critical strain the shear modulus becomes strain dependent going into the nonlinear viscoelastic region. The linear viscoelastic material properties are in general very sensitive to microstructural changes and interactions in structured fluids (Willenbacher and Georgieva, 2013).

In addition to the behaviour of viscoelastic materials described in the preceding paragraph, Barnes and Hutton (1989) pointed out that the particular response of a specimen in a given experiment depends on the time scale of the experiment. If the experiment is relatively slow, the specimen will appear to be viscous rather than elastic, whereas, if the experiment is relatively fast, it will appear to be elastic rather than viscous. At intermediate time-scales the viscoelastic response is observed.

The three distinct viscosity regions (first Newtonian plateau - power-law decrease - second Newtonian plateau) for hair and fabric conditioners illustrated in Figure 2.16 (section 2.4.3) exemplifies the nature of thixotropic fluids spanning from zero shear to very high shear rates. For the case of

suspensions containing solid particles, Barnes and Hutton (1989) extended this three region flow curve behaviour into a fourth region of increasing viscosity and attributed it to the amount of suspended material present in terms of the phase volume, φ (volume-per-volume fraction). φ is more important than weight-per-weight fraction because rheological behaviour is influenced largely by the hydrodynamic forces acting on the surface of particles or aggregates, irrespective of the particle density. The schematic of this general flow behaviour is shown in Figure 2.18.

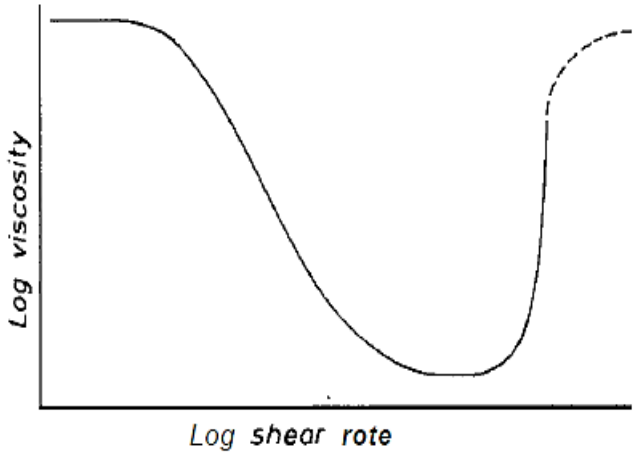

Figure 2.18: Flow curve for suspensions of solid particles (Adapted from Barnes and Hutton, 1989)

A non-Newtonian fluid with a yield stress is solid-like at rest. When applied shear stress is below the yield stress the material will deform elastically and when the yield stress is exceeded the same material will transform and start to flow like a liquid. This behaviour is clearly displayed by toothpaste being squeezed out of a tube. However, Barnes (1999) pointed out that materials exhibiting a 'true' yield stress with an infinite viscosity when approaching very low shear rates do not exist because "everything flows"

(*panta rhei* in latin) in long enough time scales. For example soft dispersions such as suspensions or emulsions often do not exhibit a true yield stress. From a Newtonian plateau at low shear stresses, they display a sudden drop in viscosity by orders of magnitude all within a narrow shear stress range termed an ‘‘apparent’’ yield stress $\sigma_{y,}$ measured at the midpoint of the viscosity curve downward slope as illustrated in Figure 2.19.

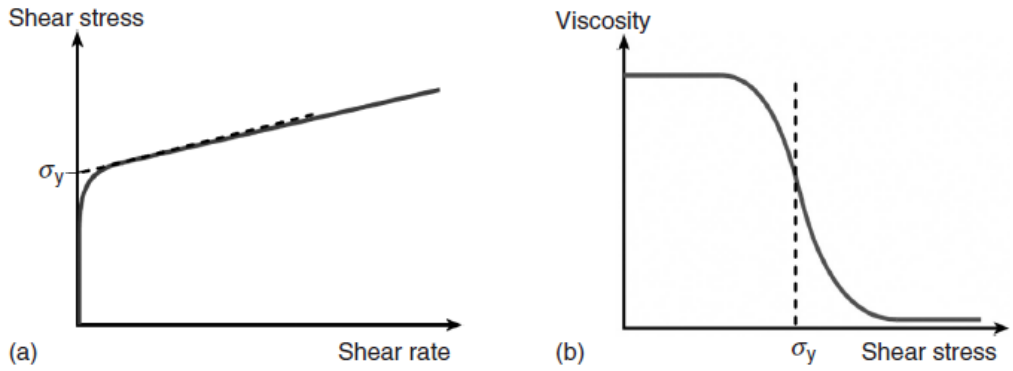

Figure 2.19: Flow curves of a material with an apparent yield stress σ_y : a) Shear stress as a function of shear rate; b) Viscosity as a function of shear stress (Adapted from Willenbacher and Georgieva, 2013)

Barnes’ observation about how everything flows in long enough time scales need not cause unduly concern because a ‘true’ yield stress can be identified with a rheometer capable of performing controlled shear rates experiments. As the concentration of suspended material increases in the dispersion, the very low to low shear rate viscosity plateau region disappears completely. The dispersion will only start to flow at a clearly identifiable yield point. An illustration of this yield-to-flow behaviour is shown in Figure 2.20 where obvious yield stresses can be measured for the viscosity curves at concentrations of 0.47% and 0.50% volume fraction of latex suspended in water. Note that the yield stress is exactly 1 Pa at 0.50% volume fraction.

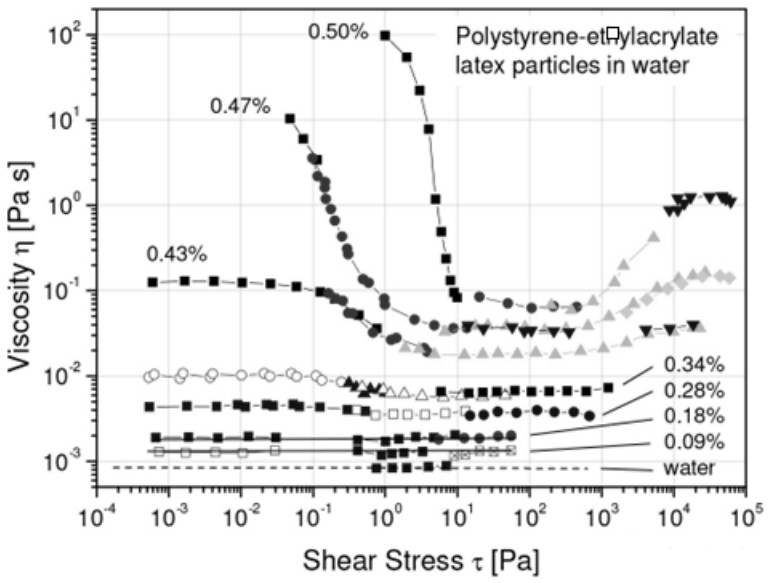

Figure 2.20: Viscosity of a structured fluid as a function of shear stress and particle concentration (Adapted from Franck, 2004)

Knowledge of how materials yield under shear forces is important because yield stresses can play a significant part in how the fluids can be properly processed and conveniently handled. In the food industry for example, the yield stresses of structured fluids like mayonnaise and ketchup are carefully engineered to allow them to be conveniently packed and made easily dispensable whilst their thixotropic properties permit them to flow and recover their original consistency when the completed dishes are ready to be served. This manipulation of yield stresses of man-made structured fluids is dependent on the type of forces acting on the particles suspended in the material. Firstly, the presence of heat causes atoms, molecules, nano-sized up to micron-sized particles to vibrate and with sufficient kinetic energy move around colliding randomly according to Brownian motion. Entropic repulsion forces can arise from electrostatic charges or from the steric repulsion of polymeric or surfactant molecules on particle surfaces. On the other hand intermolecular attraction arises from van der Waals-London forces. According

to the DLVO theory (name after Deryagin, Landau, Vewey, and Overbeek), a net energy barrier exists as a result of the combination of attractive and repulsive forces resisting particles from approaching each other closely (Thomas and Judd, et al., 1999). As long as the kinetic energy of particles did not exceed their energy barrier, agglomeration should not occur (Duffy and Hill, 2011). This phenomenon is illustrated in Figure 2.21. When particle sizes are large enough, gravity force come into effect and sedimentation may be induced for above micron-sized particles or coagulates.

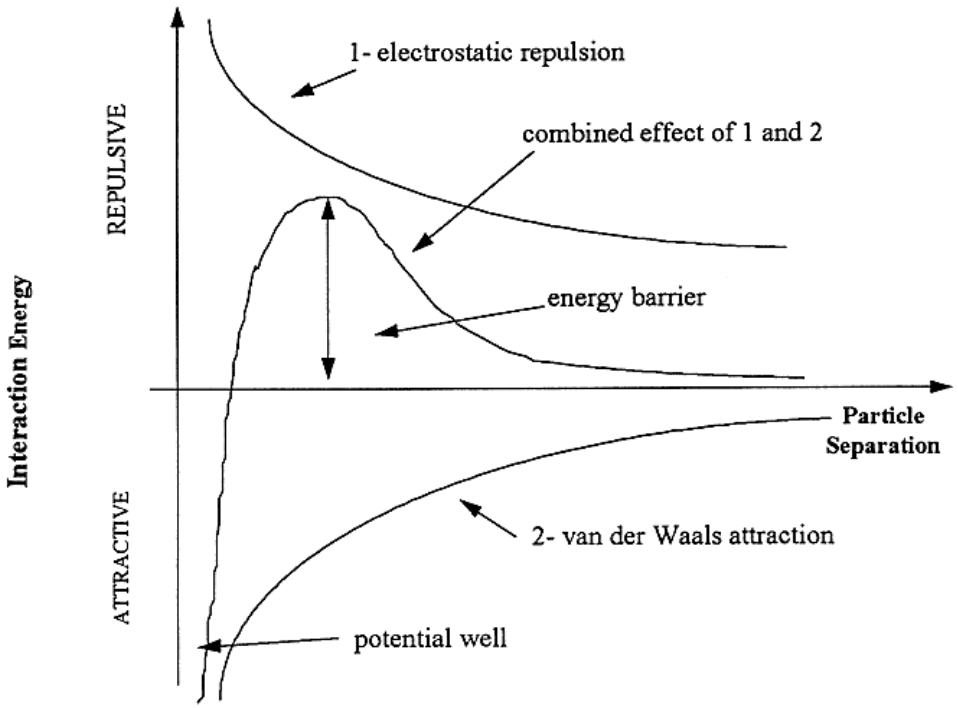

Figure 2.21: Schematic representation of DLVO theory (Adapted from Thomas and Judd, et al., 1999)

Besides the thermodynamic and microstructural factors discussed so far, viscoelastic properties of a fluid are also affected by hydrodynamic forces occurring during flow. The presence of isolated particles for example causes deviation of the fluid flow lines and leads to the increase of viscosity. At higher concentrations resistance increases further because particles collide when they are pushed and have to get out of each other's way. When particles agglomerate, even more resistance is encountered because the aggregates enclose and thus immobilise some of the continuous phase fluids.

2.4.3 Rheometry

In a nutshell rheology is the science of deformation and flow. Rheometry is the process of measuring the rheological behaviour of materials. Viscometers and rheometers are commonly used in research laboratories and industrial operations for making rheological measurements. It is important to note that a rotational instrument used for laboratory research purposes be able to perform controlled shear rate and controlled shear stress measurements (such as the Anton Parr MCR 301 used in this research effort) in order to characterize materials in both flow and oscillatory shear deformation.

Structured liquids have a natural rest condition where the microstructures exist in a minimum-energy state. Under deformation, movement from the rest state produces a certain amount of energy storage, which manifests itself as an elastic force trying to recover the minimum-energy level analogous to a stretched spring trying to return to its original

length. This kind of thermodynamic energy accounts for the elasticity seen in structured liquids and occurs simultaneously with the energy lost due to viscous flow for viscoelastic materials (Barnes, 2000).

In section 2.4.2 we discusssed how flow rheology is used to determine yield stress and also generate useful insights into the shear thinning behaviour of viscoelastic materials such as silicone oils (refer to Figure 2.14). In addition, flow studies can also reveal the extent of the time-dependent viscosity characteristics seen in thixotropic fluids in the form of a hysteresis loop as shown in Figure 2.22.

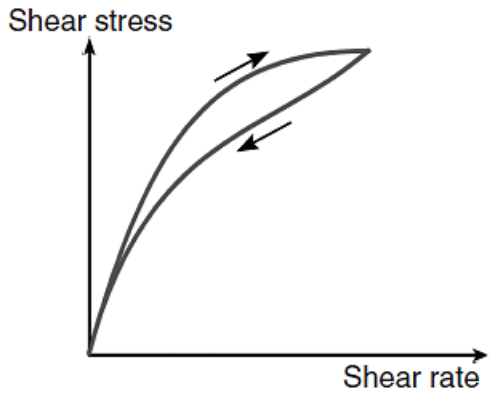

Figure 2.22: Schematic hysteresis loop of thixotropic material

Oscillatory rheology on the other hand allows the user to resolve the simultaneous elastic-like and the viscous-like properties of a material into separate behaviours, i.e. the storage (elastic) modulus *G'* and the loss modulus *G"*. It is thus a valuable tool for understanding the structural and dynamic properties of structured fluids. According to Willenbacher and Georgieva

(2013) a small amplitude oscillatory shear (SAOS) experiment is a widely used rheological measurement due to its accuracy.

When a sinusoidal oscillatory shear strain is applied, the time dependent deformation $\gamma(t)$ can be written as:

$$\gamma(t) = \gamma \sin(\omega t) \tag{2.5}$$

where t = time (s)

ω = angular frequency of oscillation (radian/s)

γ = shear strain

A viscoelastic fluid reacts to shear deformation with a sinusoidal shear stress $\sigma(t)$ response that is phase-shifted by an angle δ:

$$\sigma(t) = \sigma_0 \sin(\omega t + \delta) \tag{2.6}$$

where δ = phase angle (radian)

On the one extreme, the phase angle δ is zero for a perfectly elastic or Hookean material in that shear stress occurs instantaneously when strain is applied. On the other hand, δ is shifted by $\pi/2$ radians for a perfectly viscous or Newtonian fluid due to the time lag occuring between imposed strain and the corresponding stress response. The phase angle lies within these two boundary values for viscoelastic fluids because they contain within them both

in-phase and out-of-phase responses. These three types of oscillatory stress responses are shown graphically in Figure 2.23 (Weitz and Wyss et al., 2007).

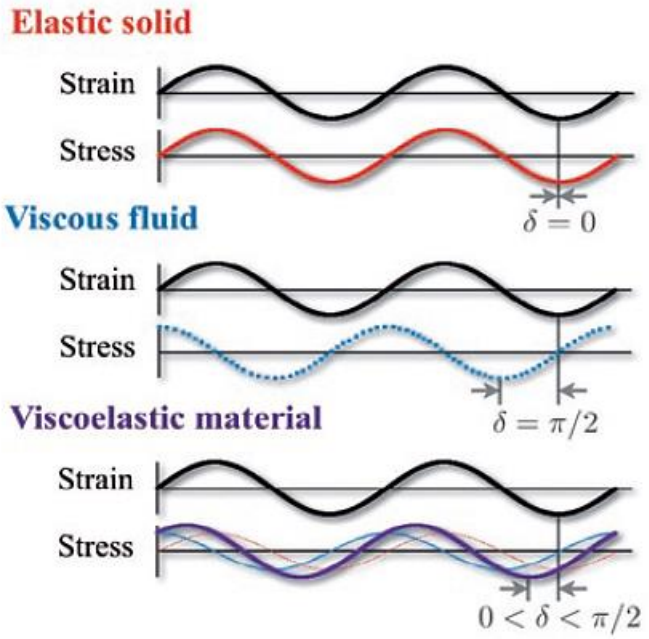

Figure 2.23: Schematic stress response to a controlled oscillatory strain deformation for an elastic solid (top), a viscous fluid (middle), and a viscoelastic material (bottom) (Adapted from Weitz and Wyss et al., 2007)

Using the Maxwell model, the measured stress response $\sigma(t)$ of a viscoelastic material for an applied dynamic sinusoidal controlled strain deformation of $\gamma(t) = \gamma_0 \sin(\omega t)$ is expressed as (Weitz and Wyss et al., 2007):

$$\sigma(t) = G'(\omega)\,\gamma_0 \sin(\omega t) + G''(\omega)\,\gamma_0 \cos(\omega t) \qquad (2.7)$$

where $G'(\omega)$ = storage modulus as a function of ω (Pa)

$G''(\omega)$ = loss modulus as a function of ω (Pa)

The storage modulus G' and the loss modulus G'' characterize respectively the solid-like and the fluid-like contributions to the measured outcome of the stress response. G' can be understood as a measure of the amount of energy stored under deformation and G'' is a measure of the energy lost in the form of dissipated heat. Using the complex notations applied in the analysis of harmonic systems, these two moduli can be combined to represent the notional spring and dashpot constituents of the Maxwellian model in the more compact complex modulus G^* equation (Barnes and Hutton, 1989):

$$G^*(\omega) = G'(\omega) + iG''(\omega) \tag{2.8}$$

The values of these complementary parameters vary with angular frequency ω, and in an oscillatory rheological experiment $G'(\omega)$ and $G''(\omega)$ are measured because a material can be solid-like or liquid-like depending on the time scale at which it is deformed. The moduli can further be expressed as sine and cosine functions of δ yielding the following two equations:

$$G'(\omega) = \frac{\sigma_0}{\gamma_0} \cos(\delta) \tag{2.9}$$

$$G''(\omega) = \frac{\sigma_0}{\gamma_0} \sin(\delta) \tag{2.10}$$

Dividing equation 2.10 with equation 2.9 will yield the loss tangent (or damping factor) representing the ratio of the loss to storage modulus:

$$\tan(\delta) = \frac{G''(\omega)}{G'(\omega)} \tag{2.11}$$

In typical oscillatory rheology studies an amplitude-sweep test is first conducted on the unknown sample to identify if any, the linear viscoelastic region where the internal structure remains stable. This is characterized by a region in the shear modulus versus amplitude curve where *G'* and *G''* become independent of amplitude. Beyond a limiting strain γ_c the viscoelastic behaviour becomes non-linear and usually both *G'* and *G''* begin to slope downwards. The analogue to the complex shear modulus $G^*(\omega)$ in oscillatory measurements is the complex viscosity $\eta^*(\omega)$, expresssed as:

$$\eta^*(\omega) = \frac{\sigma(t)}{\dot{\gamma}(t)} = \eta'(\omega) + i\eta''(\omega) \tag{2.12}$$

where the dynamic viscosity real and imaginary terms respectively are:

$$\eta'(\omega) = \frac{G''(\omega)}{\omega} \tag{2.13}$$

$$\eta''(\omega) = \frac{G'(\omega)}{\omega} \tag{2.14}$$

For non-thixotropic shear thinning fluids, viscosity varies only with shear rate or temperature. Thixotropic materials such as concentrated dispersions on the other hand are more complex because their viscosities do not immediately reach a steady state upon the removal of applied shear stress. Steady state is dependent on the internal microstructural network which when broken down under strain requires time to subsequently reform or rebuild. For a presheared sample, this long-term time dependent recovery behaviour can be

seen with a low speed oscillatory analysis as shown in Figure 2.24 where over time the storage modulus *G'* catches up with the loss modulus *G"* and continues to increase even long after *G"* has reached a steady state plateau. This points to a gradual rebuilding of the internal network structure over time. Note that the complex viscosity η^* continues to recover at the same rate as *G'* due to the contribution of the imaginary viscosity term η".

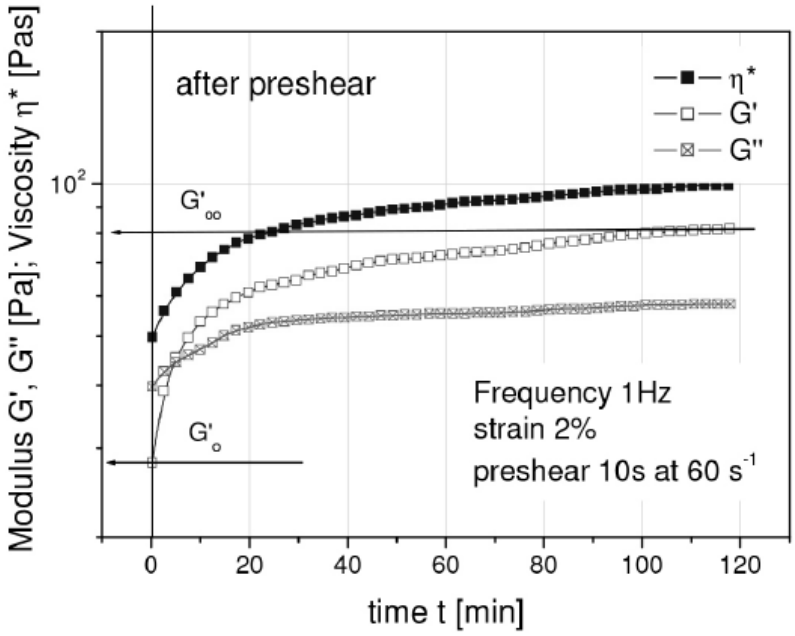

Figure 2.24: Low frequency time depenent oscillatory analysis for a presheared thixotropic concentrated dispersion (Adapted from Franck, 2004)

According to Barnes (2000) the moduli of structured fluids generally undergo changes over a few distinct regions from very low (around 10^{-3} rad/s) to very high (around 10^{8} rad/s) oscillation rates giving a distinct viscoelastic fingerprint as shown in Figure 2.25.

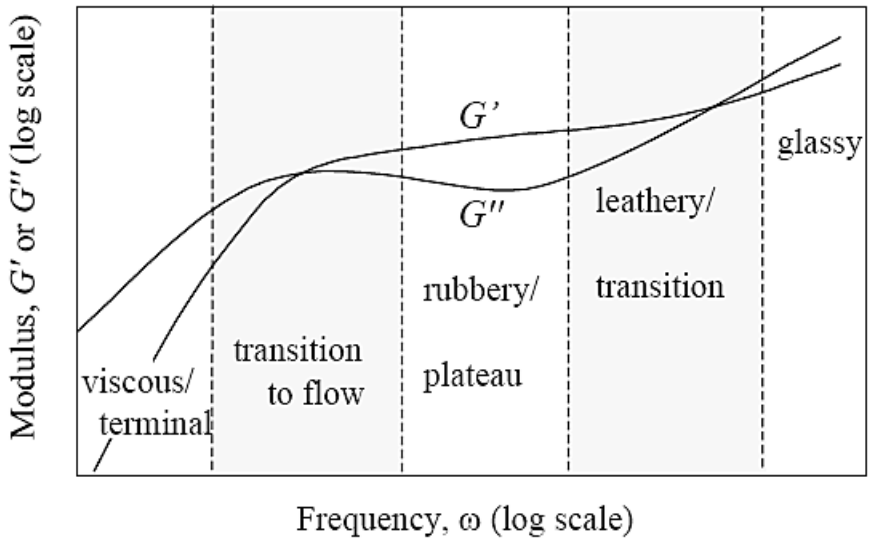

Figure 2.25: Various regions of general viscoelastic behaviour from very low to very high oscillatory speeds (Adapted from Barnes, 2000)

In the viscous/terminal region, stresses can relax through the long-range reorganization of the internal microstructure due to the long time duration of low frequency oscillations thus allowing the viscous behavior of the material to dominate. In the following region, the domination of *G"* begins to diminish as the material begins the transition to flow (but does not actually flow) and the first crossover point is encountered. Going into the rubbery/plateau region, elastic behaviour dominates and the value of *G"* is always lower than that of *G'*. What follows after this is the leathery/higher transition region where the value of *G"* rises again and the second crossover point emerges due to high-frequency dissipation mechanics and network relaxation effects. Lastly at the highest frequencies a glassy region appears where *G"* again predominates and continues to rise faster than *G'*.

It is hoped that this section of the literature review managed to uncover the pertinent aspects of the complex field of rheology and rheometry thus providing a theoretical foundation for analyzing the results obtained from experimental measurements performed on the graphene filled DGEBA samples.

2.5 Percolation Threshold (Pc) of ICAs

The intrinsic conductivity and the loading concentration of filler material are two major variables which affect the bulk resistivity of an ICA. At very low filler loadings, the matrix behaves like a insulator because the insulating property of the polymer binder dominates. As the concentration of conductive filler material increases to a critical level, the resistivity of the matrix drops precipitously.

Percolation threshold (Pc) is defined as the filler concentration at which point the electrical conductivity of an insulating polymer matrix increases dramatically or more precisely as the mid-point of a suddden increase in conductivity or conversely a suddden drop in resistivity. Figure 2.26 is a schematic illustration of the percolation mechanism for a metal filled matrix.

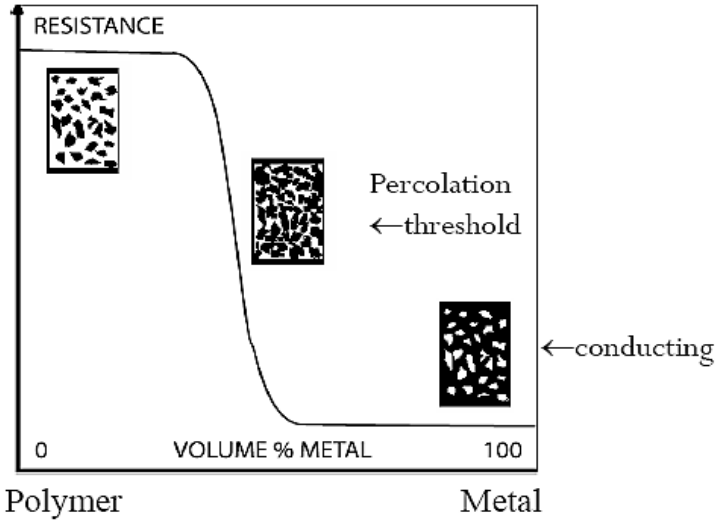

Figure 2.26: Schematic resistivity curve of metal filled polymer (Adapted from Suhir and Lee et al., 2007)

Stankovich and Dikin et al. (2006) found that the chemical reduction of phenyl isocyanate treated GO mixed in with dimethylformamide (DMF) dissolved polystyrene yielded a homogenously dispersed network of graphene (RGO) sheets in the hardened polystyrene matrix, see Figure 2.27.

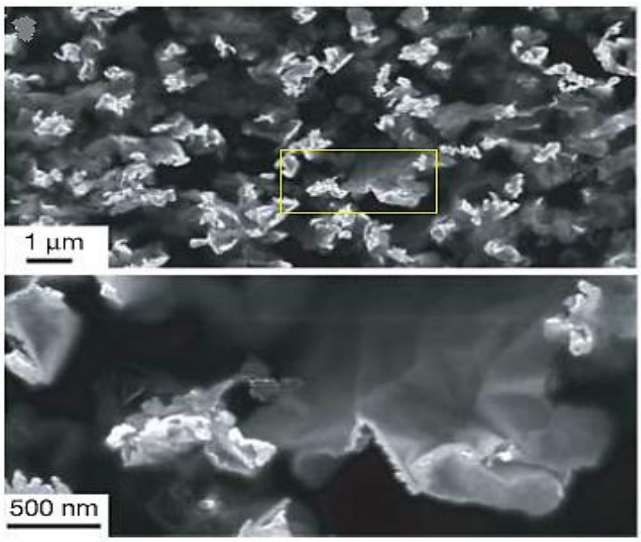

Figure 2.27: FESEM images from a fractured surface of 0.48% volume fraction graphene-polystyrene composite (Adapted from Stankovich and Dikin et al., 2006)

They suggested that the low barrier-energy graphene sheets would have crumpled and agglomerated into larger particles had they not been coated and thus stabilized with a film of polymer during the reduction stage with N,N-dimethylhydrazine as the reducing agent. Thus this in-solvent processing strategy proved to be the key factor in achieving a very low percolation threshold of 0.1% volume, see Figure 2.28 which was three times lower than any reported two-dimensional fillers used by other researchers up to the time of their experiments.

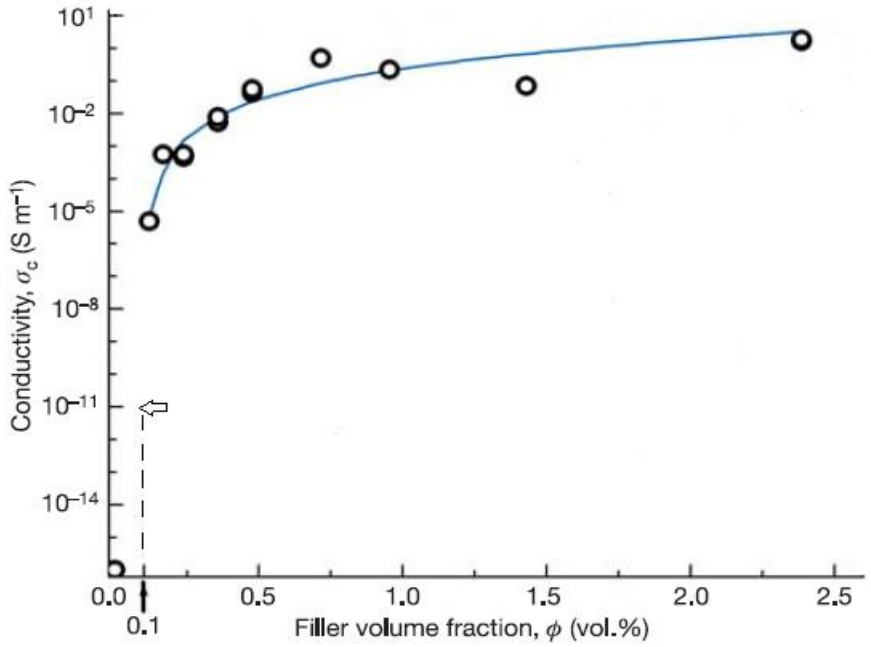

Figure 2.28: Electrical conductivity of polystyrene–graphene composite as a function of filler % volume fraction, Pc = 0.1% volume fraction (Adapted from Stankovich and Dikin et al., 2006)

At 2.4% filler volume the matrix reached a plateau bulk conductivity value of 1 x 10^{0} S m^{-1} which converts to a bulk resistivity of 1 x 10^{2} Ω cm. Stankovich and Dikin et al. (2007) subsequently published a paper on the

synthesis of graphene (RGO) particles via the chemical reduction of exfoliated GO and reported the highest bulk conductivity of compressed RGO particles (as per the same volume fractions applied in the composite samples) at ~ 2 x 10^2 S m^{-1} which converts to 5 x 10^{-1} Ω cm in terms of bulk resistivity, refer to Figure 2.29. By extrapolating these results, they estimated the intrinsic bulk resistivity of RGO at 4 x 10^{-2} Ω cm. This can be taken as the limiting value at which the bulk resitivity of an RGO-filled matrix cannot go below.

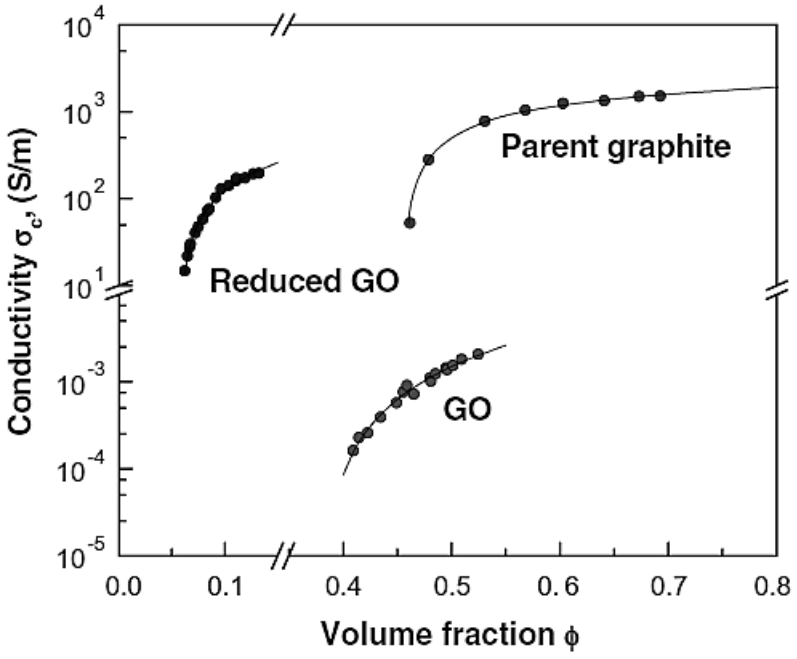

Figure 2.29: Conductivity as a function of the volume fraction of three different compressed graphitic powders: pristine graphite, GO, and reduced GO (Adapted from Stankovich and Dikin et al., 2007)

A number of years after Stankovich and Dikin published their findings, the percolation thresholds achieved with other processing strategies such as in situ polymerisation and melt processing were compiled by Verdejo and Bernal

et al. (2011) showing that solvent processing strategy still yielded the lowest percolation thresholds, see Figure 2.30.

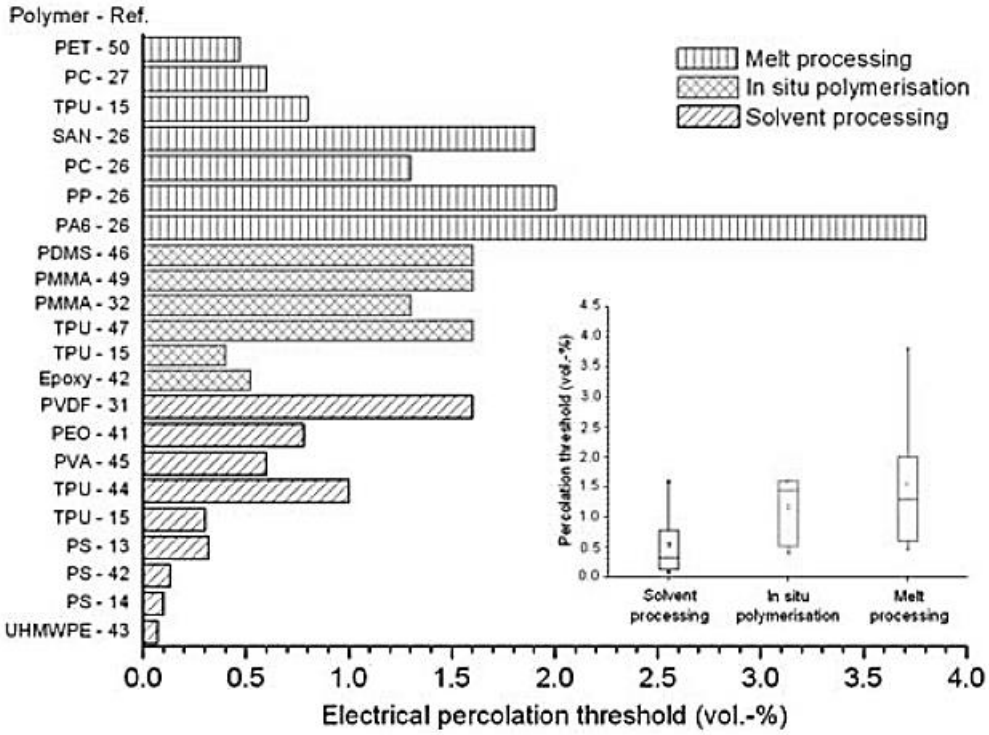

Figure 2.30: Electrical percolation thresholds of graphene/polymer nanocomposites according to processing strategy (Adapted from Verdejo and Bernal et al., 2011)

Since silver-filled die-attach adhesives have been used for decades in the semiconductor asssembly industry it makes sense to benchmark the performance of experimental graphene-filled composites against such a well established ICA. Wu and Wu et al. (2007b) reported that widely used silver-filled ICAs had percolation thresholds at 25% to 30% filler volume. This is much higher compared to the percolation threshold range of 0.1% to 4.0% volume for the graphene filled polymer systems reviewed by Verdejo and Bernal et al. Minimal filler content is of course desirable for economic

reasons. Lower filler content is also beneficial for maintaining the bonding and mechanical strength of polymer adhesives (Mukhopadhyay and Gupta , 2012).

Wu and Wu et al. (2007a) studied the effect of Ag particle size on the bulk resistivity of silver-epoxy composites and reported a percolation threshold range of 55% to 75% weight as the size of particles increased, refer to Figure 2.31. Note that the magnitude of an equivalent mass of filler loading is always higher when expressed as a weight percentage instead of a volume percentage because silver is denser than epoxy.

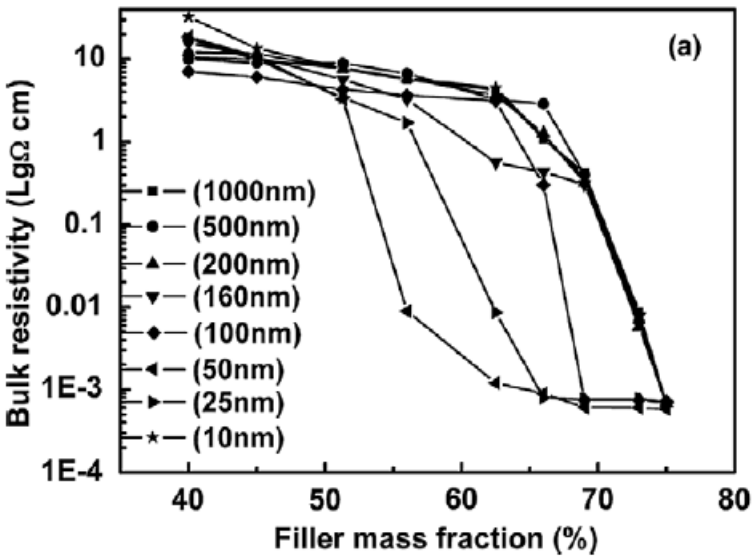

Figure 2.31: Bulk resistivity versus filler mass (weight %) at various average Ag particle sizes (Adapted from Wu and Wu et al., 2007a)

The lowest bulk resistivity value of each curve fell between 1 x 10^{-4} and 1 x 10^{-3} Ω cm. This range is similar to commercially available Ag-filled ICAs as reported at their websites by manufacturers such as Dow Corning and Epotek (Dow Corning Corp., 2015; Epoxy Technology Inc., 2015). In

comparison the bulk resistivity of Sn/Pb solder is 1.5 x 10^{-5} Ω cm (Wong and Moon et al., 2010) whilst the bulk resistivity of pure silver is 1.60 x 10^{-6} Ω cm (Matula, 1979).

From the literature reviewed thus far, it can be concluded that the bulk conductivity of chemically reduced graphene (RGO) filled ICA is inferior compared to that of silver-filled composites. Even when RGO particles did not agglomerate and were homogenously dispersed throughout the polymeric binder material, bulk resitivity measurements obtained by Stankovich and Dikin et al. (2006) at around 1 x 10^{2} Ω cm were still at least three orders higher compared to their estimated value for the intrinsic bulk resistivity of RGO at 4 x 10^{-2} Ω cm. He and Tjong (2013) used a similar solvo-thermal direct GO reduction method and produced polymer composites at an unimpressive minimum bulk resistivity of 8 x 10^{5} Ω cm (at filler concentration of 1.4% by volume fraction) even though the percolation threshold occurred at a very low 0.31% volume fraction.

CHAPTER 3

MATERIALS AND METHODOLOGY

3.1 Materials

The following is a list of materials and chemicals used and their respective sources:

Bisphenol A diglycidyl ether (D 3415); Sigma-Aldrich

Distilled water; Prepared in UTAR materials laboratory

Ethanol 97%; Systerm

Ethylenediamine ($C_2H_4(NH_2)_2$) 99%; ChemSoln

Graphene Oxide; Prepared in UTAR materials laboratory

Hydrazine hydrate (N_2H_4) 80%; R&M Chemicals

Hydrochloric acid (HCL) 37%; Systerm

Hydrogen peroxide (H_2O_2)30%; R&M Chemicals

Natural graphite flakes (Nano 25 grade); Asbury Carbons

Phosphoric acid (H_3PO_4) 85%; Systerm

Potassium permanganate ($KMnO_4$) 99.9%; ChemSoln

Sulphuric acid (H_2SO_4) 98%; Systerm

3.2 Preparation of GO

GO is the precursor material required for the synthesis of graphene and was produced via the chemical oxidation of graphite flakes according to the technique developed by Huang and Lim et al. (2011) because the steps involved are simple, safe, and yielded a 100% conversion of graphite flakes. The following table lists the specific materials used.

Table 3.1: Quantity of materials used for GO synthesis

Material	Brand	Quantity
Sulphuric acid 98%	Systerm	90 ml
Phosphoric acid 85%	Systerm	10ml
Graphite flakes Nano 25	Asbury Carbons	1g
Potassium permanganate 99.9%	ChemSoln	4g
Hydrogen peroxide 30%	R&M Chemicals	As needed
1M Hydrochloric acid	Systerm	As needed
Distilled water	Prepared in lab	As needed

Firstly, H_2SO_4 and H_3PO_4 are poured into a beaker at a ratio of 90:10 ml followed by the addition of 1 g of graphite flakes. A magnetic stir bar is added and the stir plate switched on and set at a moderate stirring speed to prevent the contents from splashing out. Next, 4 g of $KMnO_4$ oxidizing agent is slowly added so that the temperature of the exothermic reaction is kept below 50 ºC. The beaker is then covered with a petri dish and the mixture left to stir for 72 hours for the graphite flakes to completely oxidize. The colour of

the mixture will change from the initial blackish purple-green tint to a dark brown colour by the end of the third day of stirring as shown in Figure 3.1.

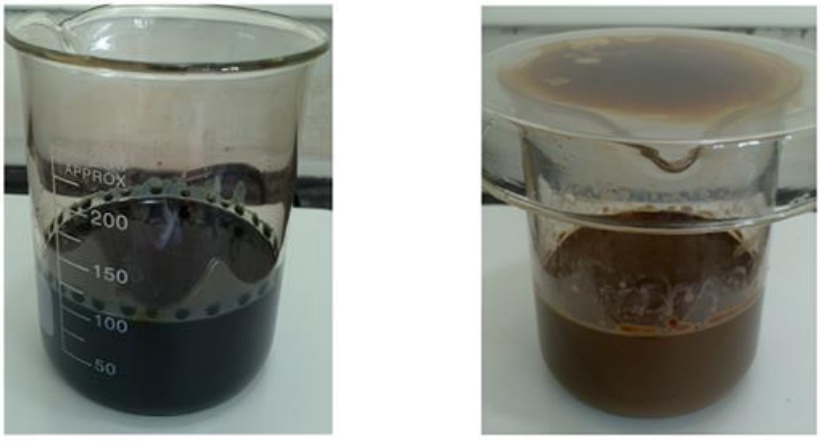

(a) **(b)**

Figure 3.1: Graphite oxidation process a) blackish purple-green tint mixture at time zero, b) turns dark brown after 72 hours of stirring

To neutralize the residual $KMnO_4$ in the mixture and terminate the oxidizing reaction, H_2O_2 solution is slowly added with a dropper until the outgassing of oxygen stops. The colour of the mixture will turn milky yellow-brown as shown in Figure 3.2 a) indicating the presence of intercalated GrO.

(a) **(b)**

Figure 3.2: Mixture a) turns milky yellow-brown colour after addition of H_2O_2, b) turns into a dark brown coloured GO gel after HCL wash

The GrO formed is then washed with an aqueous solution of HCl at a concentration of 1 M to dissolve the potassium and phosphoric salts produced during the addition of $KMnO_4$ and then rinsed with distilled water to remove the salts and residual H_2SO_4 and H_3PO_4. The last step of the washing procedure requires the decantation of the supernatant after centrifugation at 10,000 g to recover the concentrated product. The whole cycle is then repeated 3 times until a pH of 4–5 is reached. Because the GrO particles are intercalated with oxygenated functional groups, they will naturally exfoliate and separate somewhat but not completely into multi-layered GrO sheets turning dark brown in colour and eventually thickening into a GO gel by the end of the washing process as shown in Figure 3.2 b).

Finally the GO gel is poured into a petri dish and placed in a drying oven at 45 ºC for 24 hours. Figure 3.3 shows the dried GO flakes after being scraped out from the petri dish. The dried flakes should be kept in a desiccator or sealed in a dry environment. Batch to batch yield ranges from 2 g to 6 g depending on the amount of wastage incurred during the washing process.

Figure 3.3: Dried GO flakes

The Varian Cary 100 UV-Vis spectrometer was then used to examine the synthesized GO. Samples for UV-Vis examination were prepared from similar amounts of dried GO flakes dissolved in distilled water and ultrasonicated until a semi-transparent yellowish light brown colloid is obtained. Dispersion concentrations were not tightly controlled because slight differences only influence peak intensities while the relative peak positions of absorption bands remained unaffected.

Other analytical techniques used to analyse GO were XRD spectroscopy, FTIR spectroscopy, Raman spectroscopy, and XPS spectroscopy. They are further elaborated in section 3.3 because these techniques were also applied to analyse RGO.

3.3 Graphene Synthesis

Graphene, or more precisely chemically reduced graphene (RGO) was synthesized according to the Stankovich (Stankovich and Dikin et al., 2007) top-down process via the chemical reduction of exfoliated GrO. Unlike other methods such as CVD and mechanical micro-exfoliation discussed in chapter 2, this approach to the challenge of producing graphene is high yielding and easy to scale up. Table 3.2 shows the list of materials used in the RGO synthesis process.

Table 3.2: Quantity of materials used for RGO synthesis

Material	Brand	Quantity
Dried GrO	As synthesized	100mg
Distilled water	Prepared in lab	100ml
Hydrazine hydrate	R&M Chemicals	1ml
Ethanol 97%	Systerm	As needed

The process starts off with 100 mg of dried GrO added into a beaker filled with 100 ml of distilled water and then ultrasonicated for about 30 minutes until a light brown coloured clear colloid is attained. This step is performed to ensure that intercalated GO particles in the dried GrO flakes are exfoliated and separated into stable GO sheets. The dispersed content is then transferred into a 250 ml round-bottom flask.

Next, 1 ml of hydrazine hydrate is added and the flask attached to a water-cooled condenser. The assembly is kept upright with a retort stand and connected to a running water supply. Lastly, the round-bottomed flask is submerged in glycerol heated at 100 ºC and left to react for 24 hours. The dispersed GO and apparatus setup is shown in Figure 3.4.

(a) **(b)**

Figure 3.4: a) Dispersed GO, b) RGO synthesis apparatus setup

As the reaction progresses the brown coloured dispersed GO will gradually agglomerate into fine black particles, continue to precipitate and eventually coagulate into a floating cake after 24 hours as shown in Figure 3.5.

Figure 3.5: Floating coagulated RGO after 24 hours hydrazine reduction

The coagulated RGO cake is then broken into smaller clumps and poured out into a beaker after which the clumps will settle down to the bottom after cooling to room temperature as shown in Figure 3.6.

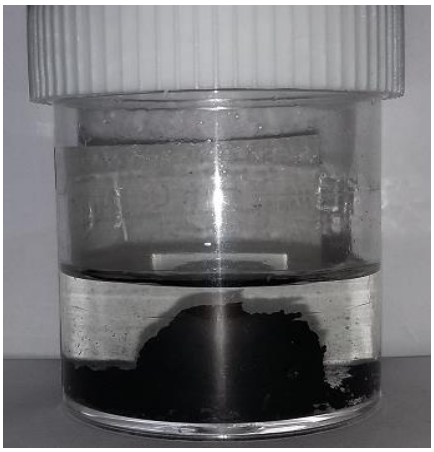

Figure 3.6: Coagulated RGO settling to the bottom after cooling

The broken RGO clumps are drained out by filter paper then washed with 100 ml of distilled water followed by 100 ml of ethanol for 5 cycles. Some of the washed products are kept in ethanol as wet solids and some are oven dried at 45 ºC for 24 hours and yielded coarse hard particles some larger than 1 mm as shown in Figure 3.7. This is a poor outcome in the sense that the surface area to volume ratio of dried RGO is extremely low.

Figure 3.7: Oven dried RGO particles

When the oven dried RGO particles are mixed into DGEBA and hand stirred vigorously for 30 minutes, they break into smaller sizes but still remained coarse as shown in Figure 3.8.

Figure 3.8: 3% weight oven dried RGO /DGEBA mixture hand stirred for 30 minutes

In order to overcome this problem, wet and spongy RGO clumps were press-dried in filter paper to a thickness of 1 mm resulting in a still soft and slightly moist product. The RGO clumps disintegrated easily into much smaller particles and were homogenously dispersed after 30 minutes of hand stirring as shown in Figure 3.9.

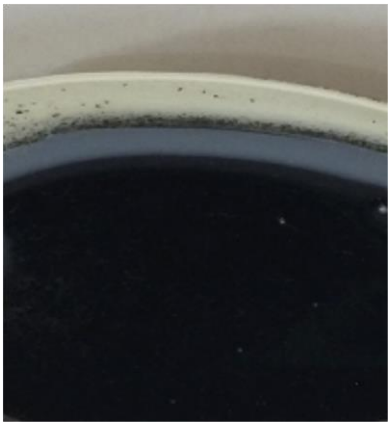

Figure 3.9: 3% weight press-dried RGO/DGEBA mixture hand stirred for 30 minutes

The mass of RGO had to be accurately determined due to the presence of residual ethanol in the press-dried material. Oven drying correlation experiments were conducted and the weight of press-dried RGO was found to be eight times (8x) heavier than oven dried RGO. Thus the quantity of press-dried RGO must be increased by 8x during weighing to obtain the same mass of dried RGO and thereafter immediately stirred into the DGEBA epoxy while the filler is still slightly moist and soft.

Even though the residual ethanol should evaporate during the hand stirring process, each sample must still be allowed to sit at least 30 minutes prior to further experimental procedures for any remaining ethanol to fully evaporate. Samples were then prepared and examined using various analytical techniques as described in the following paragraphs.

Dried samples were examined using the Thermo Scientific Nicolet iS 10 attenuated total reflectance (ATR) FTIR spectrometer to obtain FTIR spectroscopy data over a wave number range of 4000 – 400 cm^{-1} at a resolution of 4 cm^{-1}. This range corresponds to a wavelength of 2500 nm to 25 µm which is sufficient to study the infrared active oxygen functionalized groups, i.e. the carboxylic acid (COOH), epoxide (C-O-C), hydroxyl (OH), and carbonyl(C=O) groups which are supposed to be present in GO as discussed in chapter 2.

An X-ray diffractometer was employed to examine the starter graphite, GrO and RGO samples. XRD spectroscopy is a technique used to characterize the crystalline structure of material through the detection and analysis of the constructive and destructive interference patterns from diffracted incident x-ray beams. According to Bragg's Law the path of diffracted x-ray waves must obey the following relationship called the Bragg equation (Cullity, 1956):

$$\lambda = 2d \sin \theta \tag{3.1}$$

where d = crystal interplanar lattice distance (nm)

θ = wave incident angle (degree)

λ = wavelength (nm)

The signal from sample diffraction patterns are collected at an angle of 2θ as illustrated in figure 3.10. The Shimadzu XRD-6000 diffractometer used to acquire all the experimental diffraction spectra has a monochromatic Cu Kα radiation source with a wavelength of λ = 1.54 Å (or 0.154 nm). Graphite (powder), RGO (powder) and GrO (flakes) were loaded on aluminium sample holders and examined at a 2θ range of 5 degrees up to 70 degrees.

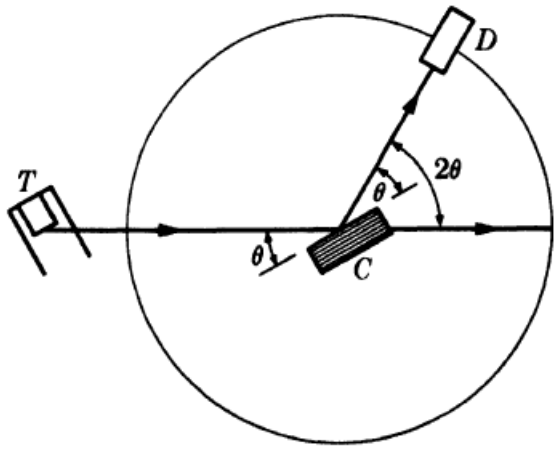

Figure 3.10: Schematic of an x-ray beam from a monochromatic source (T) striking the parallel planes of the crystal sample (C) at an incident angle θ, then scattering to the detector (D) at a diffraction angle 2θ (Cullity, 1956)

Raman spectroscopy is an especially useful technique for providing information on the chemical structures and physical forms of graphene in terms of lattice disorder, sheet layers, grain boundary, and edge conditions amongst other characteristics. It can provide a frame of structural reference as a common denominator for comparing different materials; for example to distinguish a hard amorphous carbon from a metallic nanotube, graphite from graphene, or even identify a doped graphene sample by using the Raman shift spectrum as a fingerprinting technique (Ferrari, 2007).

When light interacts and polarizes the electron cloud surrounding atomic or molecular nuclei, discrete units of vibrational mechanical energy called phonons (quasiparticles) are produced. Since this perturbation is an unstable time-dependent 'virtual state', photons are quickly re-radiated (scattered) by the short-lived phonons following which the interacting material

will stabilize to its original energy state. In elastic (or Rayleigh) scattering, re-radiated photons are scattered in different directions but retain the same wavelength as incident photons. However, in the non-resonant inelastic (or Raman) scattering condition, about one in every 10^6 to 10^8 re-radiated photon will have its energy state altered. And if the energy level of the incident photon happens to be high enough to coincide with the electronic transition state of the interacting material (resonant condition), it will cause a resonant effect and this will increase the probability of Raman scattering by several orders of magnitude. Raman spectroscopy is thus particularly well suited for analysing graphene since it is a zero band gap material and will always interact with photons under resonant conditions (Smith and Dent, 2013; Ferrari and Basko, 2013).

In Raman scattering, a red shift (Stokes scattering) occurs when a re-radiated photon loses energy while a blue shift (anti-Stokes scattering) occurs when it gains energy. Figure 3.11 illustrates the Stokes and anti-Stokes scattering events and their energy states in the resonant condition where electron-hole pairs are created. The Renishaw in Via confocal Raman microscope was used to acquire red shifted (Raman shift) signals in Stokes scattering by filtering out the signals from Rayleigh scatterings. Since anti-Stokes scattering signals are weak and rare, they are usually ignored. Spectral bands showing Raman high intensities in many cases have weak infrared intensities whilst the reverse is also true. Raman spectroscopy and FTIR absorption spectroscopy are usually performed together to form a pair of powerful complementary characterization techniques (Smith and Dent, 2013).

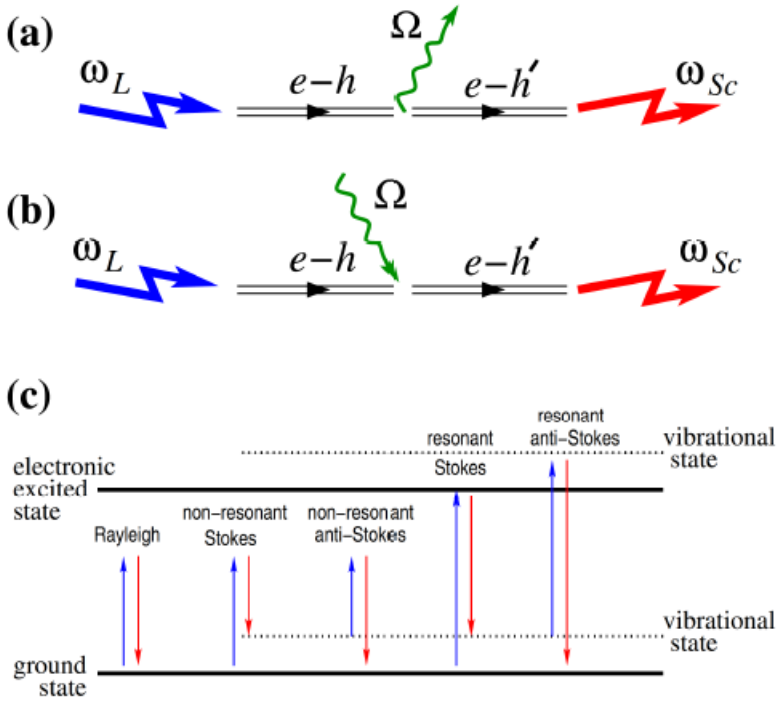

Figure 3.11: (a) Resonant Stokes scattering: an incoming photon ω_L excites an electron-hole pair *e-h*. The pair decays into a phonon Ω and another electron-hole pair *e-h′*. The latter recombines, emitting a photon ω_{Sc} (b) resonant anti-Stokes scattering: the phonon Ω is absorbed by the electron-hole pair (c) Energy states of scattering events [Adapted from Ferrari and Basko, 2013]

XPS also known as Electron Spectroscopy for Chemical Analysis (ESCA) is a surface-sensitive chemical analysis spectroscopic technique used for element identification, elemental composition quantification (parts per thousand range) and the analysis of the chemical state of atoms at the sample surface down to 10 nm below the surface. In a typical XPS analysis, a monochromatic soft x-ray beam (typically Al Kα radiation, hv = 1486.6 eV) is projected unto a sample placed in a high vacuum chamber. When core electrons are ejected in a photoemission event, they escape into the vacuum

environment as photoelectrons and are detected and counted by an electron detector while their kinetic energy levels are measured and processed by an energy analyser to determine their binding energies (Chastain and King, 1992). A schematic of the photoemission effect is shown in Figure 3.12.

The ULVAC-PI Quantera II Scanning XPS Microprobe was used to acquire the kinetic energies of the emitted photoelectrons and to compute their corresponding binding energies which are then used as markers to identify the elements and chemical bonds that are present while the elemental composition can be established based on the underlying assumption that the number of electrons detected is proportional to the number of atoms present.

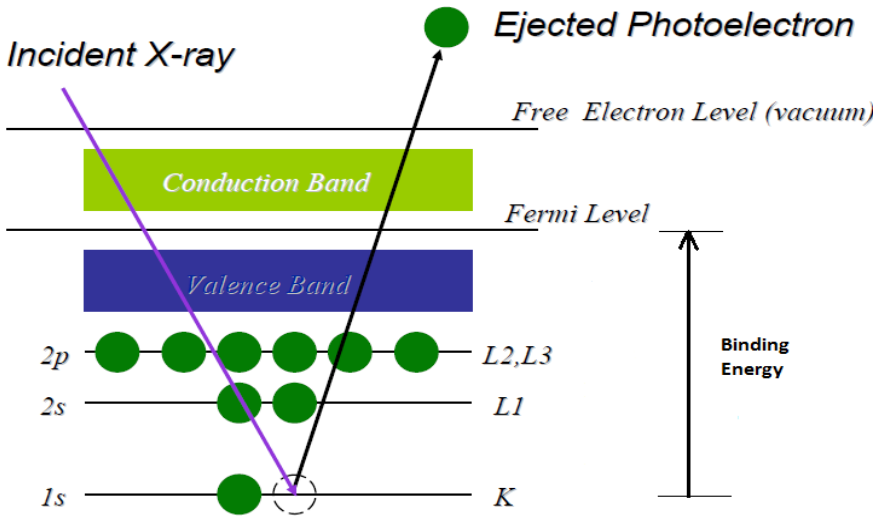

Figure 3.12: Schematic of the photoemission effect. (Adapted from PIRE-ECCHI, 2015)

Finally samples of the starter graphite, GO and RGO were examined with the Hitachi S-34000N scanning electron microscope (SEM) equipped with EDX spectrometer, JEOL JSM-6701F field effect scanning electron

microscope (FESEM), and FEI Technai G2 F20 X-Twin high resolution transmission electron microscope (HRTEM with SAED) for electron imaging and analysis.

3.4 Rheology Experiments

The Anton Parr Physica MCR 301 rheometer shown in Figure 3.13 was used to perform the rheological experiments. All measurements were conducted with the 25 mm diameter parallel plate spindle operating at a gap distance of 0.5 mm. The Peltier plate (bottom non-rotating sample platform) temperature was set at 25 ºC.

Figure 3.13: Anton Parr MCR301 rheometer (inset: side view of inserted 25 mm parallel plate spindle at a fully raised position)

Firstly, DGEBA epoxy resin should be preheated to 50 ºC for at least 30 minutes to ensure that crystallized particles if present are fully melted and stabilized. This is an important preparatory step to prevent spurious results caused by recrystallization while rheological measurements are being taken. RGO filler is then mixed in and hand stirred with a metal spatula at various concentrations by weight % and subjected to rheological measurements. The sample mixes and concentrations are shown in Table 3.3.

Table 3.3: Sample formulation and description

Sample name	Filler wt. %	Filler description
E.P. 0.01%	0.01	Press-dried RGO*
E.P. 0.5%	0.5	Press-dried RGO*
E.P. 1%	1	Press-dried RGO
E.P. 2%	2	Press-dried RGO
E.P. 3%	3	Press-dried RGO
E.P. 4%	4	Press-dried RGO
O.D. 3%	3	Press-dried RGO
Epoxy neat	0	Control sample - pure DGEBA
Graphite 3%	3	Graphite for benchmarking

* Resistivity measurements only

Each sample is then subjected to a constant speed (50 s^{-1}) flow test to obtain baseline viscosity measurements, a hysteresis loop test for thixotropy, yield test for establishing yield stress (if present), and oscillatory amplitude sweep to define the LVER region followed by a frequency sweep to study the stability of the dispersion.

3.5 Percolation Threshold Measurements

Following the rheological measurements, the samples are hand stirred vigorously with the curing agent EDA ($C_2H_4(NH_2)_2$), left to harden (pre-cure) overnight at room temperature and then oven cured at 100 ºC for one hour.

There are four active hydrogen atoms available in the two amine (NH_2) groups for each EDA molecule to provide the bonding reactions with the epoxide groups of DGEBA molecules. Given that the molar weight (MW) of EDA is 60.1 g mol^{-1} and the epoxide equivalent weight (EEW) of the Sigma-Aldrich DGEBA is 174 g (Sigma-Aldrich, 2015), the stoichiometric ratio in terms of parts by weight per hundred parts (phr) epoxy resin used for EDA loading is determined at 8.64 phr by the calculations shown below (DOW Epoxy, 2015):

$$\text{phr} = \text{amine H eq wt.} \times 100 / \text{EEW of epoxy} \qquad (3.2)$$

$$= 15.02 / 174$$

$$= 8.64$$

where

$$\text{amine H eq wt.} \times 100 = \frac{\text{MW of Amine}}{\text{No.of active hydrogen}}$$

$$= 60.01/ 4$$

$$= 15.02$$

It was found that the EDA phr loading of 8.64 phr is sufficient in fully curing neat epoxy following the curing schedule stated in the first paragraph of

this section. But for samples loaded with RGO fillers, the composite remained soft immediately after oven curing and requires up to several days to fully harden at room temperature thereafter. The effect of RGO on reducing the curing efficacy of EDA is not fully understood but this problem is easily overcome by marginally increasing the amount of EDA added (10% increase for every 1 g of RGO added) above the stoichiometric ratio. The mold used to shape and contain the composite samples for curing is a simply four pieces of pencil erasers carefully squared and glued onto the unplated side of a printed circuit board as shown in Figure 3.14. Carnauba wax is applied on the exposed PCB surface as a mold release agent to ensure the easy removal of the cured samples.

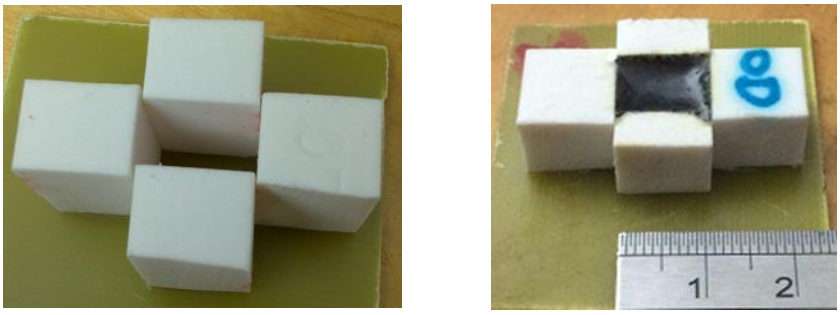

(a) **(b)**

Figure 3.14: Mold a) Unfilled b) Filled

Once the cured samples are removed they are shaped and hand polished with sandpaper until the surfaces become flat and the edges squared as measured with a Vernier caliper. Lastly, any two opposite ends are coated (smeared) with graphite powder and the samples are now ready for bulk resistivity measurements as shown in Figure 3.15.

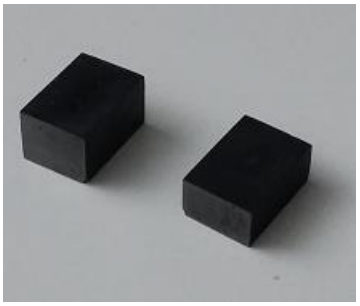

Figure 3.15: Finished samples. Graphite coated surface is light grey

The finished samples are securely clamped in a table top vice with the graphite coated surfaces making firm and even contact with the copper plated surfaces of two PCB electrodes as shown in Figure 3.16. This is to ensure that contact surface resistance is reduced to an insignificant level.

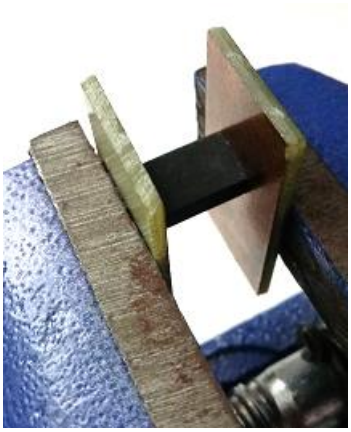

Figure 3.16: Setup for resistance measurements

Resistance measurements are made with the Keithley 4200-SCS parameter analyser which is able to supply forced currents as low as 0.1×10^{-15} amperes allowing it to measure values up to the 10^{12} Ω range. The

instrument also has an inbuilt four-point probe feature capable of easily measuring very low resistances in the μΩ range. Once the resistance and physical dimensions of each sample are determined, bulk resistivity (ρ) values can be computed using equation 2.1 shown in Chapter 2. The various experimental sample formulations are listed in Table 3.3.

CHAPTER 4

RESULTS AND DISCUSSION

4.1 GO and RGO Characterization

Since the characterization of GO and RGO requires broadly similar analytical techniques, the discussion of their test results are therefore organized together under this section.

4.1.1 Ultraviolet-Visible (UV-Vis) Spectroscopy

The GO oxidized with 4 g of $KMnO_4$ displayed a plasmonic UV absorption peak at a wavelength of 231 nm coupled with a broad sloping shoulder around 300 nm due to the $n \rightarrow \pi^*$ electronic transition in carbonyl groups. This spectral shape is consistent with that reported by Huang and Lim et al. (2011). As expected the peak wavelength at 231 nm is slightly longer than Huang's 4.5 g $KMnO_4$ (more oxidized) sample with a peak at 229 nm because the absorption peaks found at around 230 nm occurred due to the $\pi \rightarrow \pi^*$ electronic orbital transitions from conjugated aromatic C=C bonds; where the higher the degree of oxidation the fewer remaining conjugated C=C bonds there are, thus requiring shorter wavelength (more energetic) UV photons to elicit $\pi \rightarrow \pi^*$ electronic transitions.

This explanation was verified when a batch of less oxidized GO prepared using 3 g of $KMnO_4$ showed a plasmon peak at an even longer wavelength position of 236 nm. For benchmarking purposes, a sample of Sigma-Aldrich commercial GO was tested and it displayed a spectral pattern similar to that of the synthesized GO with a peak positioned at 227 nm, refer to Figure 4.1.

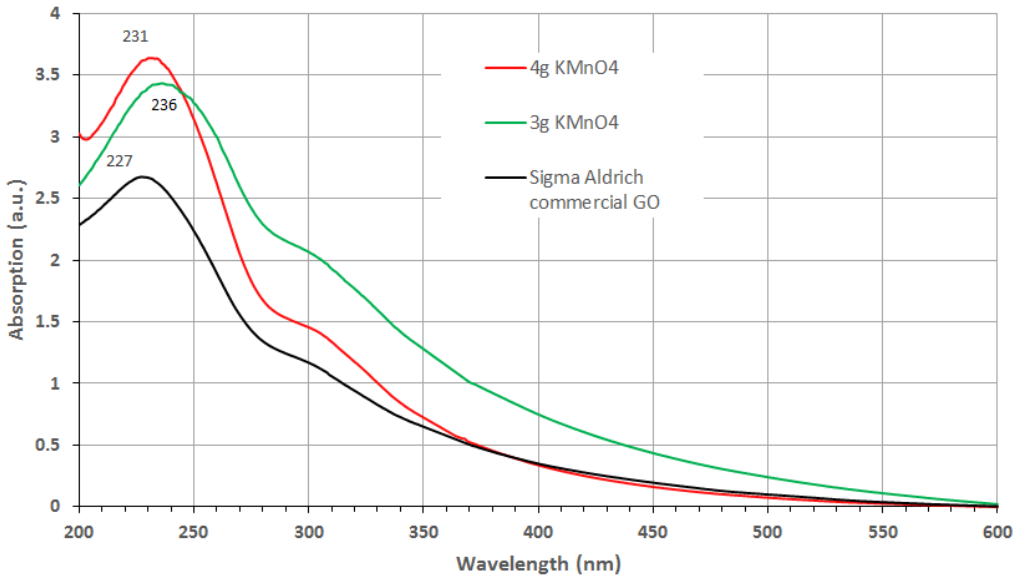

Figure 4.1: UV-Vis absorption spectra

This UV-Vis results taken together with the observation that no residual graphite flakes were found at the end of the graphite oxidation process, it is safe to conclude that the GO synthesis process per Huang's method achieved its intended purpose of converting graphite flakes to GO.

4.1.2 Fourier Transform Infrared (FTIR) Spectroscopy

Table 4.1 lists the principal infrared absorption bands present in GO and their corresponding vibrational modes. In comparison, the acquired spectrum for the synthesized GO sample shown in Figure 4.2 displays the expected absorption bands present in GO such as O-H stretch at 3700 to 2500 cm^{-1}, C=O stretch at 1760 to 1690 cm^{-1}, and C-O-C stretch at 1250 to 1050 cm^{-1}.

Table 4.1: Principal infrared absorption bands and corresponding major vibrational modes for GO functional groups (Adapted from UCLA, 2001; University of Colorado, 2015) [Accessed on 8 Dec 2015]

Wavenumber (cm^{-1})	Bond activity	Functional group
3640–3610	O–H stretch	Hydroxyl
3500–3200	O–H stretch	Hydroxyl
3300–2500	O–H stretch	Carboxylic acid
1760–1690	C=O stretch	Carboxylic acid
1760–1665	C=O stretch	Carbonyl
1320–1000	C–O stretch	Carboxylic acid
1250–1050	C–O–C stretch	Carboxylic acid
1200–1020	C–OH stretch	Carboxylic acid
950–910	O–H bend	Carboxylic acid

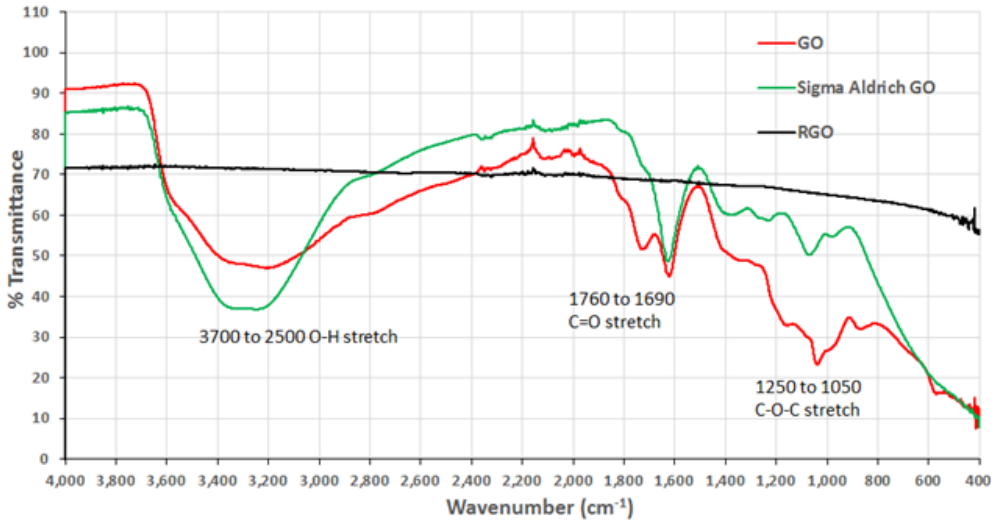

Figure 4.2: FTIR spectra for GO, RGO, and Sigma Aldrich GO with major absorption bands indicated

The unique profile of a spectrum with signature peaks and troughs can be used as a 'fingerprint' for the identification of a material. The sample spectrum of Sigma Aldrich GO was acquired for benchmarking purposes. By visually inspecting the two superimposed curves shown in Figure 4.2, we can see that they match up relatively well. Differences in the absorption intensities could be due to variations in the concentration of functional groups as a result of different oxidising conditions. As for minor differences seen in the absorption band wavenumbers, Zhang and Dabbs et al. (2015) developed mathematical models to demonstrate that lattice vacancies could induce both blue and red shifts in the prominent OH stretching and bending bands.

In contrast, the spectrum for RGO is free from any prominent absorption troughs and relatively infrared inactive with a transmission level of 60% to 70%. This slightly downward sloping and featureless profile indicate

low levels of residual functional groups pointing to the effectiveness of the hydrazine reduction process. From these test results, there is no reason to conclude that the samples tested were not GO and not RGO.

4.1.3 X-ray Diffraction (XRD) Spectroscopy

The acquired spectra of starter graphite (powder), RGO (powder) and GrO (flakes) are shown in Figure 4.3. Samples of the acquired raw data are shown in Appendix E.

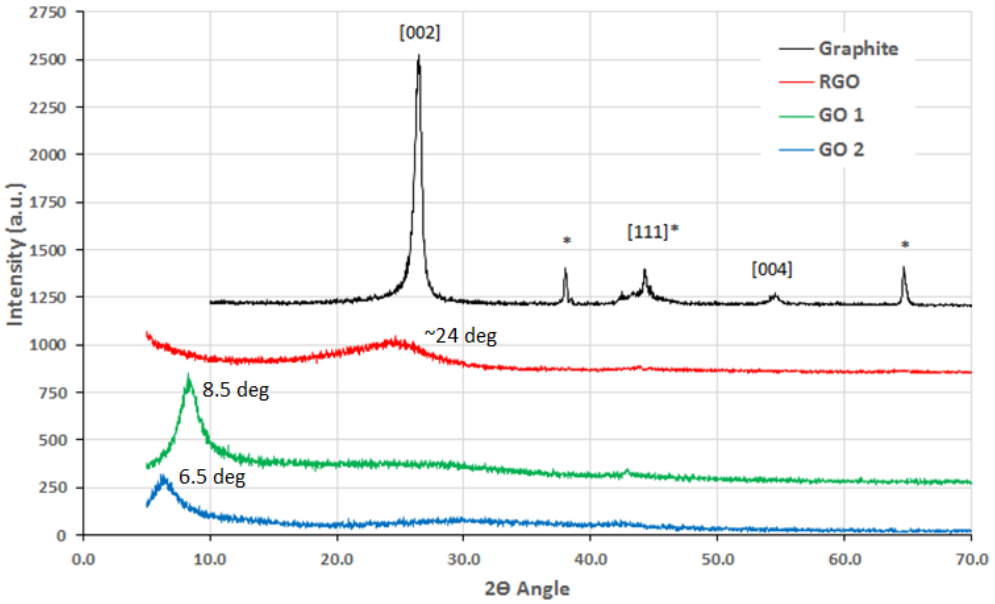

Figure 4.3: XRD spectra of starter graphite, RGO, GO 1 and GO 2. Graphite miller indices are shown in brackets. Asterisks denote spurious aluminium peaks emanated from the sample holder

Visual examination of Figure 4.3 shows that the starter natural graphite spectrum is almost free from an amorphous background and displays the three prominent graphite diffraction peaks at the Miller indices of [002], [111] and

[004] providing strong evidence that it is crystalline graphite. Note that the peaks marked with asterisks are spurious diffractions from the aluminium specimen holder. At the 44 degree 2θ position there is a slightly broad band created by the overlapping of the [200] aluminium peak, with the [111] graphite peak. Table 4.2 lists the diffraction angles, peak intensities, d-spacing and Miller indices for graphite (RRUFF, 2015a) and aluminium (RRUFF, 2015b) published by the public-private sponsored RRUFF Project created to collect a worldwide database for mineralogists, geoscientists, and the general public (Lafuente and Downs et al., 2015).

Table 4.2: Diffraction data for (a) Graphite and (b) Aluminium (Adapted from RRUFF, 2015a; RRUFF, 2015b)

(a) Graphite:

X-RAY WAVELENGTH: 1.541838
MAX. ABS. INTENSITY / VOLUME**2: 16.80109255

2-THETA	INTENSITY	D-SPACING	H	K	L
26.63	100.00	3.3480	0	0	2
42.50	4.61	2.1270	0	2	0
44.70	15.06	2.0272	1	1	1
50.86	4.46	1.7953	0	2	2
54.84	6.55	1.6740	0	0	4
60.09	4.52	1.5398	1	1	3
71.75	1.16	1.3155	0	2	4
77.77	1.77	1.2280	2	0	0
79.32	6.68	1.2079	1	3	1
83.93	2.86	1.1529	2	0	2
85.73	1.36	1.1333	1	1	5
87.38	1.30	1.1160	0	0	6

(b) Aluminium:

X-RAY WAVELENGTH: 1.541838
MAX. ABS. INTENSITY / VOLUME**2: 34.61439413

2-THETA	INTENSITY	D-SPACING	H	K	L
38.50	100.00	2.3380	1	1	1
44.76	47.49	2.0248	2	0	0
65.16	28.01	1.4317	2	2	0
78.30	30.71	1.2210	3	1	1
82.52	8.74	1.1690	2	2	2

When the GrO flakes samples were analysed, their spectra showed the absence of any graphitic diffraction peaks which implies that the starting material have been completely oxidized. The interplanar distance of graphite has expanded beyond 0.335 nm due to the intercalation of the d-spacing with functional groups (Marcano and Kosynkin et al., 2010).

The GrO samples tested were damp, with GO 2 being wetter than GO 1. The presence of the diffused peaks located at 8.5 degrees (d=1.0 nm) for GO 1 and 6.5 degrees (d=1.3 nm) for the wetter GO 2 are in line with the expanding effects of moisture (Lerf and Bucksteiner et al., 2006). According to Stankovich and Dikin et al. (2007), it is very difficult if not impossible to completely remove moisture from GrO. If the specimen GrO flakes were too dry it was even necessary to moisten them so that they could be securely compacted into the shallow indented cavity of the XRD diffractometer sample holder. Park and Ruoff (2009) postulated that the swelling effects of moisture caused the interplanar distance to vary from the lowest d-spacing value of d = 0.63 nm for dry GrO to d = 1.2 nm for hydrated GrO. From equation 3.1 (Bragg equation) it can be shown that this d-spacing range corresponds to a 2θ diffraction angle spanning from 7 degrees (d=1.2 nm) to 14 degrees (d=0.63 nm). This range agrees with the experimental results of Nakajima and Matsuo (1994) and Lerf and Bucksteiner et al. (2006). Since the peak locations of GO 1 and GO 2 are consistent with this range and are devoid of any graphitic peaks, it can be concluded that these samples contain fully oxidized GrO.

The spectrum of hydrazine reduced RGO sample displays only one diffused peak near the [002] peak of graphite at 26.4 degrees. This indicates a partial restoration of graphitic structures into disordered graphene sheets via the removal of oxygen containing groups (Gao and Ma et al., 2011).

4.1.4 Raman Spectroscopy

The Raman spectra of the starter graphite, GO, and RGO samples are shown in Figure 4.4 and their corresponding resonant band shifts are tabulated in Table 4.3.

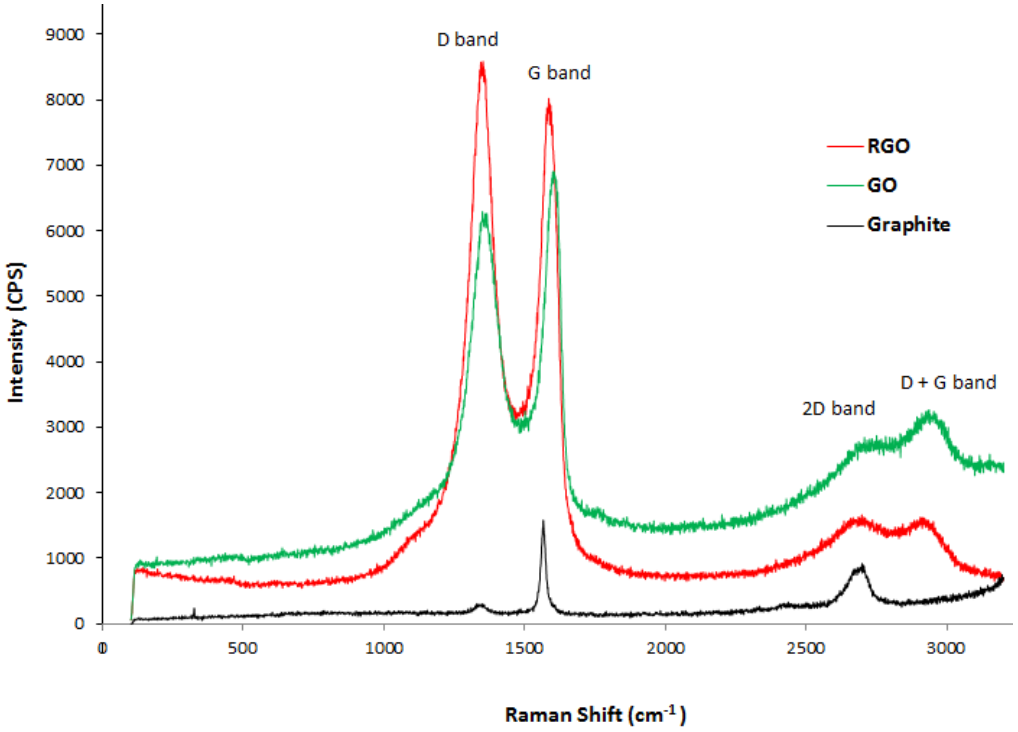

Figure 4.4: Raman spectra for graphite, RGO, and GO

Table 4.3: Raman resonant peaks for graphite, GO, and RGO at 2.41 eV laser excitation energy (wavelength=514 nm). For comparison, values published by Jorio (2012) and Ferrari (2007) are shown in the last two rows

Sample	Resonant peaks (cm^{-1})			
	D	G	2D (or G')	D+G
Graphite	1,349.4	1,565.4	2,697.7	2,937.7
RGO	1,351.5	1,584.8	2,704.6	2,945.1
GO	1,358.8	1,599.1	2,706.3	2,952.6
Jorio, 2012	1,350.0	1,580.0	2,700.0	2,935.0
Ferrari, 2007	1,360.0	1,560.0	2,710.0	Not stated

An inspection of the RGO and GO spectrum shown in Figure 4.4 reveals several general features consistent with those published by Jorio (2012) and Ferrari (2007). Prominent and narrow G peaks were detected at ~ 1,580 cm^{-1} band shift, followed by distinct and slightly broader D peaks at ~ 1,350 cm^{-1} band shift while a diffused pair of peaks were detected at the 2D (or G') ~ 2,700 cm^{-1} and the D + G bands ~ 2,935 cm^{-1} band shifts.

The G band shifts are produced by single-resonant scattering involving C-C bond stretching within the in-plane direction. According to various published literature, the G peak is positioned from 1,560 to 1,582 cm^{-1} (Ferrari and Basko, 2013; Jorio, 2012; Ferrari, 2007). In Figure 4.10, RGO has a higher G peak compared to GO due to the recovery of sp^2 domains from the removal of in-plane functional groups. The position of the G band is not sensitive to the number of layers as shown in Figure 4.5 (left).

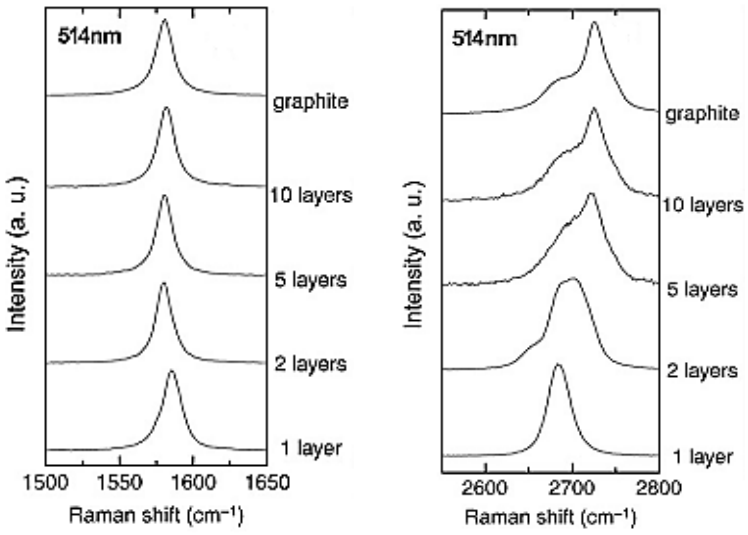

Figure 4.5: Evolution of G band (left) and 2D band (right) with respect to layer thickness (Adapted from Ferrari, 2007)

The D band arises from double-resonant interactions emanating from edge defects (Jorio, 2012). According to Ferrari and Basko (2013), edges are regarded as extended defects by breaking the translational symmetry of the aromatic rings, unless they retain a perfect zigzag or armchair shape which will then still preserve the symmetry along the edge and thus not contribute to the D band intensity. This account is useful in explaining the small D peak of graphite followed by the intense and diffused peak for GO due to the presence of functional groups breaking up the lattice edges during the oxidation process. According to Huang and Lim et al., (2011), when GO flakes are dispersed via ultrasonication prior to the reduction process edge damage will be introduced due to tearing of the exfoliated sheets. There are also dangling bonds left behind after the removal of oxygenated functional groups. According to Stankovich and Dikin et al. (2007) the average size of the recovered sp^2 domains are also smaller compared to their prior dimensions as

sp^3 sites in the exfoliated GO sheets. Therefore RGO has a more intense D peak compared to GO because it contains relatively more disordered edges.

The 2D band is an overtone of the D band. For pristine single layered graphene (SLG), a very intense 2D peak is detected at a Raman shift of slightly less than 2,700 cm^{-1}. This feature is used as the fingerprint for confirming SLG. When the layers increase to two layers and beyond, the 2D band will evolve from a sharp single peak to broader convoluted peaks as shown in Figure 4.5 (right). The difference between the spectrum of SLG and that of graphite can be clearly distinguished by examining their G and 2D bands as shown in Figure 4.6. Note that the 2D to G peak ratio (I_{2D} / I_G) is less than unity for graphite and greater than unity for SLG. The number of layers present can be derived from the ratio of the I_{2D} / I_G peak intensities, as well as the position and shape of these peaks as discussed earlier (Childres and Jauregui et al., 2013).

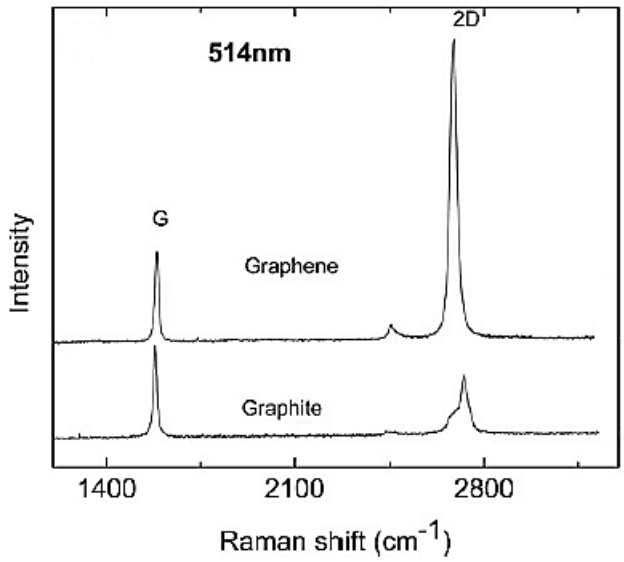

Figure 4.6: Raman shift of single-layered graphene (top) versus graphite (Adapted from Ferrari, 2007)

The RGO and GO spectra showed in Figure 4.4 display prominent but slightly broad D and G bands with low intensity diffused 2D and D + G bands. For RGO, these features can indicate the presence of edge defects and in-plane disorder and impurities in the crystal lattice. Since the I_{2D} / I_G peak ratio is less than unity, the RGO obtained is multi-layered. Unfortunately, due to the high level of diffusion present in the 2D peak the number of layers cannot be resolved. The peak intensities and ratios for the D, G, and 2D bands are summarized in Table 4.4.

Table 4.4: Peak intensities and intensity ratios

Sample	Peak intensity (cps)			Intensity ratio	
	I_D	I_G	I_{2D}	I_D/I_G	I_{2D} / I_G
Graphite	305.85	1,583.65	922.46	0.19	0.58
RGO	8,583.03	7,936.18	1,531.97	1.08	0.19
GO	6,260.47	6,900.84	3,243.24	0.91	0.47

Stankovich and Dikin et al. (2007) obtained similar D and G band profiles as shown in Figure 4.7. Note that the near zero intensity of the D band for graphite is explained by the low defect purified natural graphite used.

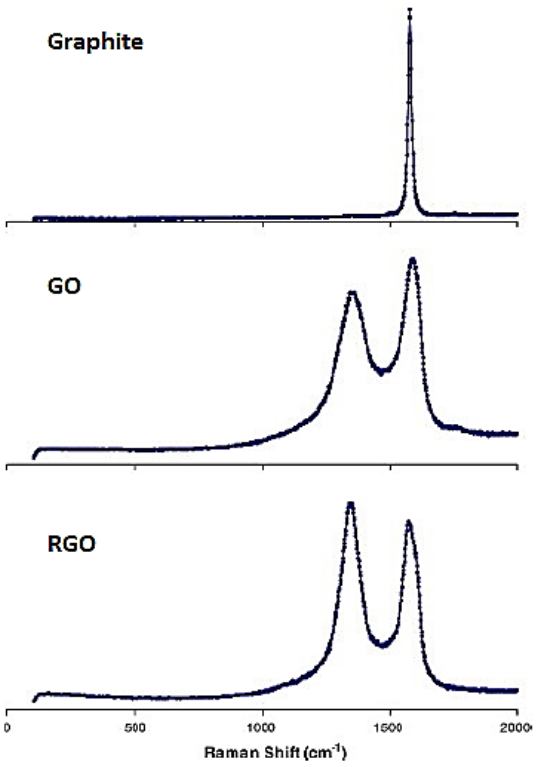

Figure 4.7: Raman spectra showing D and G bands for graphite, GO, and RGO (Adapted from Stankovich and Dikin et al., 2007)

Based on the preceding discussions on the Raman spectroscopy results, it can be concluded that the synthesized RGO is consistent with that produced by the process developed by Stankovich and Dikin et al. in 2007.

4.1.5 X-ray Photoelectron Spectroscopy (XPS)

Figures 4.8 and 4.9 are the broad survey scans for GO and RGO generated by the XPS energy analyser. The O KLL peaks are Auger electron signals and therefore can be ignored.

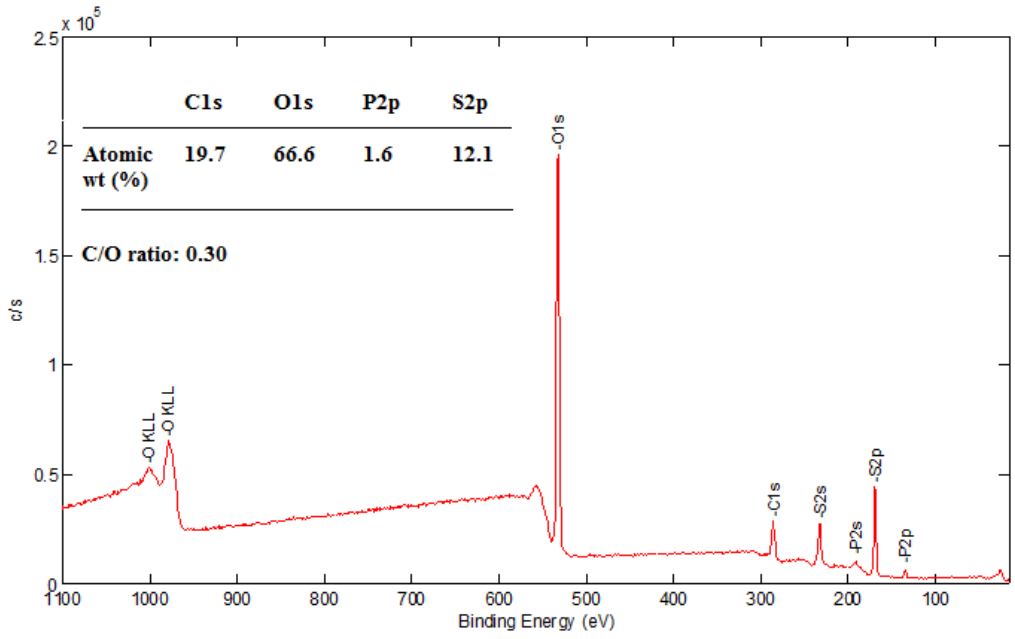

Figure 4.8: XPS broad survey scan for GO

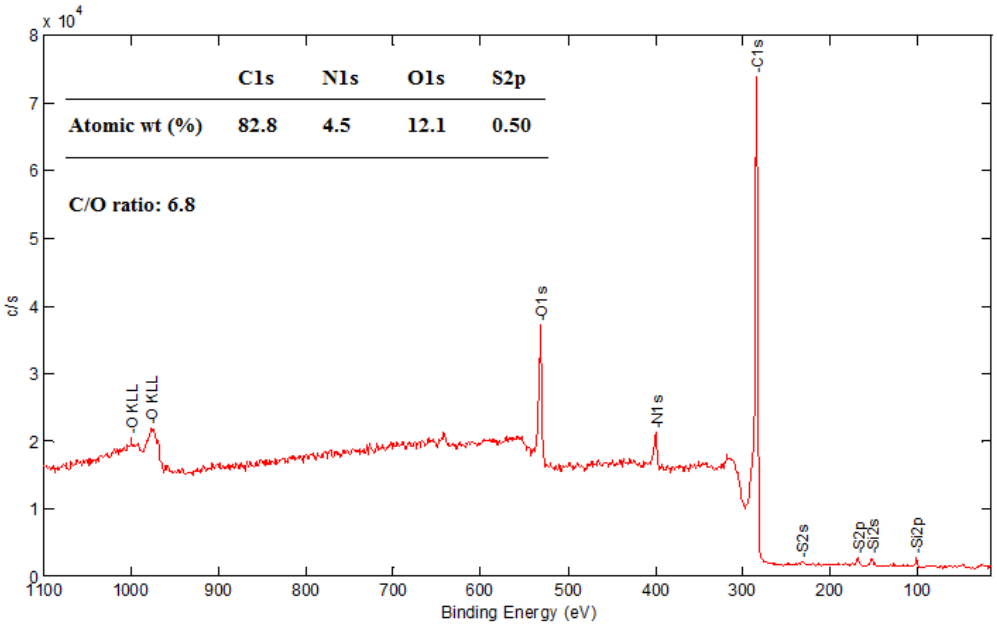

Figure 4.9: XPS broad survey scan for RGO

As expected the survey scan for GO shown in Figure 4.8 contains a sharp and intense oxygen peak at the O1s position with the presence of a relatively small carbon C1s peak. There are also prominent phosphorous and

sulphur peaks present. But unexpectedly, the C/O ratio of 0.30 is much lower than the 2.7:1 ratio reported by Stankovich and Dikin et al. (2007). This lowered ratio is very likely due to the oxygen contained in the residual phosphate and sulphate salts probably as a result of the inadequate wash process.

As for the RGO broad survey scan shown in Figure 4.9, the C/O ratio of 6.8 indicates a significant removal of oxygen bearing functional groups via the hydrazine reduction process. This observation is corroborated by the FTIR results discussed earlier in section 4.1.2. In comparison, Dreyer and Park et al. (2010) reported a C/O ratio in the range of 2.8 to 6.2 for RGO films, while Marcano and Kosynkin et al. (2010) reported a C/O ratio of around 10:1 for RGO that have been thermally annealed. Note that phosphorous peaks are no longer present while sulphur peaks have been reduced to near zero levels most likely because the sulphate and phosphate salts were removed during the RGO wash process. The detection of minor silicon peaks could be due to contamination from the glassware used.

The presence of a significant nitrogen N1s peak at a C:N ratio of 18.4:1 is caused by doped nitrogen atoms from the hydrazine used. During the reduction process, nitrogen atoms tend to form covalent bonds at the surface of GO sheets while the oxygen bearing groups are being removed resulting in amines, hydrazones, aziridines and other similar structures. Functioning as an n-type dopant, such heteroatomic impurities have a profound disrupting effect

on the sp^2 structure of the final RGO lattice. According to Dreyer and Park (2010), the C to N doping ratio can go as low as 16:1.

The deconvoluted narrow scans at C1s for GO and RGO with the appended binding energies of the various bonds are shown in Figures 4.10 and 4.11 respectively. C-C denotes carbon to carbon sp^2 bond, C-O denotes single hydroxyl bond and epoxide functionality, C=O denotes carbonyl bond, C(O)O denotes carboxylic bond, and pi – pi* transition denotes the π bond to π anti-bond transition. The binding energies were produced by the PHI-Quantera XPS spectrum analyser software. These values are consistent with those published by Park and An et al. (2011), Marcano and Kosynkin et al. (2010), and Stankovich and Dikin et al. (2007).

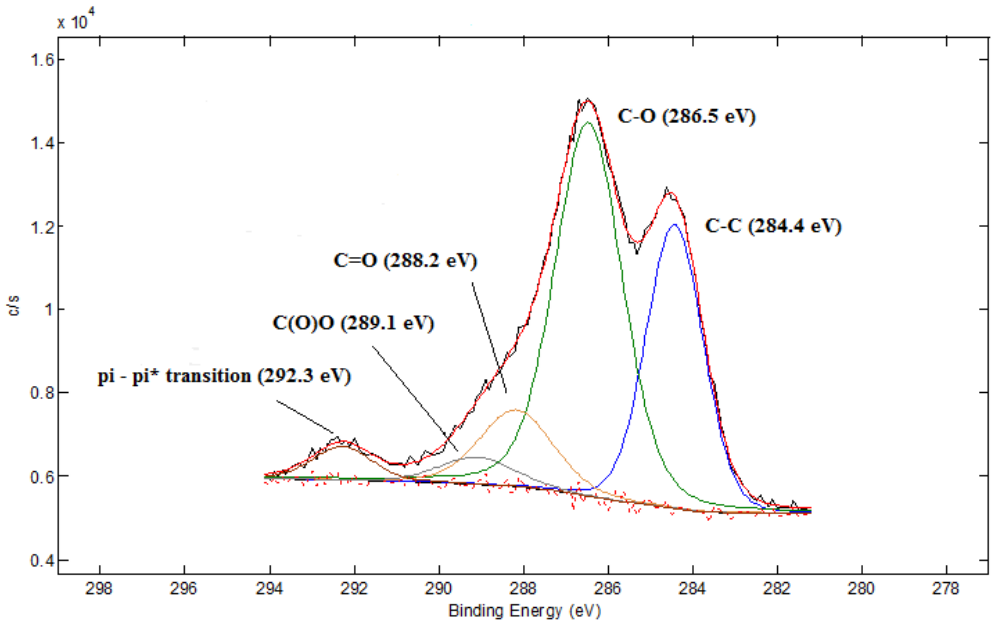

Figure 4.10: XPS deconvoluted C1s spectrum for GO

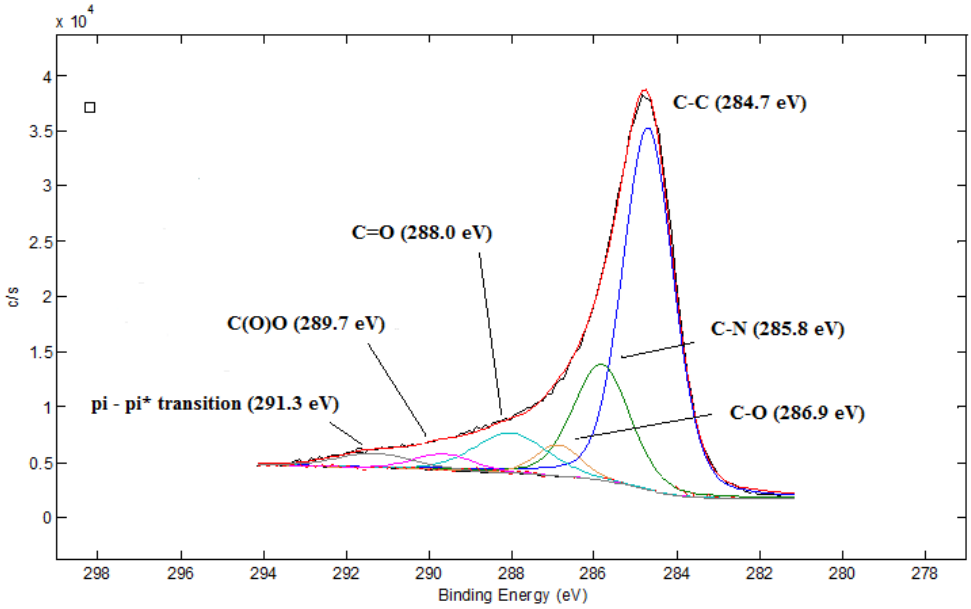

Figure 4.11: XPS deconvoluted C1s spectrum for RGO

The highly oxygenated GO spectrum and the largely deoxygenated RGO spectrum are consistent with the curves published by Park and An (2011) shown in Figure 4.12. In terms of C-O/C-C bond evolution, the purity of RGO from figure 4.11 is calculated at a C-O/C-C ratio of 0.16 in contrast with its precursor state calculated at a ratio of 1.21 as shown in figure 4.10.

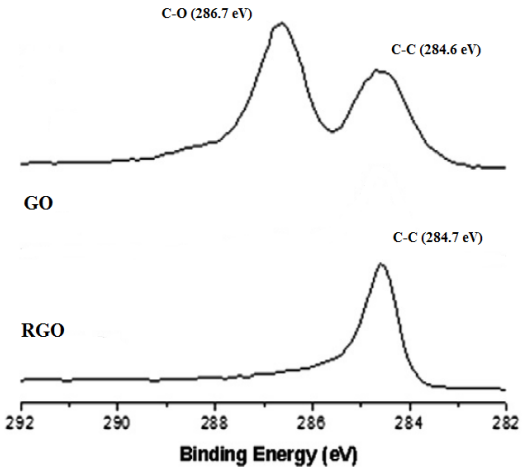

Figure 4.12: XPS C1s spectra for GO and RGO (Adapted from Park and An, 2011)

In summary, the XPS elemental analysis results point to a highly oxidized GO which contained some residual sulphate and phosphate salts that were eventually removed during the RGO reduction process. The synthesized RGO was well deoxygenated consistent with the ranges published in highly cited research articles and contained doped nitrogen due to the hydrazine (reducing agent) used.

4.1.6 Electron Microscopy

The FESEM image of the Asbury Carbon Nano 25 grade graphite flakes used as starter material for the synthesis of GO is presented in figure 4.13.

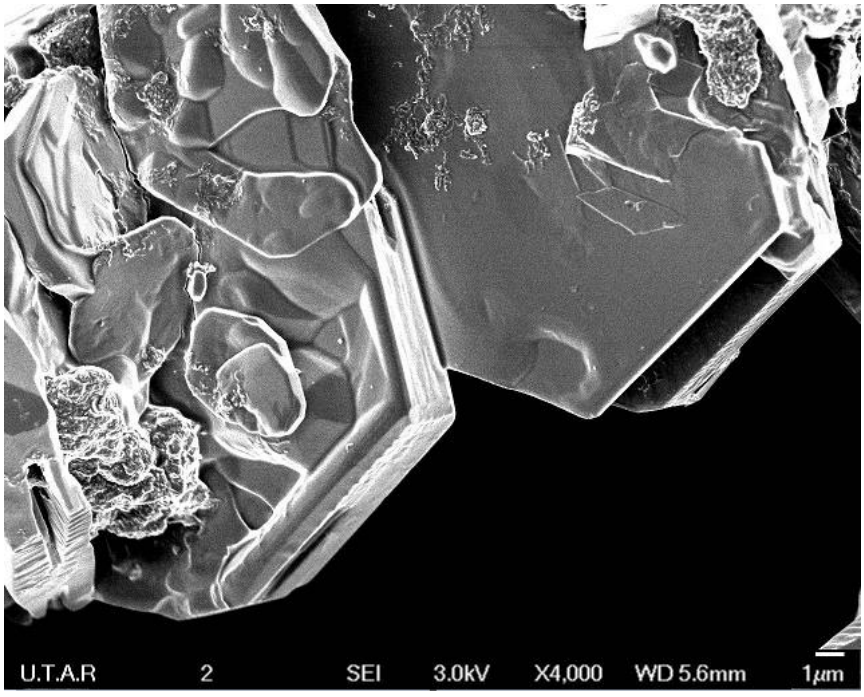

Figure 4.13: Asbury Carbon Nano 25 grade natural graphite flakes

This grade of graphite was selected because it was processed from natural graphite into thin flakes of several microns to tens of microns in dimension to specifically facilitate the intercalation of the graphite d-spacing with oxygenated functional groups. The presence of pristine graphitic hexagonal crystal lattice can be clearly seen. However some rounded edges on the stacked features indicate edge damage probably sustained during production. Note that the presence of impurities (see bottom left hand and top right hand corners) is likely to be amorphous carbon residue because an EDX analysis showed that the material contained only carbon (97%) and oxygen (3%).

Figure 4.14 is the FESEM images of dried GO flakes showing prominent surface folds at different magnifications.

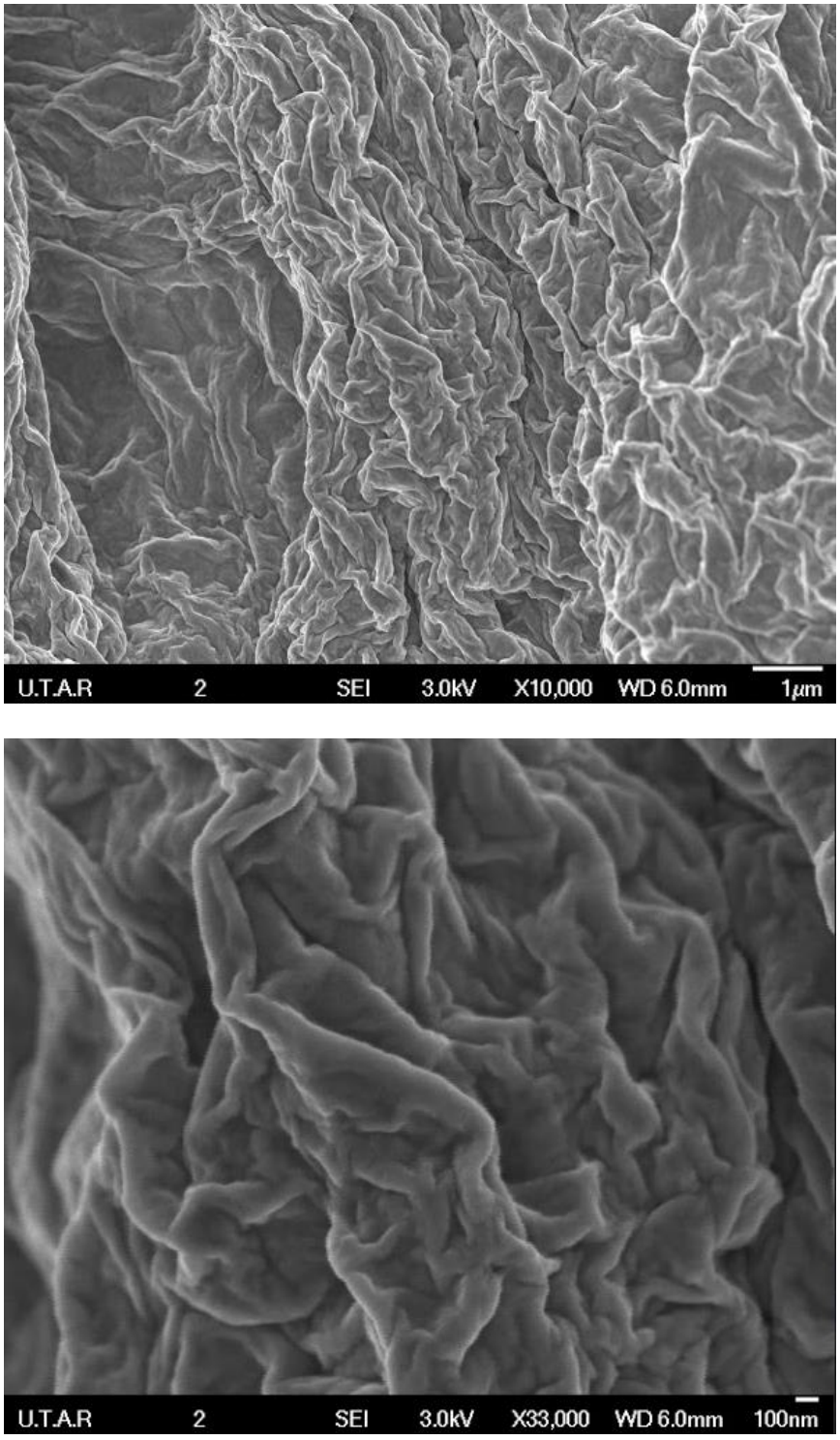

Figure 4.14: FESEM images of dried GO flake. Compacted thick folds feature prominently at X10k magnification (top) and X33k (bottom) magnified close-up view

Figure 4.15 displays the FESEM images of dried RGO particles showing stacked agglomerates with corrugated wrinkled surface morphology.

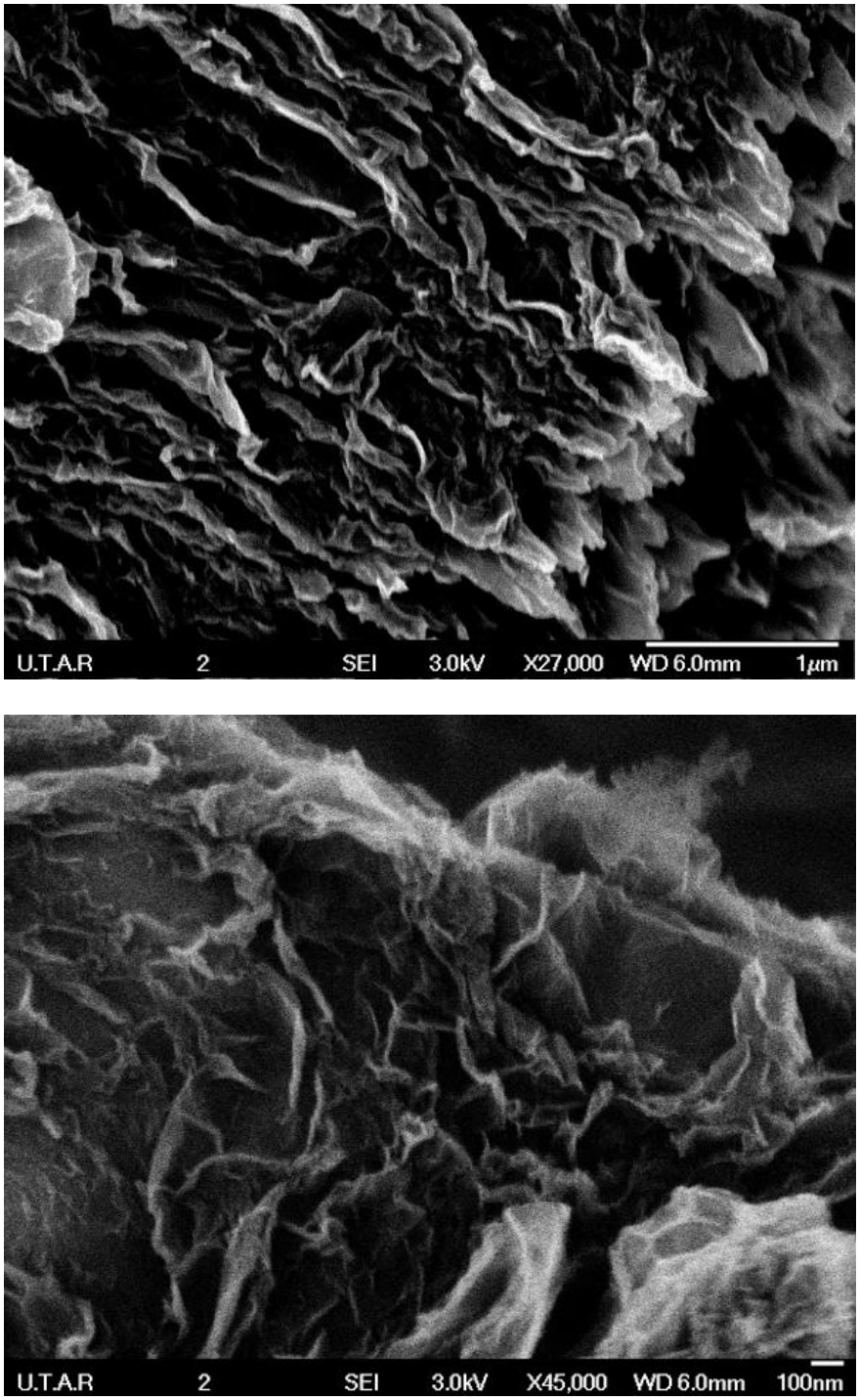

Figure 4.15: FESEM images of dried RGO particles. Edge view shows stacked agglomerated sheets of graphene (top) and X45k magnified surface view showing the wrinkling effect of single or few layered graphene

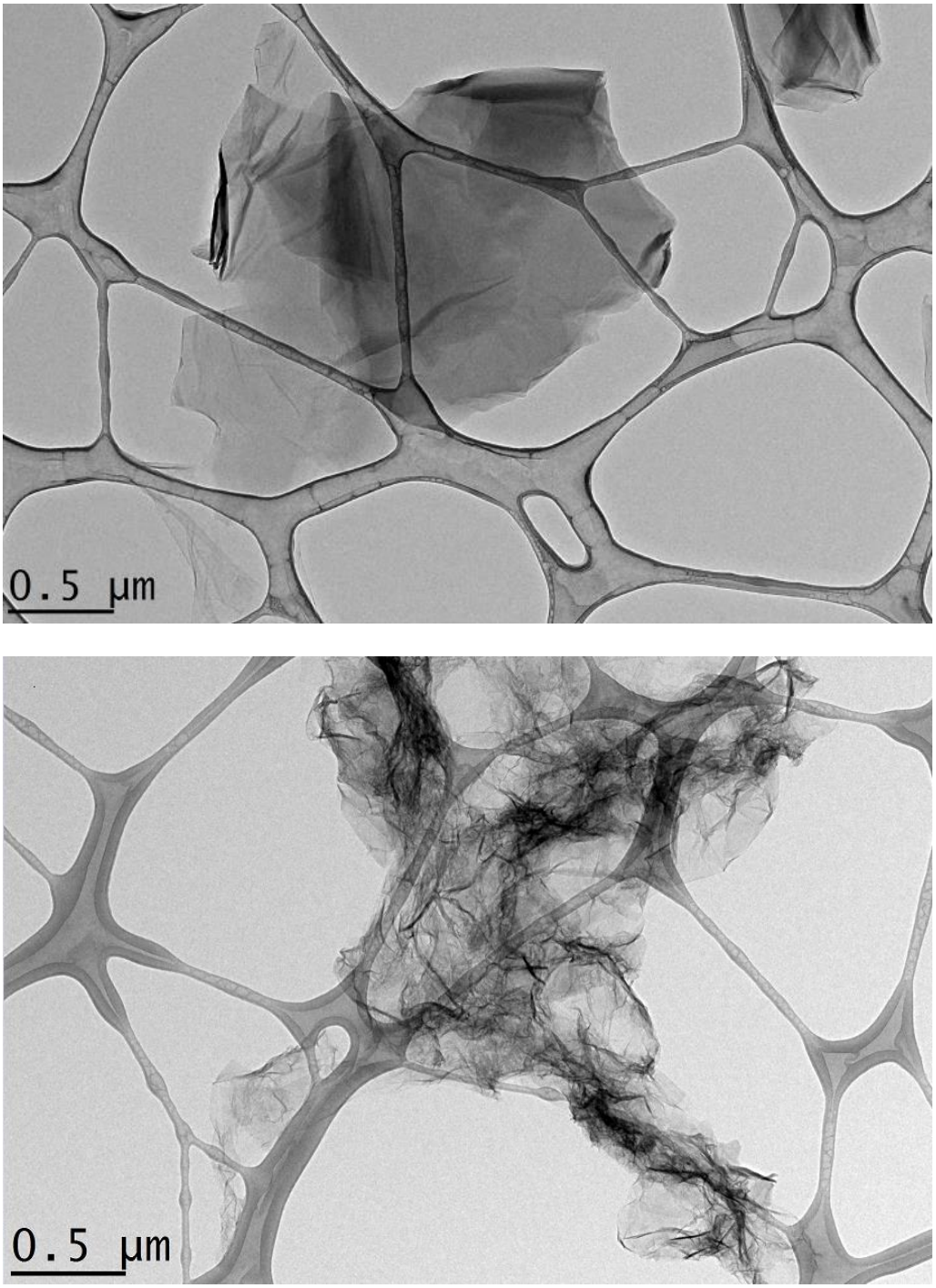

Figure 4.16: HRTEM images at X6.3k magnification for GO (top) and HRGO (bottom) sheets suspended on lacey carbon TEM grid. Dried GrO flakes and RGO particles were ultrasonicated for 30 minutes in ethanol, drop casted and air dried

HRTEM high resolution images were obtained for exfoliated GrO and RGO sheets to study their surface and edge morphology. Visual inspection of

low magnification HRTEM images for exfoliated GrO and RGO sheets shown in Figure 4.16 reveal a distinct difference between the two materials. Being thicker due to the presence of functional groups attached to the basal plane, the GO sheet(s) appear relatively flat and less crumpled compared to the RGO sheet(s) which is wrinkled and contains many folded and crumpled zones. At a higher magnification, the characteristic wrinkling and corrugated features of the suspended RGO sheet are clearly visible as shown in Figure 4.17. Note that the curling or scrolling at the unsupported hanging edges visible at the bottom of the figure is a common feature of single and few layered graphene sheets according to Meyer and Geim et al. (2007)

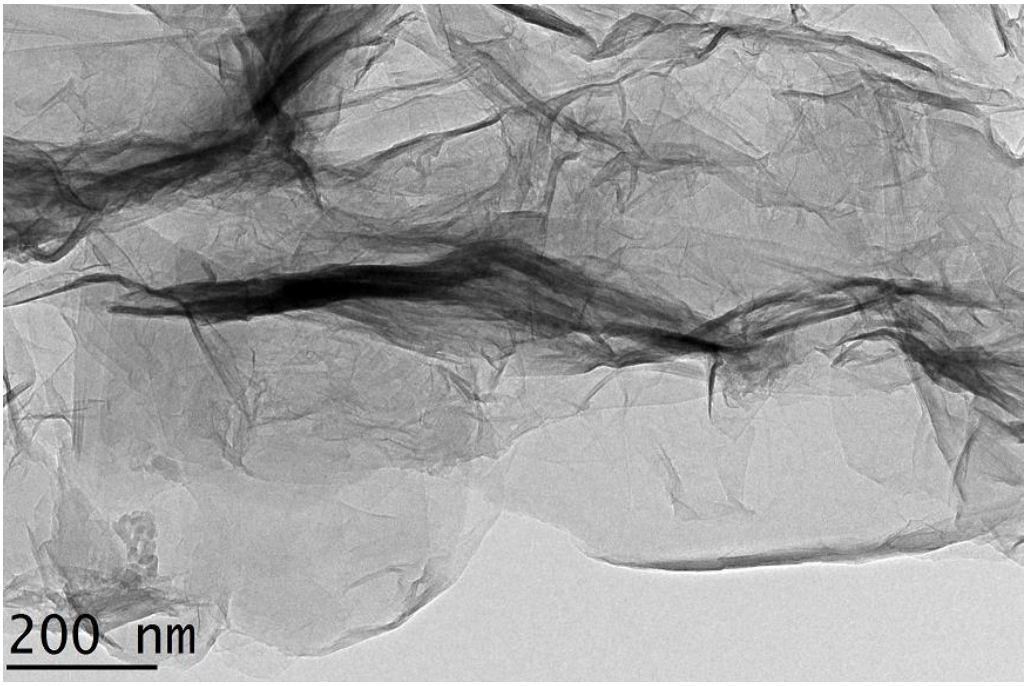

Figure 4.17: RGO at X17.5k magnification revealing the wrinkling, folded and heavily crumpled features with scrolled edges (bottom of image) of freely suspended single and/or few layered graphene sheets

At higher magnifications, the number of layers in a graphene sheet will only be visible if wrinkled or folded sheets are imaged at an angle

perpendicular to the fold. This is not difficult to accomplish because folded regions are abundantly present in the sample. Figure 4.18 shows an image at X255k magnification with a 5-layered sheet thickness.

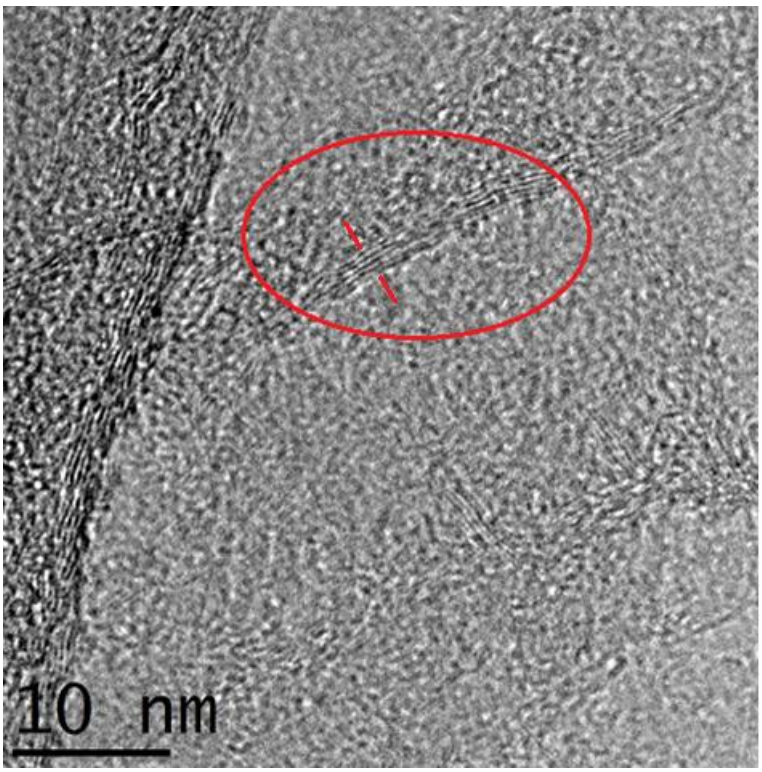

Figure 4.18: Folded region of few layered RGO sheet at X255k magnification. A wrinkled feature (inside red oval) viewed from one side revealing a 5-layered sheet thickness at ~ 0.335 nm sheet distance

An explanation of how the number of layers can be resolved via HRTEM imaging is illustrated in Figure 4.19 by Meyer and Geim et al. (2007).

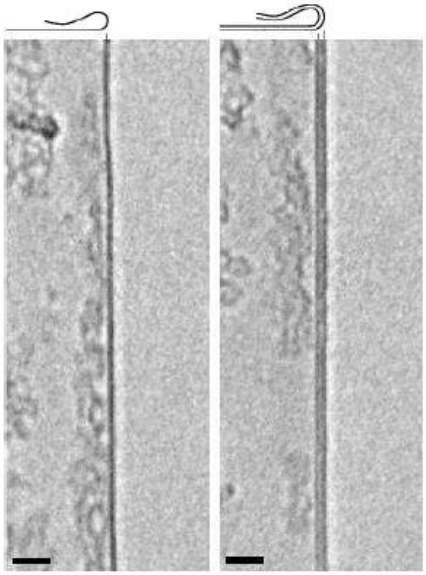

Figure 4.19: How folded (including wrinkled and creased) sheet edges show up in a TEM image according to Meyer. Scale bars = 2nm (Adapted from Meyer and Geim et al., 2007)

With selected area electron diffraction (SAED) spectroscopy, a selected area of the HRTEM image can be tested to determine if the sample is crystalline, polycrystalline, or amorphous. Figure 4.20 is an image of RGO obtained at 800k magnification showing an amorphous basal plane.

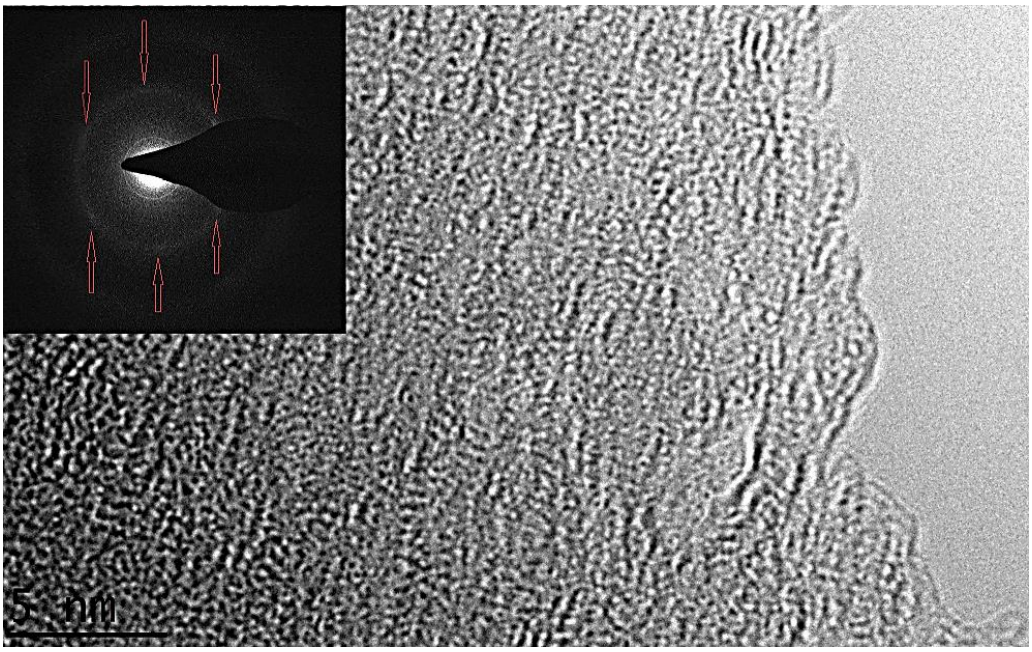

Figure 4.20: RGO at X800k magnification showing disordered basal lattice structure and an irregular edge. SAED diffraction pattern (inset) indicates a highly amorphous structure. Faintly visible graphitic hexagonal diffraction spots are pointed out with red arrows

The lack of crystalline structure in the SAED diffraction pattern was most likely caused by the destructive power of the high energy electron beam set at 200keV while the image was being acquired. According to Kotakoski and Meyer (2011), point defects especially vacancies are naturally created by the "knock-on" effect from energetic electrons if the threshold beam energy of 100 keV is exceeded. This effect is more acute at higher magnifications and at longer dwell times. The skill of the HRTEM imaging operator is thus very important in determining the quality of the images obtained. Fortunately, the young operator at MIMOS subsequently improved his technique and managed to obtain better quality GO and RGO images. Figure 4.21 (used with permission) is an image of RGO produced by Tan (2015) in her Final Year Project work at UTAR using Marcano's process showing a clear graphitic

crystalline lattice structure even though the lattice sustained some damage during image acquisition.

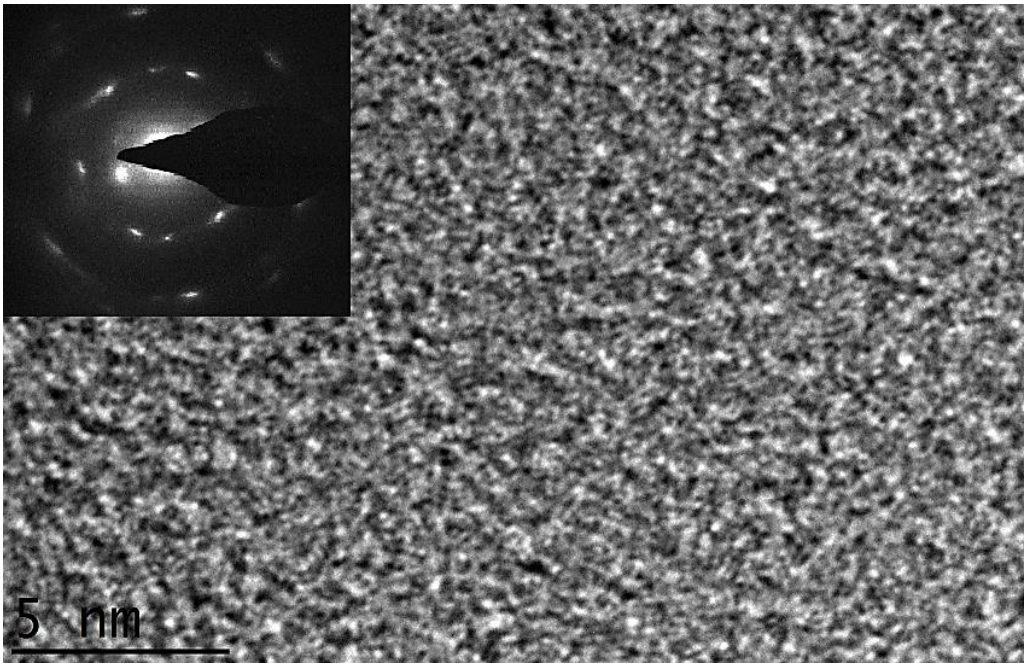

Figure 4.21: RGO (Marcano's process) at X930k magnification (Adapted from Tan (2015) with permission)

Damage caused by the HRTEM imaging process notwithstanding, it was also pointed out in section 2.3.3 of the literature review that the wet reduction of GO to RGO is a process which produces inherent edge and basal plane lattice defects. An RGO image populated with basal plane vacancies not exceeding 100 nm across is shown in Figure 4.22. Any damage caused by the electron beam is minimal because the image was acquired at a relatively low 26.5k magnification where the destructive effects of the beam are spread out over a wider area.

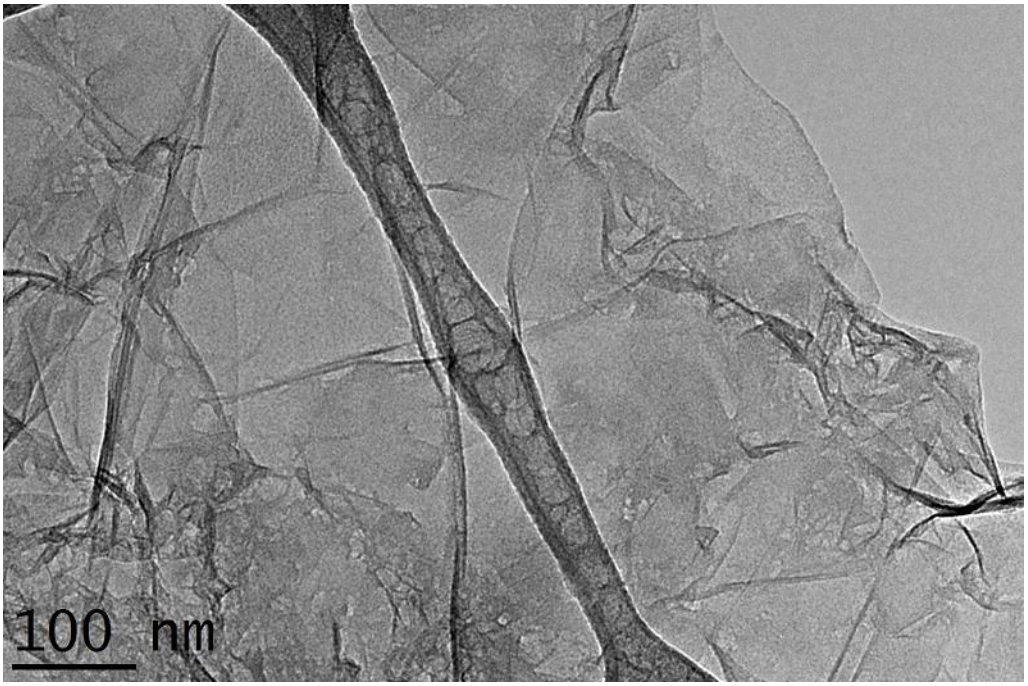

Figure 4.22: RGO at X26.5k magnification. Basal plane with vacancy type lattice defects visible at bottom left region of image

In summary, the FESEM and HRTEM image analysis showed that GO and RGO can be identified and differentiated. The synthesized RGO sheets were few layers thick and their surface and edge morphology contained defects such as vacancies and disordered non-crystalline lattice structures. Supplementary images are shown in Appendix B.

4.2 Rheological Characterization

The rheological properties of the RGO filled epoxy samples were studied per the formulations listed in Table 3.1. The 25 mm diameter parallel plate gap distance was fixed at 0.5 mm and temperature controlled at 25 ºC. Following are the results and discussions for the flow and oscillatory rheological test

measurements made. Samples of rheometer raw data are shown in Appendix C.

4.2.1 Constant Shear Test

The constant shear test is a flow study that will give an indication of fluid stability under shear over time. The stencil or screen printing process typically used for the application of the liquid ICA operates over a period of seconds at the shear rate of around 10 to 10^2 s^{-1} (Barnes, 2000). Therefore a shear rate ($\dot{\gamma}$) of 50 s^{-1} was selected to obtain viscosity measurements and provide a fundamental understanding of the matrix under this constant flow condition.

All the curves in Figure 4.29 are flat. This means that the samples do not shear thin thus displaying a stable Newtonian like behaviour within the experimental time interval of 120 s. The measured viscosity of 4.38 Pa.s for neat epoxy is within the range specified by the manufacturer (Sigma-Aldrich, 2015). The measurements for the oven-dried RGO samples were omitted because the data points obtained were highly erratic due to the coarse particles breaking up in the matrix while the samples were being measured. Because of this, the oven-dried samples were left out of all subsequent experiments.

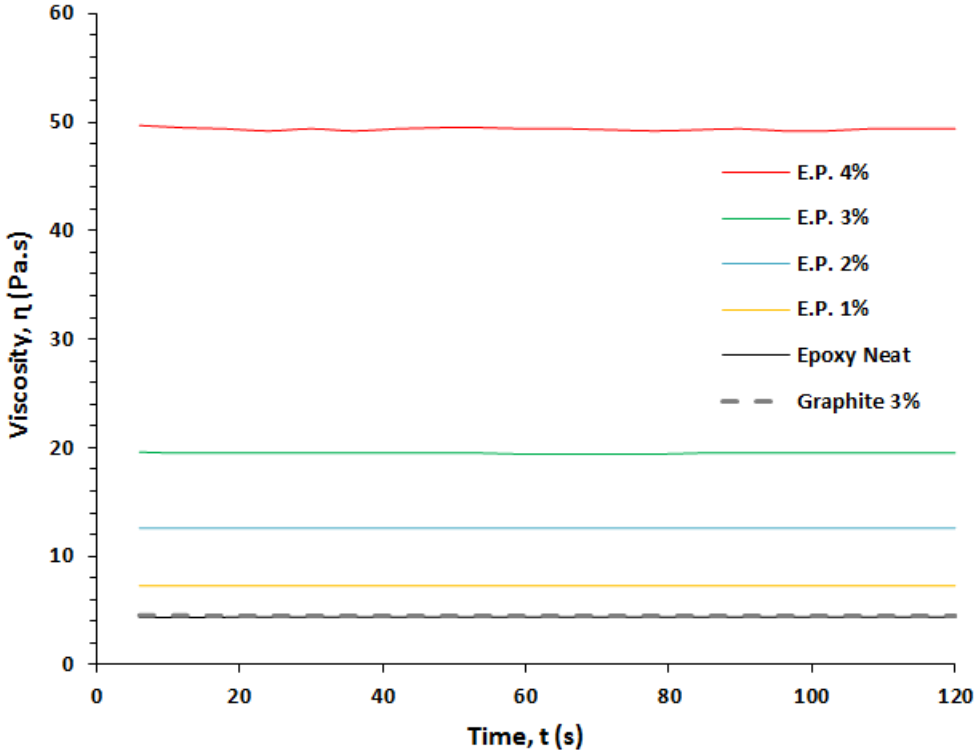

Figure 4.23: Viscosity measurements at constant shear rate ($\dot{\gamma}$) 50 s^{-1}

The viscosity of the samples increased non-linearly with the increase in filler loading starting at a viscosity of 7.3 Pa.s at 1% filler loading reaching a value of 50 Pa.s for the E.P. 4% sample. Viscosity is the resistance of a fluid to flow. The presence of the agglomerated irregularly shaped granular RGO particles provides this resistance by impeding the flow of the DGEBA molecules past each other. Interestingly, the viscosity of the 3% graphite filled benchmark sample at 4.39 Pa.s was not significantly larger than that of the neat epoxy. This can be explained by the low resistance smooth laminar flow between the shear planes due to the lubricating effect of the uniformly aligned graphitic micro sheets. But as the concentration of the non-uniform granular RGO particles increased, the flow of the DGEBA molecules probably became even more turbulent thus increasing the viscosity significantly along the way.

4.2.2 Hysteresis Loop Test

It was pointed out in the literature review section that Newtonian fluids will display non-Newtonian like behaviour when subjected to high enough shear rates. The hysteresis loop test is a flow test that can reveal the shear thinning (or thickening) profile together with any time-dependent property (thixotropic characteristic) of a fluid.

Figure 4.30 illustrates the curves of the hysteresis loop tests conducted on the experimental samples where the shear rate was increased from zero to 600 s^{-1} over a 160 s duration and reversed along the same path back to zero following a 15 s constant shear interval at 600 s^{-1}. The graphite 3% sample curve is omitted because it overlaps with the epoxy neat curve.

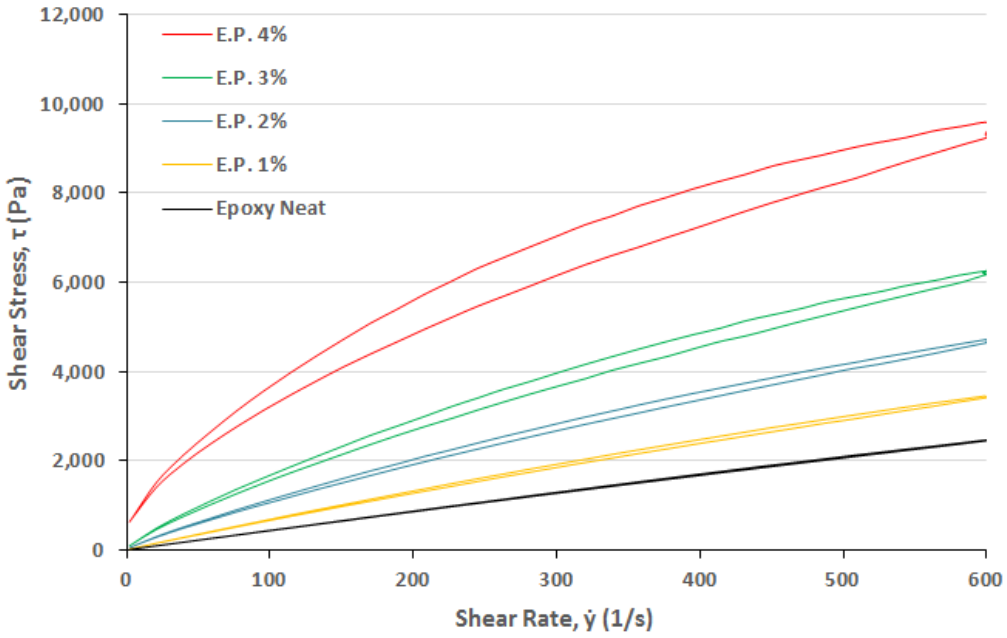

Figure 4.24: Hysteresis loop curves

The unfilled epoxy sample does no exhibit a clear hysteresis loop (refer to Figure 2.22 for a typical example) since the forward and return stress curves overlap each other. The near linear shape also points to minimal shear thinning. This result supports the earlier conclusion from the constant shear test that pure epoxy is an unstructured Newtonian like fluid.

When epoxy is filled with 1% RGO, a very narrow hysteresis loop appeared. This shear thinning effect is most likely caused by the breakdown of the matrix micro structure created by the presence of RGO particles in the matrix. A schematic of this phenomenon is illustrated in Figure 2.17 where completely unstructured or minimally structured fluids exhibit shear thinning behaviour. As the content of the filler increases the hysteresis loop became more prominent with the 4% filled sample showing the largest loop with a distinct time dependent drop in shear stress before the return curve. This presence of a looping feature accompanied with a drop in shear stress during the constant shear interval is a characteristic of thixotropic materials (Barnes, 2000).

The relative overall increase in shear stresses corresponding to the filler content supports the finding of the constant shear test that viscosity increased along with filler concentrations. The fact that the return shear stress curve of every sample ended at their points of origin indicate that the matrix managed to recover to their initial rest structures. This is noteworthy because the RGO filled epoxy composites did not suffer any permanent breakdown and thus are very stable within these shear conditions.

4.2.3 Amplitude Sweep Test

Figure 4.31 illustrates the amplitude sweep curves conducted at a fixed angular frequency (ω) of 10 s^{-1} over a strain (γ) range of 0.01 to 100 (%). The distinct linear viscoelastic regions (LVERs) of the 2% to 4% RGO filled samples extended up to the 1% limiting strain level beyond which non-linear behaviour started to gradually emerge. From around 10% strain onwards the samples transitioned into the non-linear viscoelastic region. Hence the midpoint of 5% strain was selected as the parameter for the frequency sweep test since the amplitude sweep test is an oscillatory test designed to elucidate the viscous and elastic (if present) behaviour of a sample by measuring the G' (storage modulus) and G" (loss modulus) values when subjected to an increasing oscillatory shear strain at a fixed strain rate.

With the exception of the 4% RGO filled sample, the rest of the samples displayed liquid-like behaviour because their loss moduli G" were always above their storage moduli G' and also did not display any cross-over points throughout the full range of the experiments. The 4% filled RGO displayed a different characteristic from the rest of the samples at which its storage modulus G' dominated the loss modulus G". This indicates that beyond 3% filler loading, there exists a threshold at which the RGO matrix transitioned from liquid-like to solid-like behaviour from a rheological perspective. This observation corresponds well with the difficulty encountered during the hand mixing of the sample when the dispersion of the particles took longer than usual due to its thick and tacky consistency.

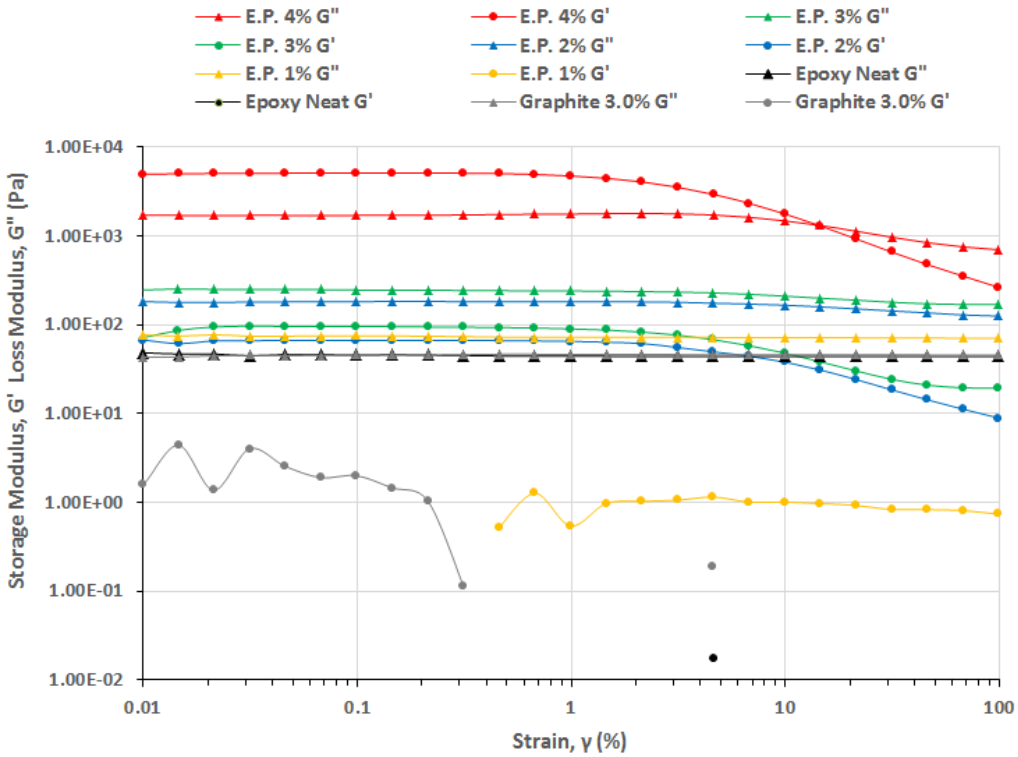

Figure 4.25: Amplitude sweep curves at ω = 10 s^{-1}

As for the epoxy neat, E.P. 1%, and the graphite 3% samples their low and unstable G' curves accompanied with prominent G" curves yielding large loss tangent (δ) values (δ = G"/G' refer to equation 2.11) in the range of 10 to 10^4. A loss tangent value of greater than one indicates that the material is viscous in nature and the larger the δ value the more dominant the viscous behaviour is. In the case of unfilled epoxy at the point where G"/G' is 46/0.018, the loss tangent is a massive 2,556 pointing to a viscous fluid with a virtually non-existent Hookean elasticity characteristic. This result corroborates the findings from the constant shear and hysteresis loop tests.

4.2.4 Frequency Sweep Test

Following the amplitude sweep test, the amplitude of the frequency tests were fixed at 5% strain (γ) and the experimental results are shown in Figure 4.32. The frequency sweep is an oscillatory test at which the amplitude of oscillation (a value around the LVER identified from the amplitude sweep test where the internal structure is expected to remain stable) is held constant while the angular frequency of oscillation (ω) is typically varied over a range of 10^{-1} to 10^{2} s^{-1} (Willenbacher and Georgieva, 2013; Barnes, 2000).

The shape and the magnitude of the frequency sweep curves depend largely on the internal structure of the material. The behaviour of the samples started at the rubbery/plateau region then moved into the leathery/transition zone within the experimental frequency sweep range with the 4% RGO filled epoxy demonstrating the second G'/G" crossover point at $\omega = 10$ s^{-1} to demark the onset of the transition between the two zones (refer to Figure 2.25. for an illustration of the general shape of viscoelastic behaviour). The almost overlapping G' and G" moduli of the neat epoxy up to the 3% RGO filled samples indicate that little internal structure exists at those concentrations. As detected at the constant shear, hysteresis loop, and amplitude sweep tests, the 4% filler concentration level imparted a structural behaviour to the epoxy matrix not apparent in the other samples.

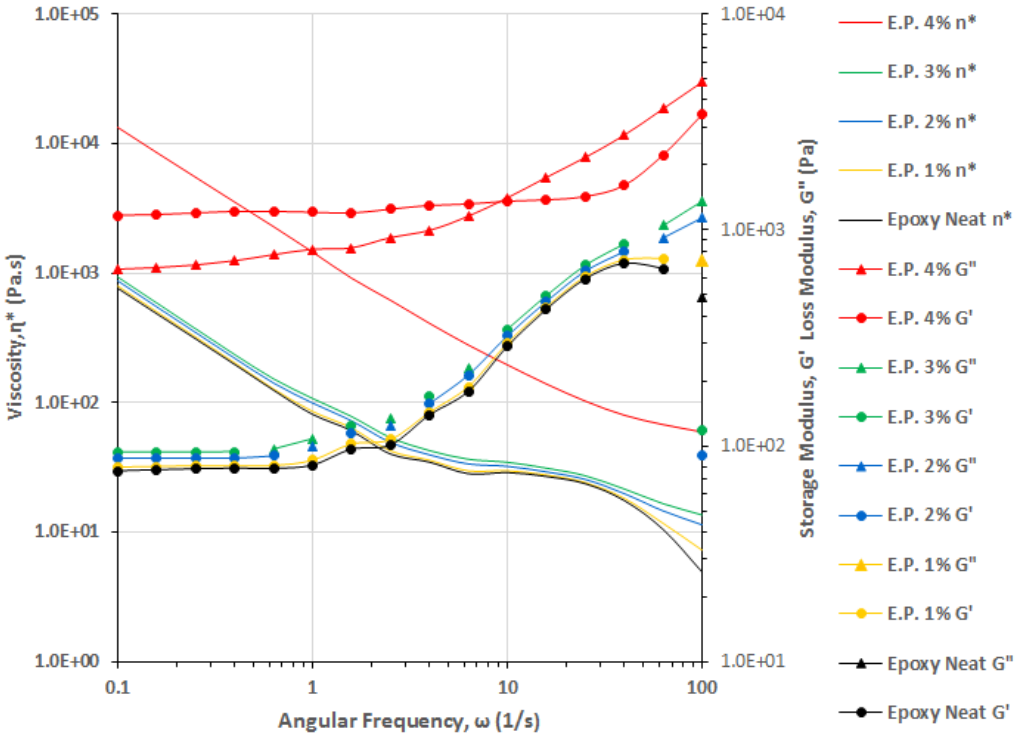

Figure 4.26: Frequency sweep at γ = 5%

As the angular frequency is increased, the short-term time-dependent behaviour of the material dominates leading to an increase in rigidity in the matrix. The downward sloping complex viscosity curves of all the samples can be explained in terms of the loss tangent increasing with frequency even though the storage modulus G' increased along the way albeit at a slower rate (this can be more clearly seen by examining the 4% RGO curves). As the frequency is increased, the heat dissipated within the matrix is transferred out through the cooling effect of the rheometer Peltier plate in keeping the working temperature constant at 25 ºC.

Even though the experiments conducted were limited to a typical range, a series of time-temperature superposition (TTS) curves can be

obtained at different temperatures at the same oscillation rates to construct what is known as a master curve in order to extend the range of the frequency sweep curves if so required (Barnes, 2000).

4.2.5 Yield Test

Since the yield test is a flow experiment used to investigate how a fluid deforms at rest and transitions to flow (yield-to-flow) when subjected to a controlled increased in shear rate, it can be seen from Figure 4.33 that as shear rate was increased the shear stresses also increased immediately from the point of origin in a linear pattern for the neat epoxy and 1% RGO filled samples. Together with their almost flat viscosity curves it is clear that these two specimens do not exhibit significant yield-to-flow characteristics. Inspection of the other shear stress curves show that yield-to-flow behaviour began to emerge only at the 2% RGO concentration onwards with the 4% RGO filled sample showing the highest yield stress of 580 Pa.

The concentration of the filler affects the micro-mechanical structural property of the samples and plays a large role in the yield-to-flow behaviour of the matrix. The 2% filler level appears to be the threshold upon which the resistance offered by the higher particle concentration required a yield stress to be built up first before structural breakdown allowed the matrix to flow. This general behaviour of the RGO filled composite matrix correlates well with that shown in Figure 2.20 of the literature review.

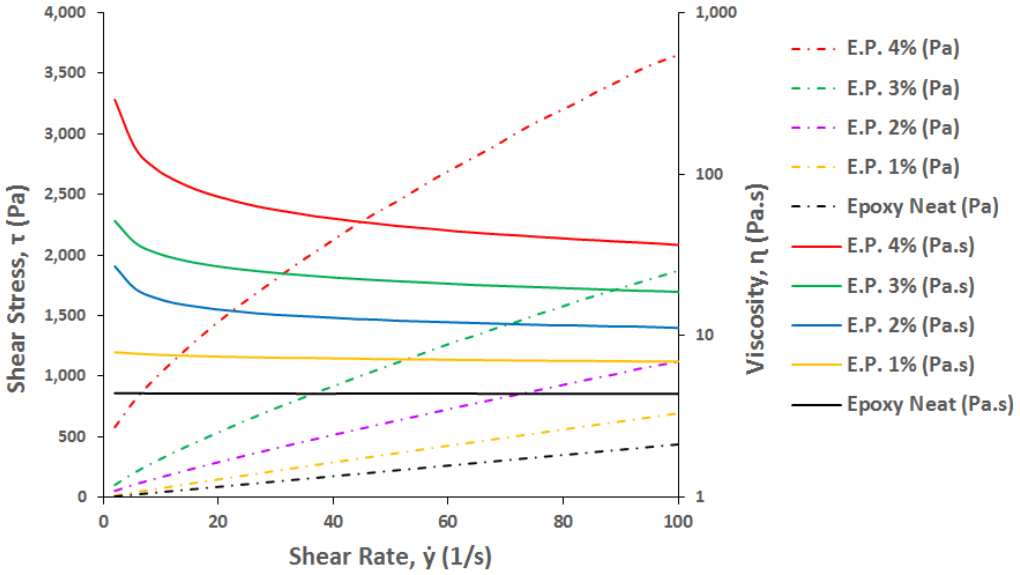

Figure 4.27: Yield test curves

4.2.6 Summary of Rheological Characterization

Neat DGEBA epoxy resin is a robust Newtonian-like fluid which did not undergo permanent changes in its polymeric micro-structure even at shear rates of up to 600 s^{-1}. With these characteristics, it is well suited as a composite binder material for ECAs.

RGO filled epoxy matrix is a thixotropic and viscoelastic composite. The behaviour of the matrix transformed gradually as filler concentration was increased. But at the 4% concentration level, it exhibited a large shift in rheological behaviour and transformed into a tacky thixotropic viscoelastic material. This highly structured gel like behaviour as seen in the predominantly linear and upward sloping G' modulus in the frequency sweep

test points to a stable formulation that would not result in particulate sedimentation over time.

4.3 Bulk Resistivity Measurements

From the curve of the bulk resistivity measurements shown in Figure 4.34, RGO filled DGEBA epoxy matrix has a percolation threshold of Pc = 0.7%. Extrapolation of the curve shows that the bulk resistivity should plateau out at around 1.00E+01 Ω cm. These characteristics are similar to the findings of Stankovich and Dikin el al (2007) as shown in Figure 2.28. Sample calculations for bulk resistivity and the measured corresponding resistance values are shown in Appendix A.

As shown in the results obtained by Park and An (2011) in figure 4.12, the purity of RGO defined by the C-O/C-C ratio can go as low as near zero. If the purity of the synthesized RGO at a C-O/C-C ratio of 0.16 is lowered, a concomitant improvement in the electrical conductivity of the 'cleaner' RGO loaded ICA can be surmised. However, due to a lack of data points in this research effort, only a further study can quantify the relationship of C-O impurity with respect to the bulk resistivity of RGO filled ICA.

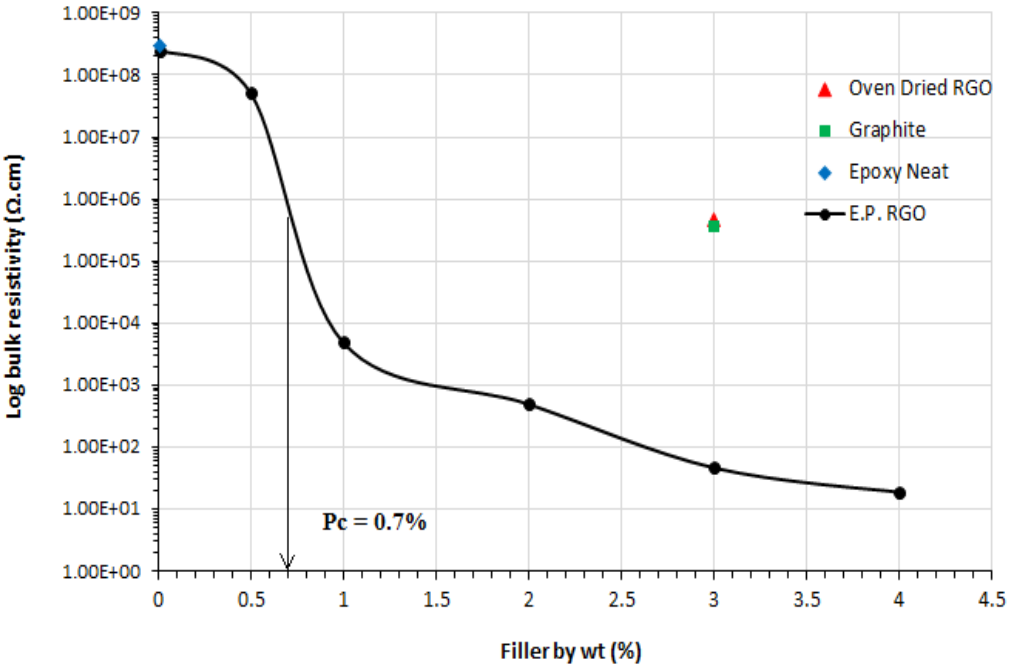

Figure 4.28: Bulk resistivity (ρ) measurements

For benchmarking purposes, both the 3% filled graphite and oven dried RGO samples were found to be less conductive by three orders of magnitude compared to the same amount of ethanol pressed RGO. As discussed in the literature review chapter, evenly dispersed small particles of RGO particles are the major factors in influencing the conductivity of ICAs. A picture of the fractured surface of a 1% ethanol pressed RGO cured sample examined under an optical microscope is shown in Figure 4.29 displaying a somewhat even level of particle dispersion but with a wide distribution of particle sizes in the range of a few microns to tens of microns in dimension.

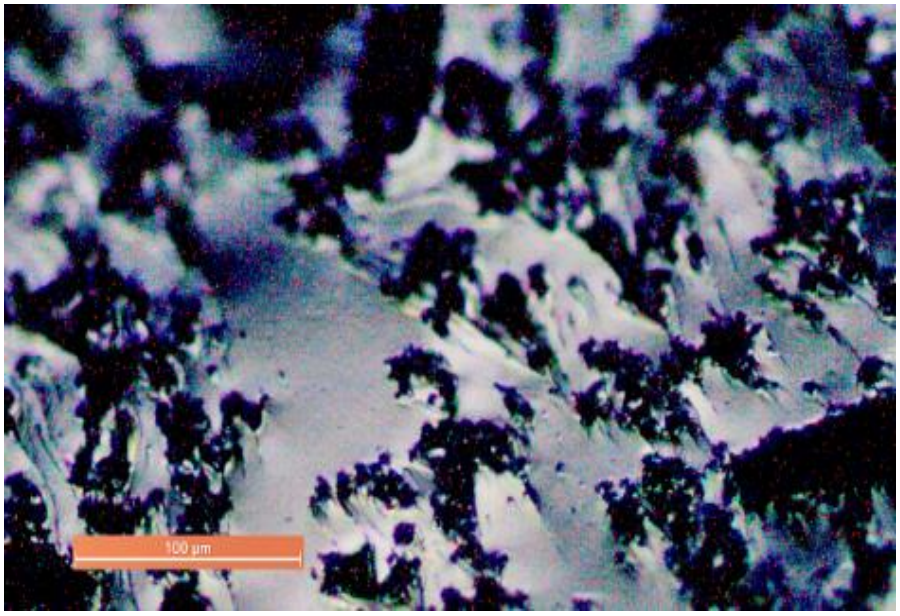

Figure 4.29: Optical micrograph of the fractured surface of a cured sample matrix filled with 1% ethanol pressed RGO. Particles are black and the light coloured background is the surface of the epoxy binder

Figure 4.30 is the FESEM images of the same sample. Even though the contrast of the RGO filler and epoxy binder is poorer compared to the optical image, the image produced from a 90º viewing angle and at a higher resolution gives a clearer understanding of how the RGO particles are dispersed and the morphology of the microstructural network in forming the conductive pathways of the ICA. At higher filler loadings, the images obtained were not informative because the higher density of particles obscured the background and therefore did not show up as distinct entities.

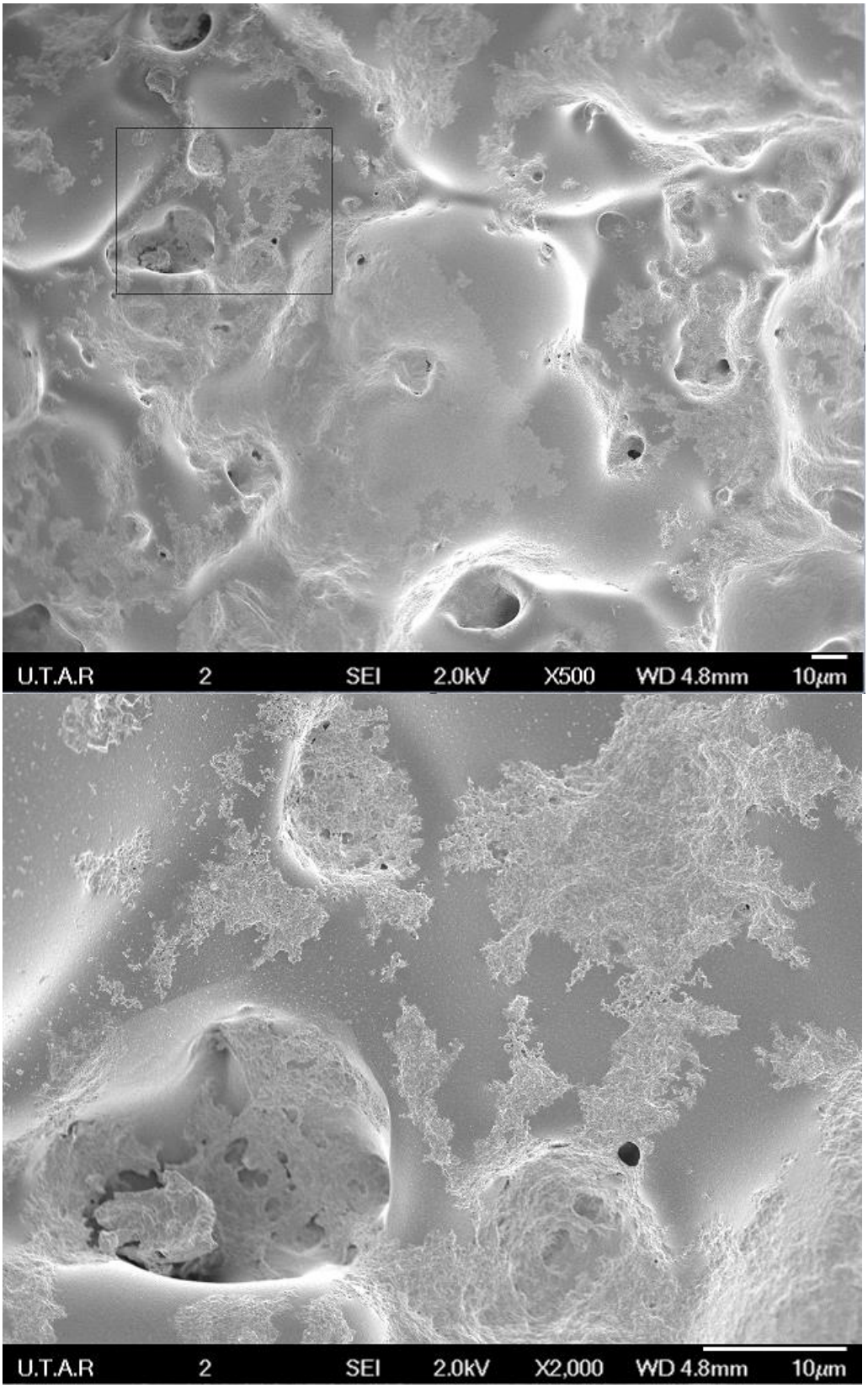

Figure 4.30: FESEM micrographs of the fractured surface of a cured sample matrix filled with 1% ethanol pressed RGO (top), and at higher magnification (bottom)

It can be clearly seen that the islands of agglomerated particles are separated by gaps with bridging points occurring randomly. Since the 1% filler concentration is above the percolation threshold of 0.7%, the number of bridging points must be sufficient enough in forming a closed circuit network across the bulk of the sample. Voids present in the samples are probably caused by the outgassing of unreacted curing agent during the curing process and may have a detrimental reliability impact in terms of mechanical moduli reduction and moisture absorption into the matrix. Possible solutions for reducing the number voids is to mix an amount of curing agent at slightly below stoichiometric ratio or by subjecting the mixture to horn ultrasonication.

In summary, two primary groups of factors affect the bulk resistivity of the RGO filled ICA – purity/lattice structure of the synthesized RGO and the size/dispersion of the RGO particles in the binder material. Further studies have to be conducted to develop a deeper understanding on how these factors affect bulk resistivity and to quantify their interactions (if any) in lowering the bulk resistivity of RGO filled ICAs.

CHAPTER 5

CONCLUSION AND RECOMMENDATION

5.1 Graphene Synthesis

The synthesis of graphene via the Huang and Lim et al. (2011) aqueous process of oxidizing natural graphite flakes into GO followed by chemical reducing using the Stankovich and Dikin et al. (2007) technique to RGO is a viable technique for producing graphene. Due to the hydrophobic nature of graphene the synthesized RGO took on the morphology of agglomerated particles consisting stacked graphene sheets when samples were examined with the FESEM. When viewed under the HRTEM at X255k magnification, one of the folded regions of an exfoliated RGO particle revealed a 5-layered sheet thickness measured at ~ 0.335 nm inter-sheet gaps.

Further HRTEM micrograph analyses provided clear visual evidence which revealed significant in-plane and edge topographical defects while the presence of distinct Raman peaks at the band shifts of D ~ 1,351.5 cm^{-1}, G ~ 1,584.8 cm^{-1}**,** 2D (or G') ~ 2,704.6 cm^{-1}, D + G ~ 2,945.1 cm^{-1} and their peak intensity ratios of I_D/I_G = 1.08 and I_{2D} / I_G = 0.19 support the conclusion that the synthesized RGO is indeed graphene. Together with the deconvoluted XPS C1s spectrum showing a highly significant C-N peak at 285.8 eV, it can be concluded that the synthesized RGO is topographically imperfect graphene

containing heteroatomic contaminations mainly as doped nitrogen atoms at a C-O/C-C purity ratio of 0.16.

5.2 Rheology Studies of RGO Dispersion in DGEBA

Flow and oscillatory rheological tests showed that RGO filled epoxy composite is predominantly Newtonian like in behaviour at a weight concentration of 1% gradually transitioning to non-Newtonian behaviour with shear thinning and thixotropic characteristics as filler content increased to 3% loading. At the 4% weight concentration level, a step change in characteristic occurred when the matrix displayed a more structured gel like behaviour.

It can be concluded that semi-wet RGO particles can be evenly dispersed in DGEBA epoxy forming a highly robust and stable liquid matrix which is a desirable characteristic in the electronics industry where syringe dispensing and screen printing processes are used. In reference to the findings published by Santamaria and Munoz et al. (2013), Lu and Tong et al. (1999), Dreyer and Ruoff et al. (2010) and Morris (2007) this new observation of semi-wet RGO filled matrix behaviour in ICA research has useful implications extending beyond the field of electronics packaging and interconnects to other areas such as lubrication technologies and paint and coating applications.

5.3 ICA Electrical Percolation Threshold

Bulk resistivity measurements showed that DGEBA epoxy filled with synthesized RGO displayed a percolation threshold of Pc = 0.7% loading by weight at a bulk resistivity of 1.50E+05 Ω cm. The conductivity behaviour of epoxy loaded with RGO from 1% to 4% by weight is consistent with that of an ICA. However, with the minimum bulk resistivity extrapolated at not lower than 1.00E+01 Ω cm this value is still six orders in magnitude higher than that of Sn/Pb solder at 1.50E-05 Ω cm. Based on this finding, the synthesized RGO filled epoxy matrix is not conductive enough to be used as a replacement for Sn/Pb type solder.

Optical and FESEM images of fractured samples managed to reveal the morphology of RGO filler material trapped within the epoxy binder material. Conductive pathways are formed through a network of dispersed RGO particles making physical contact with each other. This point to the relatively large size of agglomerated particles and the poor quality of the synthesized RGO as the limiting factors in attaining better electrical conductivity.

5.4 Recommendations

GO is hydrophilic and therefore disperses well in water. RGO on the other hand is hydrophobic and the particles begin to aggregate and agglomerate immediately upon reduction due to their high surface energies. In theory, the

conductivity of RGO filled ICA should increase if the filler particles can be stabilized at the dimension of just a few layers or even down to single sheets. Since it is possible in theory to keep the nano-dimensioned RGO sheets apart through the use of dispersing agents, particle dispersion experiments via the application of stearic and non-stearic surfactants might be useful.

The application of graphene nano-coatings via the in situ reduction of GO coatings is another area of research worth pursuing. Since GO is water soluble, a thin coating can readily be applied on specimen surfaces and subsequently reduced to an RGO layer by exposing the coated material to hydrazine vapour.

Given that the ACS Material graphene powder purchased from the United States that was used in initial experiments turned out to be not conductive and from SEM analysis appeared very likely to be exfoliated and partially reduced GO, the lesson learnt here is not to accept at face value the manufacturer's certification and to always verify the quality of commercially available graphene before use. From an equipment perspective, the addition of a horn ultrasonicator and a zeta potential analyser would be useful enhancements for our laboratory in conducting future nano-materials experiments.

REFERENCES

Areshkin, D.A., Gunlycke, D. and White, C.T., 2007. Ballistic transport in graphene nanostrips in the presence of disorder: Importance of edge effects. *Nano Letters*, 7(1), pp.204-210.

Bae, S., Kim, H., Lee, Y., Xu, X., Park, J.S., Zheng, Y., Balakrishnan, J., Lei, T., Kim, H.R., Song, Y.I. and Kim, Y.J., 2010. Roll-to-roll production of 30-inch graphene films for transparent electrodes. *Nature nanotechnology*, 5(8), pp.574-578.

Bagri, A., Mattevi, C., Acik, M., Chabal, Y.J., Chhowalla, M. and Shenoy, V.B., 2010. Structural evolution during the reduction of chemically derived graphene oxide. *Nature chemistry*, 2(7), pp.581-587.

Barnes, H.A., 1997. Thixotropy—a review. *Journal of Non-Newtonian fluid mechanics*, 70(1), pp.1-33.

Barnes, H.A., 1999. The yield stress—a review or ‘παντα ρει’—everything flows?. *Journal of Non-Newtonian Fluid Mechanics*, 81(1), pp.133-178.

Barnes, H.A., 2000. *A handbook of elementary rheology*. Institute of non-Newtonian Fluid Mechanics, University of Wales. Aberystwyth.

Barnes, H.A., Hutton, J.F. and Walters, K., 1989. *An introduction to rheology* (Vol. 3). Elsevier.

Bellinger, D.C. and Bellinger, A.M., 2006. Childhood lead poisoning: the torturous path from science to policy. *Journal of Clinical Investigation*, 116(4), p.853.

Biró, L. P., P. Nemes-Incze, et al., 2012. Graphene: nanoscale processing and recent applications. *Nanoscale*, 4(6), pp.1824-1839.

Bonaccorso, F., Lombardo, A., Hasan, T., Sun, Z., Colombo, L. and Ferrari, A.C., 2012. Production and processing of graphene and 2d crystals. *Materials Today*, 15(12), pp.564-589.

Brodie, B.C., 1859. On the atomic weight of graphite. *Philosophical Transactions of the Royal Society of London*, pp.249-259.

Chastain, J. and King, R.C. eds., 1992. *Handbook of X-ray photoelectron spectroscopy: a reference book of standard spectra for identification and interpretation of XPS data* (p. 261). Eden Prairie, MN: Perkin-Elmer.

Childres, I., Jauregui, L.A., Park, W., Cao, H. and Chen, Y.P., 2013. Raman spectroscopy of graphene and related materials. *New developments in photon and materials research*, *1*, pp.978-981.

Creative Commons, 2015. *A piece of resistive material with electrical contacts on both ends*. [Online] Wikipedia. Available at: <https://commons.wikimedia.org/wiki/File:Resistivity_geometry.png> [Accessed 19 November 2015]

Cullity, B.D., 1956. *Elements of X-ray Diffraction*. Adisson-Wesley Publishing. USA.

Dow Answer Center, 2015. *Dow-epoxy-calculation-of-stoichiometric-ratios*. [Online] Midland: Dow Corning Corporation. Available at: <http://dowac.custhelp.com/app/answers/detail/a_id/4151/~/dow-epoxy---calculation-of-stoichiometric-ratios> [Accessed 2 December 2015].

Dow Corning, 2015. *IMAGINE: Reliable adhesion in extreme conditions*. [Online] Midland: Dow Corning Corporation. Available at: <https://www.dowcorning.com/content/electronics/electronicsproducts/sapm-die-attach-adhesives.aspx> [Accessed 10 December 2015].

Dreyer, D.R., Park, S., Bielawski, C.W. and Ruoff, R.S., 2010. The chemistry of graphene oxide. *Chemical Society Reviews*, 39(1), pp.228-240.

Dreyer, D.R., Ruoff, R.S. and Bielawski, C.W., 2010. From conception to realization: an historial account of graphene and some perspectives for its future. *Angewandte Chemie International Edition*, 49(49), pp.9336-9344.

Du, J. and Cheng, H.M., 2012. The fabrication, properties, and uses of graphene/polymer composites. *Macromolecular Chemistry and Physics*, 213(10-11), pp.1060-1077.

Duffy, J.J., Hill, A., Walton, A. and Mazzeo, F., 2011. Suspension stability; Why particle size, zeta potential and rheology are important. *Proceedings of Particulate Systems Analysis*.

Environment Directorate General of the European Commission, 2009. *Waste Electrical and Electronic Equipment (WEEE)*. [Online] Brussels: European Commission. Available at: <http://ec. europa. eu/environment/waste/weee/index_en. htm> [Accessed 10 December 2015].

EPOTEK, 2015. *EPO-TEK E3001 Technical Data Sheet*. [Online] Pembroke Pines:, Epoxy Technology, Inc. Available at: < http://www.epotek.com/site/administrator/components/com_products/assets/files/Style_Uploads/E3001.pdf> [Accessed 10 December 2015].

Ferrari, A.C., 2007. Raman spectroscopy of graphene and graphite: disorder, electron–phonon coupling, doping and nonadiabatic effects. *Solid state communications*, 143(1), pp.47-57.

Ferrari, A.C. and Basko, D.M., 2013. Raman spectroscopy as a versatile tool for studying the properties of graphene. *Nature nanotechnology*, 8(4), pp.235-246.

Ferrari, A.C., Bonaccorso, F., Fal'Ko, V., Novoselov, K.S., Roche, S., Bøggild, P., Borini, S., Koppens, F.H., Palermo, V., Pugno, N. and Garrido, J.A., 2015. Science and technology roadmap for graphene, related two-dimensional crystals, and hybrid systems. *Nanoscale*, 7(11), pp.4598-4810.

Franck, A.J., 2004. Understanding rheology of structured fluids. *Book of TA instruments*, pp.1-17.

Gao, Y., Ma, D., Wang, C., Guan, J. and Bao, X., 2011. Reduced graphene oxide as a catalyst for hydrogenation of nitrobenzene at room temperature. *Chem. Commun.*, 47(8), pp.2432-2434.

Garg, B., Bisht, T. and Ling, Y.C., 2014. Graphene-based nanomaterials as heterogeneous acid catalysts: a comprehensive perspective. *Molecules*, 19(9), pp.14582-14614.

Geim, A. K. and Novoselov, K. S., 2007. The rise of graphene. *Nature materials*, 6(3), pp.183-191.

Gillespie, R.J., 2004. Teaching molecular geometry with the VSEPR model. *Journal of Chemical Education*, 81(3), pp.298–304.

Handwerker, C., 2005. Transitioning to Pb-free assemblies. *INEMI Report*. [pdf] Frankfurt: NIST. Available at: <http://thor.inemi.org/webdownload/projects/ese/IPC_JEDEC-Handwerker.pdf> [Accessed 10 December 2015].

He, L. and Tjong, S.C., 2013. Low percolation threshold of graphene/polymer composites prepared by solvothermal reduction of graphene oxide in the polymer solution. *Nanoscale research letters*, 8(1), pp.1-7.

Huang, N.M., Lim, H.N., Chia, C.H., Yarmo, M.A. and Muhamad, M.R., 2011. Simple room-temperature preparation of high-yield large-area graphene oxide. *International journal of nanomedicine*, 6(6), pp.3443-3448.

Hummers Jr, W.S. and Offeman, R.E., 1958. Preparation of graphitic oxide. *Journal of the American Chemical Society*, 80(6), pp.1339-1339.

Jorio, A., 2012. Raman spectroscopy in graphene-based systems: Prototypes for nanoscience and nanometrology. *ISRN Nanotechnology*, 2012.

Kang, S. K., 1999. Development of lead (Pb)-free interconnection materials for microelectronics. *Metals and Materials*, 5(6), pp.545-549.

Kobayashi, T., Bando, M., Kimura, N., Shimizu, K., Kadono, K., Umezu, N., Miyahara, K., Hayazaki, S., Nagai, S., Mizuguchi, Y. and Murakami, Y., 2013. Production of a 100-m-long high-quality graphene transparent conductive film by roll-to-roll chemical vapor deposition and transfer process. *Applied Physics Letters*, 102(2), p.023112.

Kotakoski, J., Krasheninnikov, A.V., Kaiser, U. and Meyer, J.C., 2011. From point defects in graphene to two-dimensional amorphous carbon. *Physical Review Letters*, 106(10), p.105505.

Lafuente, B., Downs, R.T., Yang, H. and Stone, N., 2015. The power of databases: the RRUFF project. *Highlights in Mineralogical Crystallography, ed. T. Armbruster and RM Danisi, W. De Gruyter, Berlin, Germany*, pp.1-30.

Lee, N.C., 1997. Getting Ready for Lead-free Solders*. *Soldering & Surface Mount Technology*, 9(2), pp.65-69.

Lerf, A., Buchsteiner, A., Pieper, J., Schöttl, S., Dekany, I., Szabo, T. and Boehm, H.P., 2006. Hydration behavior and dynamics of water molecules in graphite oxide. *Journal of Physics and Chemistry of Solids*, 67(5), pp.1106-1110.

Lerf, A., He, H., Forster, M. and Klinowski, J., 1998. Structure of graphite oxide revisited. *The Journal of Physical Chemistry B*, 102(23), pp.4477-4482.

Li, Y. and Wong, C.P., 2006. Recent advances of conductive adhesives as a lead-free alternative in electronic packaging: materials, processing, reliability and applications. *Materials Science and Engineering: R: Reports*, 51(1), pp.1-35.

Li, Y.G., Lu, D. and Wong, C.P., 2009. *Electrical conductive adhesives with nanotechnologies*. Springer Science & Business Media.

Lu, D. and Wong, C.P., 2000. Development of conductive adhesives for solder replacement. *Components and Packaging Technologies, IEEE Transactions on*, 23(4), pp.620-626.

Marcano, D.C., Kosynkin, D.V., Berlin, J.M., Sinitskii, A., Sun, Z., Slesarev, A., Alemany, L.B., Lu, W. and Tour, J.M., 2010. Improved synthesis of graphene oxide. *ACS nano*, 4(8), pp.4806-4814.

Matula, R.A., 1979. Electrical resistivity of copper, gold, palladium, and silver. *Journal of Physical and Chemical Reference Data*, 8(4), pp.1147-1298.

Meyer, J.C., Geim, A.K., Katsnelson, M.I., Novoselov, K.S., Booth, T.J. and Roth, S., 2007. The structure of suspended graphene sheets. *Nature*, 446(7131), pp.60-63.

Mezger, T.G., 2006. *The rheology handbook: for users of rotational and oscillatory rheometers*. Vincentz Network GmbH & Co KG.

Miller, C.M., Anderson, I.E. and Smith, J.F., 1994. A viable tin-lead solder substitute: Sn-Ag-Cu. *Journal of Electronic Materials*, 23(7), pp.595-601.

Mir, I. and Kumar, D., 2008. Recent advances in isotropic conductive adhesives for electronics packaging applications. *International journal of adhesion and adhesives*, 28(7), pp.362-371.

Morris, J.E., 2007. Isotropic conductive adhesives: Future trends, possibilities and risks. *Microelectronics Reliability*, 47(2), pp.328-330.

Mukhopadhyay, P. and Gupta, R.K. eds., 2012. *Graphite, Graphene, and their polymer nanocomposites*. CRC Press.

Nakajima, T. and Matsuo, Y., 1994. Formation process and structure of graphite oxide. *Carbon*, 32(3), pp.469-475.

Nanofutures, 2015. *European initiative for sustainable development by Nanotechnologies*. [Online] Brussels: European Commission. Available at: < http://www.nanofutures.eu/about> [Accessed 19 October 2015]

NNI, 2015. *What is Nanotechnology?* [Online] U.S.A.: National Nanotechnology Initiative. Available at: < http://www.nano.gov/nanotech-101/what/definition> [Accessed 19 October 2015]

Novoselov, K.S., Geim, A.K., Morozov, S.V., Jiang, D., Zhang, Y., Dubonos, S.A., Grigorieva, I.V. and Firsov, A.A., 2004. Electric field effect in atomically thin carbon films. *science*, 306(5696), pp.666-669.

NSTC/CoT/NSET, 2014. *NNI Supplement to the President's 2015 Budget*. [Online] U.S.A.: National Nanotechnology Initiative. Available at: <http://www.nano.gov/node/1128> [Accessed 19 October 2015]

Park, S., An, J., Potts, J.R., Velamakanni, A., Murali, S. and Ruoff, R.S., 2011. Hydrazine-reduction of graphite-and graphene oxide. *Carbon*, 49(9), pp.3019-3023.

Pauling, L., 1931. The nature of the chemical bond. Application of results obtained from the quantum mechanics and from a theory of paramagnetic susceptibility to the structure of molecules. *Journal of the American Chemical Society*, 53(4), pp.1367-1400.

PIRE-ECCHI, 2015. *Introduction to X-ray Photoelectron Spectroscopy (XPS)*. [Online] Santa Barbara: University of California Santa Barbara. Available at: <http://pire-ecci.ucsb.edu/pire-ecci-old/summerschool/papers/vohs1.pdf> [Accessed 10 December 2015].

Quora, 2015. *In chemistry, what are carbon double bonds and triple bonds?* [Online] California: Quora Inc. Available at: <https://www.quora.com/In-chemistry-what-are-carbon-double-bonds-and-triple-bonds> [Accessed 24 November 2015].

Rajagopalan, B. and Chung, J.S., 2014. Reduced chemically modified graphene oxide for supercapacitor electrode. *Nanoscale research letters*, 9(1), pp.1-10.

Roduner, E., 2006. Size matters: why nanomaterials are different. *Chemical Society Reviews*, 35(7), pp.583-592.

RoHSGuide, 2015. *RoHS Compliance Guide: Regulations, 6 Substances, Exemptions, WEEE*. [ONLINE] Brussels: European Commission. Available at: <http://www.rohsguide.com> [Accessed 10 December 2015].

RRUFF, 2015a. *Graphite*. [ONLINE] Tuscon: RRUFF Project. Available at: <http://rruff.info/repository/sample_child_record_powder/by_minerals/Graphite__R050503-1__Powder__DIF_File__6230.txt> [Accessed 11 December 2015].

RRUFF, 2015b. *Aluminium*. [ONLINE] Tuscon: RRUFF Project. Available at: <http://rruff.geo.arizona.edu/AMS/xtal_data/DIFfiles/12907.txt> [Accessed 11 December 2015].

Santamaria, A., Muñoz, M.E., Fernández, M. and Landa, M., 2013. Electrically conductive adhesives with a focus on adhesives that contain carbon nanotubes. *Journal of Applied Polymer Science*, 129(4), pp.1643-1652.

Sigma-Aldrich, 2015. *D3415 Sigma Bisphenol A diglycidyl ether*. [Online] St. Louis: Sigma-Aldrich Corporation. Available at: <http://www.sigmaaldrich.com/catalog/product/sigma/d3415?lang=en&region=MY> [Accessed: 2 December 2015].

Skeist, I. ed., 2012. *Handbook of adhesives*. Springer Science & Business Media.

Smith, E. and Dent, G., 2013. *Modern Raman spectroscopy: a practical approach*. John Wiley & Sons.

Stankovich, S., Dikin, D.A., Dommett, G.H., Kohlhaas, K.M., Zimney, E.J., Stach, E.A., Piner, R.D., Nguyen, S.T. and Ruoff, R.S., 2006. Graphene-based composite materials. *Nature*, 442(7100), pp.282-286.

Stankovich, S., Dikin, D.A., Piner, R.D., Kohlhaas, K.A., Kleinhammes, A., Jia, Y., Wu, Y., Nguyen, S.T. and Ruoff, R.S., 2007. Synthesis of graphene-based nanosheets via chemical reduction of exfoliated graphite oxide. *Carbon*, 45(7), pp.1558-1565.

Staudenmaier, L., 1898. Verfahren zur darstellung der graphitsäure. *Berichte der deutschen chemischen Gesellschaft*, 31(2), pp.1481-1487.

Suganuma, K., 2002. The current status of lead-free soldering. *ESPEC technology report*, 13, pp.1-8.

Suhir, E., Lee, Y.C. and Wong, C.P. eds., 2007. *Micro-and Opto-Electronic Materials and Structures: Physics, Mechanics, Design, Reliability, Packaging: Volume I Materials Physics-Materials Mechanics. Volume II Physical Design-Reliability and Packaging* (Vol. 1). Springer Science & Business Media.

Tan, C.H., 2015. *Thermal Interface Material*. BEng. Universiti Tunku Abdul Rahman.

Thomas, D.N., Judd, S.J. and Fawcett, N., 1999. Flocculation modelling: a review. *Water research*, 33(7), pp.1579-1592.

UCLA, 2001. *Infrared Spectroscopy Table*. [Online] Los Angeles: University of California Los Angeles. Available at: <http://www.chem.ucla.edu/~bacher/General/30BL/IR/ir.html> [Accessed 8 Dec 2015]

University of Colorado, 2015. *Table of Characteristic IR Absorptions*. [Online] Boulder: University of Colorado Boulder <http://orgchem.colorado.edu/Spectroscopy/specttutor/irchart.html> [Accessed 8 Dec 2015]

University of Montana, 2015. *Nanotechnology Size Comparisons.* [Online] Missoula: University of Montana. Available at: <http://www.umt.edu/ethics/debating%20science%20program/odc/imx/Nanoscale_2.jpg> [Accessed 10 December 2015]

Verdejo, R., Bernal, M.M., Romasanta, L.J. and Lopez-Manchado, M.A., 2011. Graphene filled polymer nanocomposites. *Journal of Materials Chemistry*, 21(10), pp.3301-3310.

WEITZ, D., WYSS, H. and LARSEN, R., 2007. Oscillatory rheology: Measuring the viscoelastic behaviour of soft materials. *GIT laboratory journal Europe*, 11(3-4), pp.68-70.

Willenbacher, N. and Georgieva K., 2013. *Rheology of Disperse Systems*. Wiley VCH Verlag GmbH & Co. KGaA: Weinheim, Germany, pp. 7-49.

Wong, C.P., Moon, K.S. and Li, Y., 2010. *Nano-bio-electronic, photonic and MEMS packaging*. New York: Springer.

Wu, H.P., Wu, X.J., Ge, M.Y., Zhang, G.Q., Wang, Y.W. and Jiang, J.Z., 2007a. Effect analysis of filler sizes on percolation threshold of isotropical conductive adhesives. *Composites science and technology*, 67(6), pp.1116-1120.

Wu, H.P., Wu, X.J., Ge, M.Y., Zhang, G.Q., Wang, Y.W. and Jiang, J.Z., 2007b. Properties investigation on isotropical conductive adhesives filled with silver coated carbon nanotubes. *Composites science and technology*, 67(6), pp.1182-1186.

Yim, B.S. and Kim, J.M., 2010. Characteristics of isotropically conductive adhesive (ICA) filled with carbon nanotubes (CNTs) and low-melting-point alloy fillers. *Materials transactions*, 51(12), pp.2329-2331.

Zhang, C., Dabbs, D.M., Liu, L.M., Aksay, I.A., Car, R. and Selloni, A., 2015. Combined effects of functional groups, lattice defects, and edges in the infrared spectra of graphene oxide. *The Journal of Physical Chemistry C*, 119(32), pp.18167-18176.

APPENDICES

APPENDIX A

A1: Bulk resistivity readings

			Bulk Resistivity Ohm.cm		
Filler% wt	ACS Graphene	E.P. RGO	Graphite	Freeze Dried RGO	Oven Dried RGO
0.01	2.51E+09	2.50E+09			
0.1	1.62E+09				
0.5	1.05E+09	5.08E+08			
1	1.49E+09	4.87E+04			
1.5	7.63E+08				
2	5.01E+08	4.95E+03			
2.5					
3	2.93E+08	4.68E+02	3.64E+06	1.25E+05	4.61E+06
3.5					
4	3.50E+08	1.88E+02			
4.5					
5	3.18E+08				

Sample calculation for specimen filled with 3% E.P. RGO:

$$\rho = \frac{RA}{l} \quad \ldots\ldots \text{from equation 2.1}$$

where ρ = bulk resistivity (Ω cm)

R = resistance of specimen

A = cross-sectional area of specimen

l = length of specimen

R = 1106 Ohms, A = 44.66 mm^2, l = 10.56 mm, therefore:

$$\rho = \frac{1106\ X\ 44.66}{10.56}$$

$$= \text{4.68E+3 Ω.mm}$$

$$= \text{4.68E+2 Ω.cm}$$

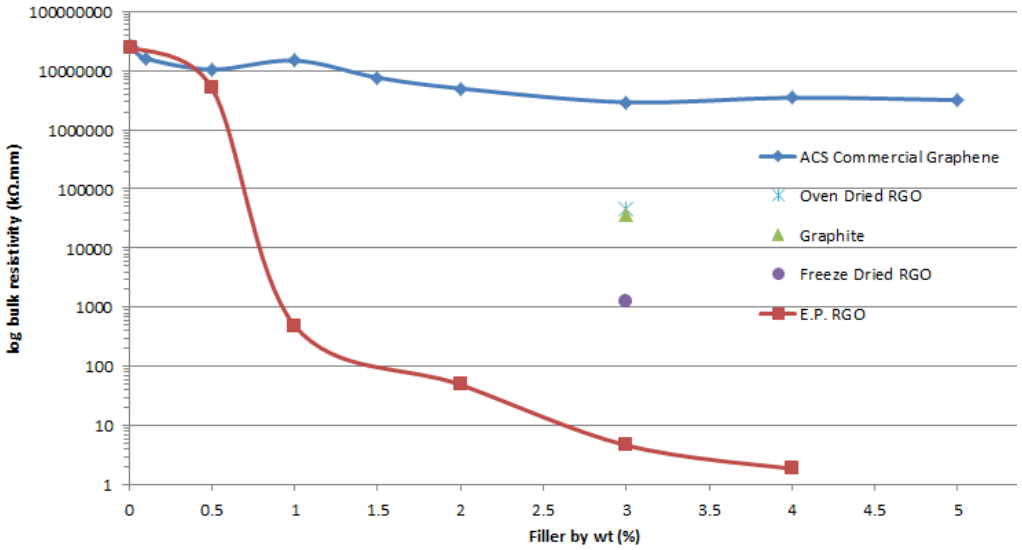

A2: Bulk resistivity graph including ACS commercial graphene

APPENDIX B

Supplementary images.

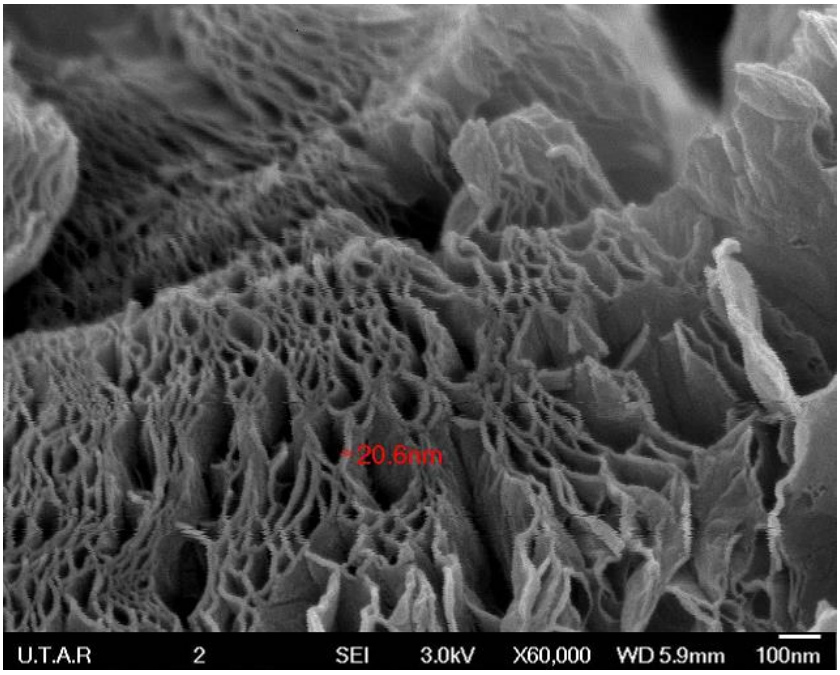

B1: ACS Commercial Graphene

B2: Freeze Dried RGO

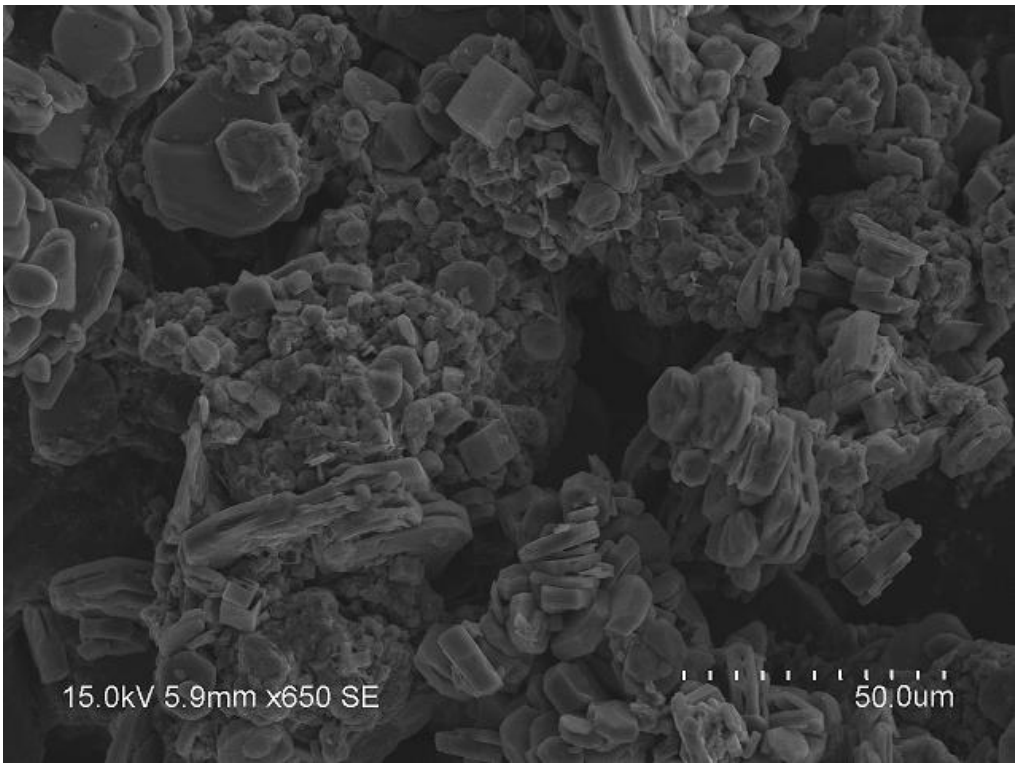

B3: Asbury Carbon Nano 25 natural graphite X650 magnification

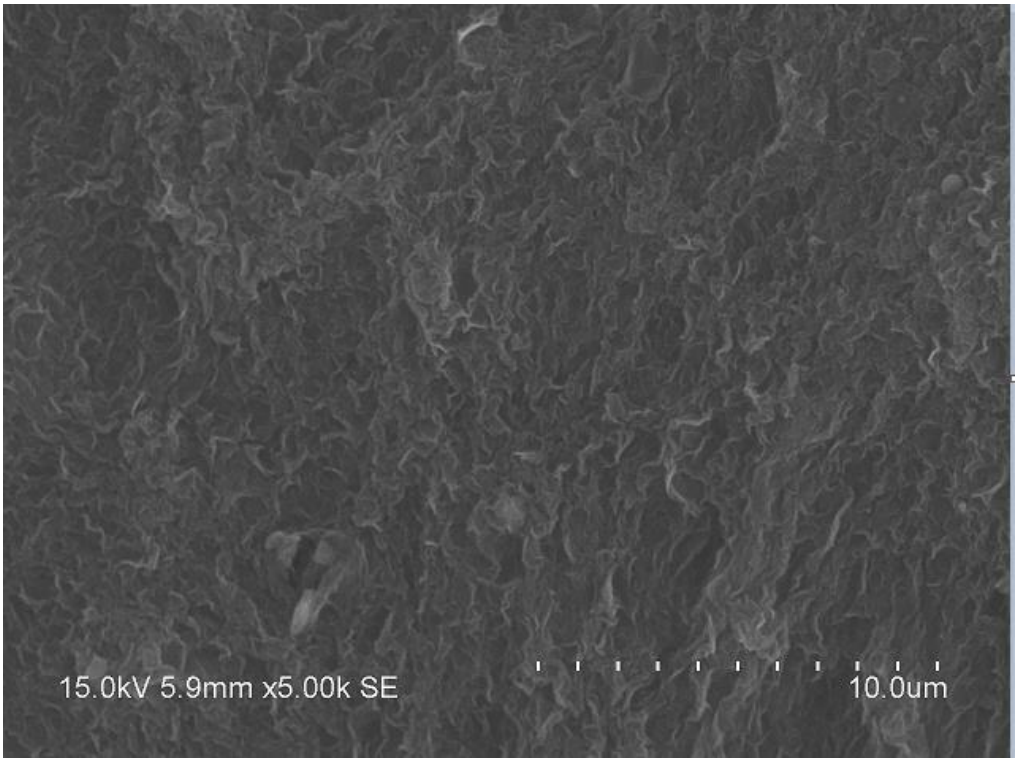

B4: Exfoliated (via ultrasonication) and dried RGO

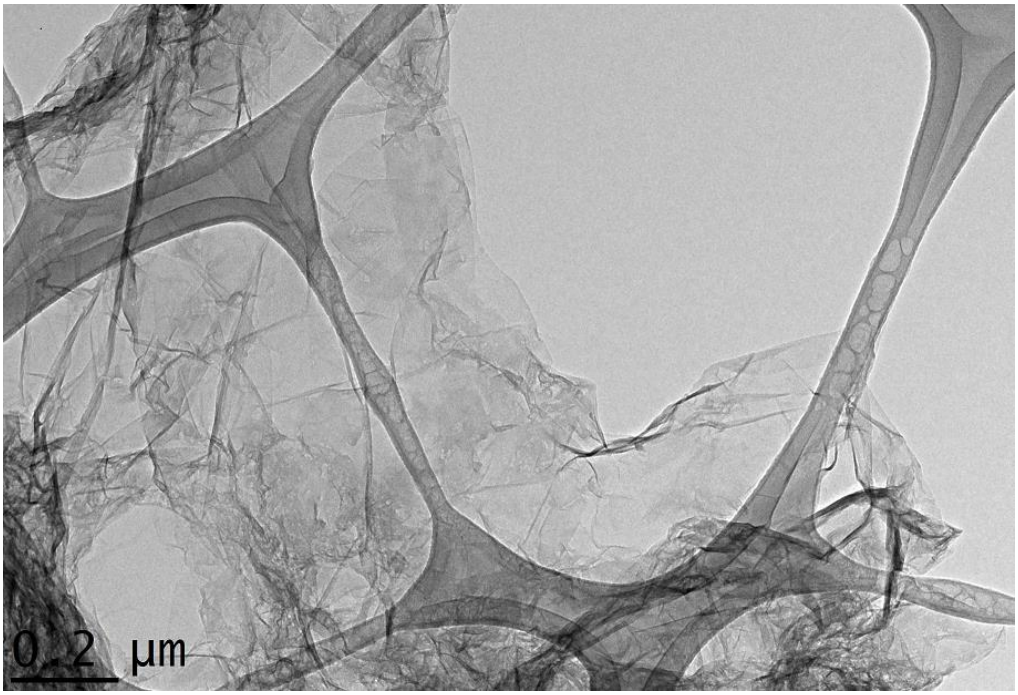

B5: HRTEM image of RGO at X13.5k magnification

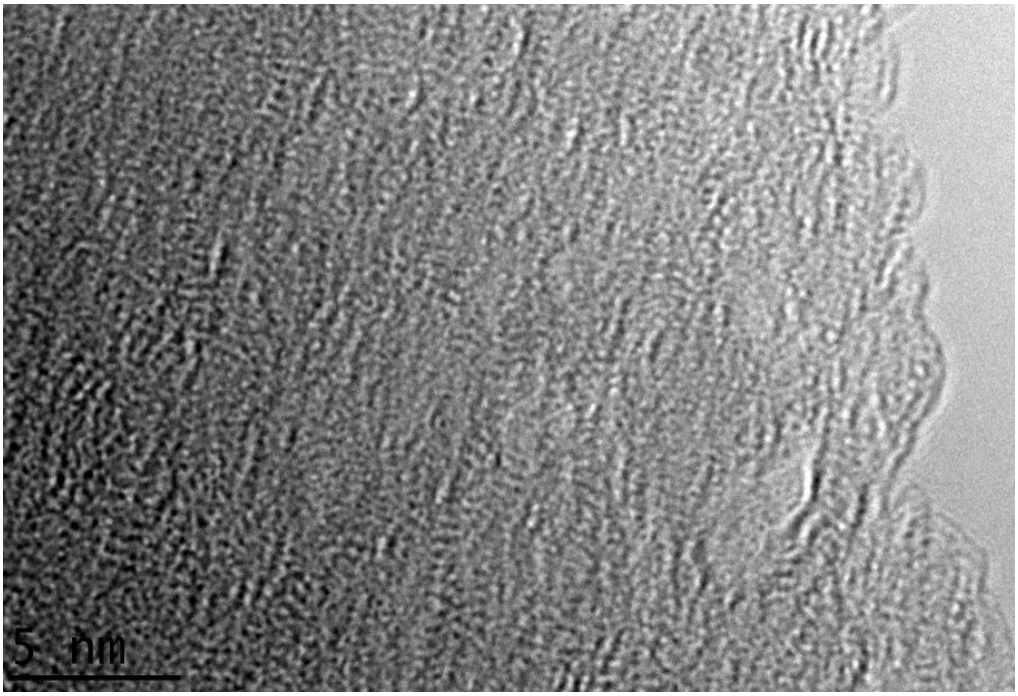

B6: HRTEM image of RGO at X800k magnification

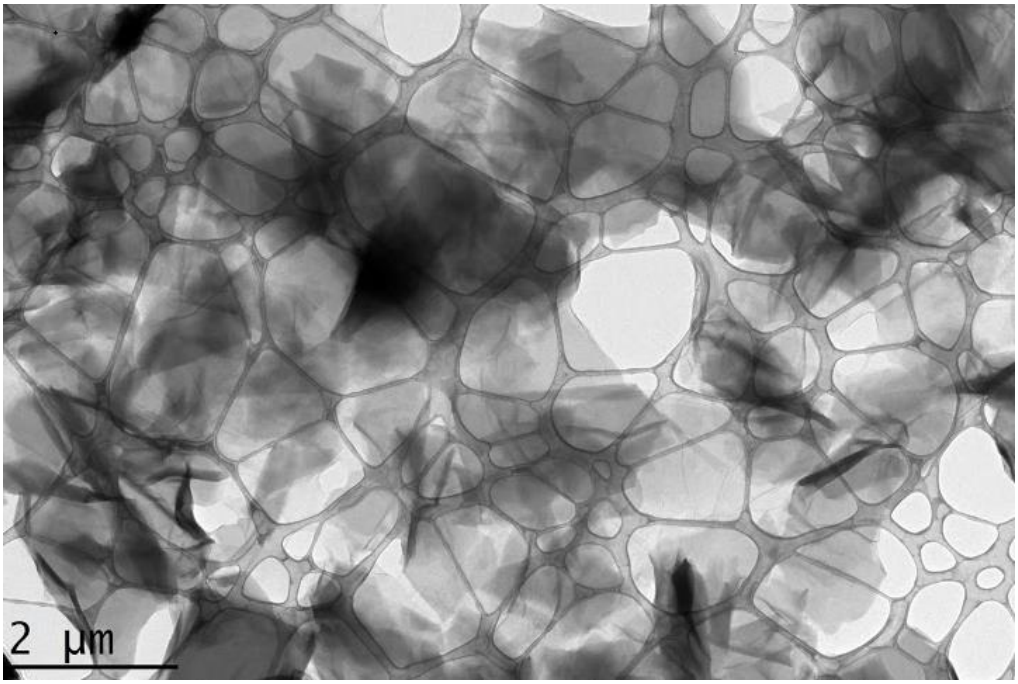

B7: HRTEM image of GO at X2.3k magnification

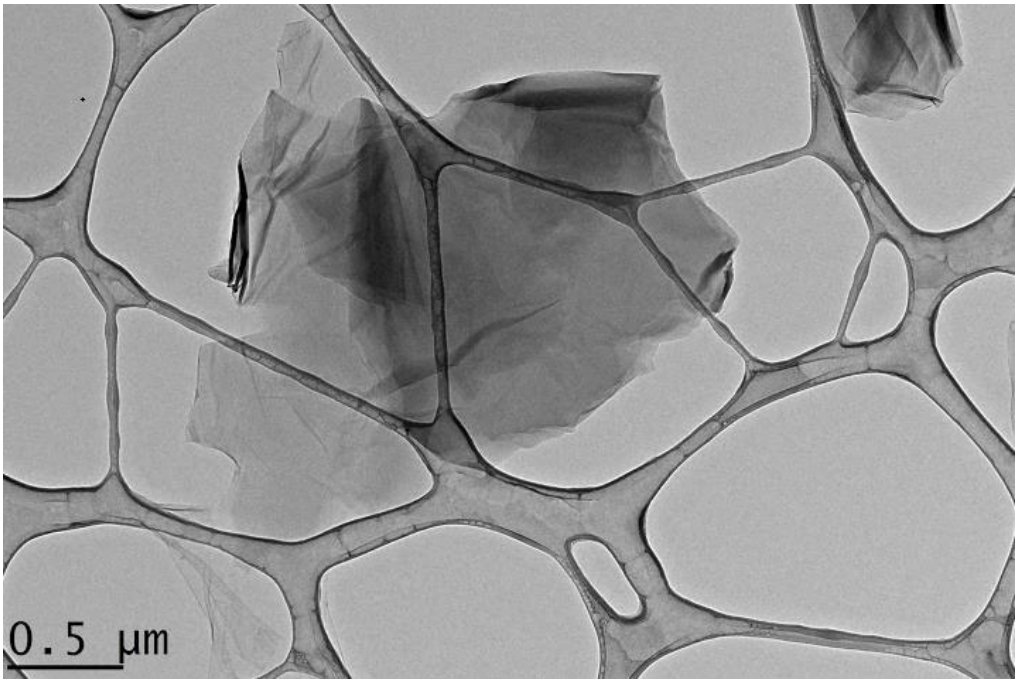

B8: HRTEM image of GO at X6.3k magnification

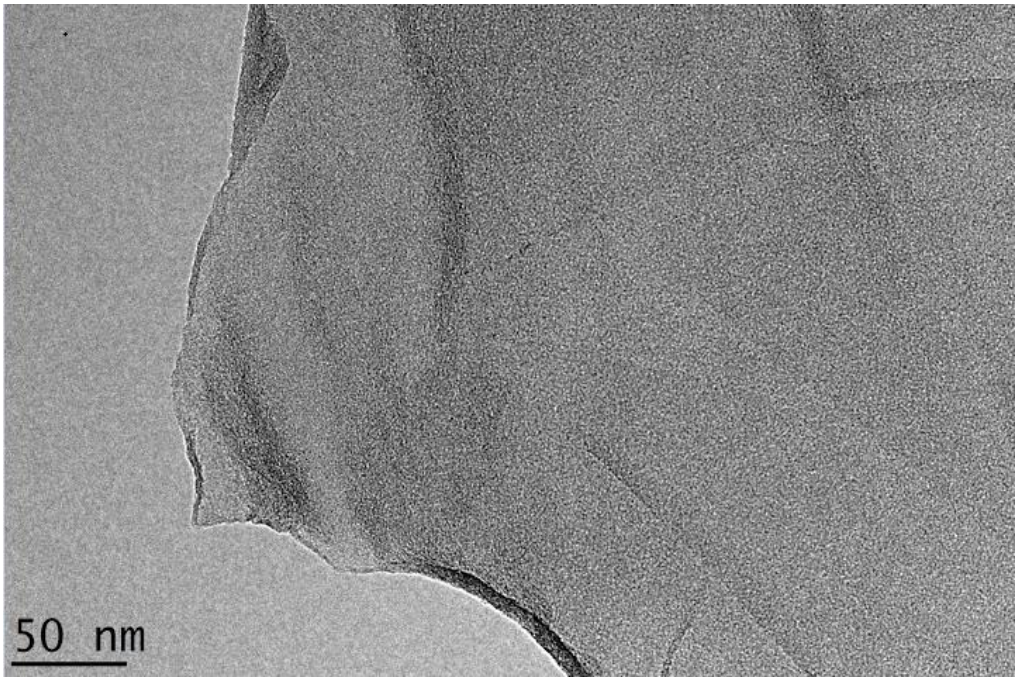

B9: HRTEM image of GO at X64k magnification

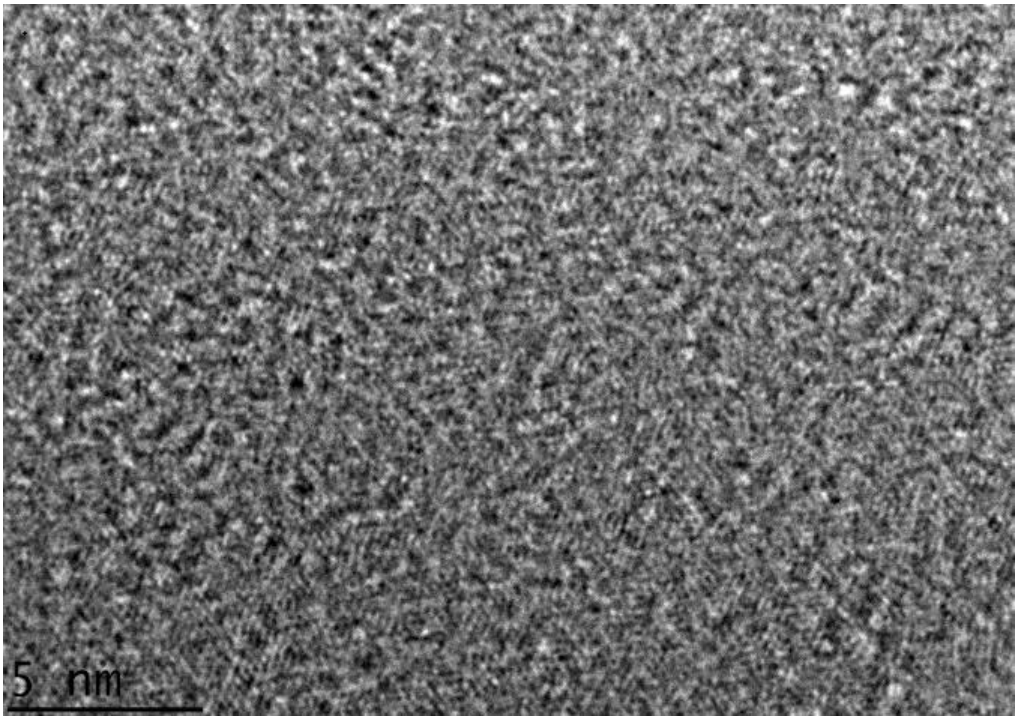

B10: HRTEM image of GO at X930k magnification

APPENDIX C

Sample rheology data.

Data Series Information			Frequency Sweep					
Name:			Ethan Press 4%					
Number of Intervals:			1					
Application:			RHEOPLUS/32 V3.21 21003688-33024					
Device:			MCR301 SN80350866; FW3.41D110330; Slot4					
Measuring Date/Time:			1/1/2007; 3:10 AM					
Measuring System:			PP25-SN13717; [d=0.5 mm]					
Accessories:			TU1=P-PTD200-SN80484899					
Calculating Constants:								
- Norm. Csr [min/s]:			1.307468					
- Norm. Css [Pa/mNm]:			327.0941					
- Start Delay Time [s]:			4.031					
- Substance Density [rho]:			1,000					
- Measurement Type:			1					
- Motor Correction Factor:			1					
Interval:			1					
Number of Data Points:			16					
Time Setting:			16 Meas. Pts.					
			Meas. Pt. Duration 1 s					
Measuring Profile:								
#NAME?			Amplitude gamma = 5 %					
			Angular Frequency omega = 100 ... 0.1 1/s log; |Slope| = 5 Pt. / de					
Meas. Pts.	Angular Fre	Storage M	Loss Modu	Damping F	Complex V	Deflection	Torque	Status
	[1/s]	[Pa]	[Pa]	[1]	[Pa·s]	[mrad]	[µNm]	[]
1	100	3.43E+03	4.85E+03	1.42	5.94E+01	1.52E+00	6.87E+02	WMa,DSO
2	63.1	2.23E+03	3.65E+03	1.64	6.78E+01	1.86E+00	6.07E+02	WMa,DSO
3	39.8	1.61E+03	2.75E+03	1.71	8.01E+01	1.84E+00	4.48E+02	WMa,DSO
4	25.1	1.43E+03	2.17E+03	1.52	1.03E+02	1.87E+00	3.70E+02	WMa,DSO
5	15.8	1.38E+03	1.75E+03	1.27	1.40E+02	1.90E+00	3.24E+02	WMa,DSO
6	10	1.36E+03	1.41E+03	1.04	1.96E+02	1.93E+00	2.90E+02	WMa,DSO
7	6.31	1.32E+03	1.16E+03	0.878	2.79E+02	1.96E+00	2.63E+02	WMa,DSO
8	3.98	1.30E+03	9.96E+02	0.766	4.11E+02	1.97E+00	2.46E+02	WMa,DSO
9	2.51	1.25E+03	9.22E+02	0.737	6.19E+02	1.98E+00	2.35E+02	WMa,DSO
10	1.58	1.20E+03	8.26E+02	0.688	9.19E+02	1.98E+00	2.20E+02	WMa,DSO
11	1	1.21E+03	8.14E+02	0.674	1.46E+03	1.98E+00	2.21E+02	WMa,DSO
12	0.631	1.22E+03	7.69E+02	0.628	2.29E+03	1.98E+00	2.19E+02	WMa,DSO
13	0.398	1.22E+03	7.21E+02	0.592	3.55E+03	1.98E+00	2.14E+02	WMa,DSO
14	0.251	1.20E+03	6.89E+02	0.574	5.51E+03	1.99E+00	2.10E+02	WMa,DSO
15	0.158	1.18E+03	6.70E+02	0.566	8.58E+03	1.99E+00	2.06E+02	WMa,DSO
16	0.1	1.17E+03	6.59E+02	0.563	1.34E+04	1.99E+00	2.04E+02	WMa,DSO

Data Series Information	Amplitude Sweep
Name:	Ethan Press 4%
Number of Intervals:	1
Application:	RHEOPLUS/32 V3.21 21003688-33024
Device:	MCR301 SN80350866; FW3.41D110330; Slot4
Measuring Date/Time:	1/1/2007; 2:57 AM
Measuring System:	PP25-SN13717; [d=0.5 mm]
Accessories:	TU1=P-PTD200-SN80484899
Calculating Constants:	
- Norm. Csr [min/s]:	1.307468
- Norm. Css [Pa/mNm]:	327.0941
- Start Delay Time [s]:	4.5
- Substance Density [rho]:	1,000
- Measurement Type:	1
- Motor Correction Factor:	1
Interval:	1
Number of Data Points:	25
Time Setting:	25 Meas. Pts.
	Meas. Pt. Duration 6 s
Measuring Profile:	
#NAME?	Amplitude gamma = 0.01 ... 100 % log; |Slope| = 6 Pt. / dec
	Angular Frequency omega = 10 1/s

Meas. Pts.	Strain	Shear Stre	Storage M	Loss Modu	Damping F	Deflection	Torque	Status
	[%]	[Pa]	[Pa]	[Pa]	[1]	[mrad]	[µNm]	[]
1	0.01	5.24E-01	4.96E+03	1.70E+03	0.341	0.004	1.6	WMa,DSO
2	0.0146	7.69E-01	5.00E+03	1.70E+03	0.34	0.00582	2.35	WMa,DSO
3	0.0213	1.14E+00	5.04E+03	1.69E+03	0.336	0.00854	3.47	WMa,DSO
4	0.0313	1.67E+00	5.07E+03	1.70E+03	0.334	0.0125	5.12	WMa,DSO
5	0.046	2.46E+00	5.08E+03	1.70E+03	0.334	0.0184	7.53	WMa,DSO
6	0.0675	3.62E+00	5.09E+03	1.69E+03	0.333	0.027	11.1	WMa,DSO
7	0.099	5.32E+00	5.10E+03	1.70E+03	0.333	0.0396	16.3	WMa,DSO
8	0.145	7.82E+00	5.11E+03	1.70E+03	0.333	0.0582	23.9	WMa,DSO
9	0.213	1.15E+01	5.10E+03	1.71E+03	0.335	0.0853	35.1	WMa,DSO
10	0.313	1.68E+01	5.08E+03	1.72E+03	0.339	0.125	51.4	WMa,DSO
11	0.46	2.44E+01	5.03E+03	1.74E+03	0.345	0.184	74.7	WMa,DSO
12	0.675	3.52E+01	4.92E+03	1.75E+03	0.356	0.27	108	WMa,DSO
13	0.991	4.99E+01	4.72E+03	1.76E+03	0.373	0.396	152	WMa,DSO
14	1.45	6.97E+01	4.45E+03	1.78E+03	0.399	0.582	213	WMa,DSO
15	2.14	9.45E+01	4.05E+03	1.79E+03	0.441	0.854	289	WMa,DSO
16	3.13	1.24E+02	3.53E+03	1.77E+03	0.502	1.25	378	WMa,DSO
17	4.6	1.56E+02	2.93E+03	1.72E+03	0.585	1.84	478	WMa,DSO
18	6.75	1.91E+02	2.33E+03	1.62E+03	0.695	2.7	585	WMa,DSO
19	9.9	2.28E+02	1.77E+03	1.48E+03	0.835	3.96	697	WMa,DSO
20	14.5	2.67E+02	1.30E+03	1.31E+03	1.01	5.82	817	WMa,DSO
21	21.3	3.11E+02	9.26E+02	1.13E+03	1.22	8.54	952	WMa,DSO
22	31.3	3.66E+02	6.59E+02	9.67E+02	1.47	12.5	1,120	WMa,DSO
23	45.9	4.43E+02	4.76E+02	8.39E+02	1.76	18.4	1,350	WMa,DSO
24	67.4	5.60E+02	3.53E+02	7.53E+02	2.13	27	1,710	WMa,DSO
25	99	7.40E+02	2.64E+02	6.99E+02	2.65	39.6	2,260	WMa,DSO

Data Series Information			Yield Test			
Name:			Ethan Pres 4%			
Number of Intervals:			3			
Application:			RHEOPLUS/32 V3.21 21003688-33024			
Device:			MCR301 SN80350866; FW3.41D110330; Slo			
Measuring Date/Time:			1/1/2007; 2:50 AM			
Measuring System:			PP25-SN13717; [d=0.5 mm]			
Accessories:			TU1=P-PTD200-SN80484899			
Interval:			1			
Number of Data Points:			0			
Time Setting:			2 Meas. Pts., Reject			
			Meas. Pt. Duration 0.5 min			
Measuring Profile:						
Shear Rate			d(gamma)/dt = 5 1/s			
Interval:			2			
Number of Data Points:			0			
Time Setting:			10 Meas. Pts., Reject			
			Meas. Pt. Duration 5 s			
Measuring Profile:						
Interval:			3			
Number of Data Points:			29			
Time Setting:			29 Meas. Pts., Reset Strain			
			Meas. Pt. Duration 5 s			
Measuring Profile:						
Shear Rate			d(gamma)/dt = 2 ... 100 1/s lin			

Meas. Pts.	Shear Rate	Shear Stre	Viscosity	Speed	Torque	Status
	[1/s]	[Pa]	[Pa·s]	[1/min]	[µNm]	[]
1	2	577	288	0.764	1,760	Dy_auto
2	5.5	804	146	2.1	2,460	Dy_auto
3	9	982	109	3.44	3,000	Dy_auto
4	12.5	1,140	91.4	4.78	3,490	Dy_auto
5	16	1,290	80.5	6.12	3,940	Dy_auto
6	19.5	1,420	73	7.46	4,350	Dy_auto
7	23	1,550	67.3	8.79	4,730	Dy_auto
8	26.5	1,660	62.6	10.1	5,070	Dy_auto
9	30	1,780	59.5	11.5	5,450	Dy_auto
10	33.5	1,900	56.7	12.8	5,800	Dy_auto
11	37	2,010	54.3	14.1	6,140	Dy_auto
12	40.5	2,120	52.3	15.5	6,470	Dy_auto
13	44	2,210	50.2	16.8	6,750	Dy_auto
14	47.5	2,320	48.8	18.2	7,080	Dy_auto
15	51	2,420	47.5	19.5	7,400	Dy_auto
16	54.5	2,520	46.3	20.8	7,710	Dy_auto
17	58	2,620	45.1	22.2	8,000	Dy_auto
18	61.5	2,710	44.1	23.5	8,290	Dy_auto
19	65	2,790	42.9	24.9	8,530	Dy_auto
20	68.5	2,890	42.2	26.2	8,830	Dy_auto
21	72	2,980	41.4	27.5	9,110	Dy_auto
22	75.5	3,070	40.7	28.9	9,400	Dy_auto
23	79	3,160	39.9	30.2	9,650	Dy_auto
24	82.5	3,240	39.2	31.5	9,900	Dy_auto
25	86	3,320	38.6	32.9	10,100	Dy_auto
26	89.5	3,410	38	34.2	10,400	Dy_auto
27	93	3,480	37.5	35.6	10,700	Dy_auto
28	96.5	3,560	36.9	36.9	10,900	Dy_auto
29	100	3,640	36.4	38.2	11,100	Dy_auto

Data Series Information			Constant Shear			
Name:			EthanPress 4%			
Sample:			text1			
Operator:			NoLogin			
Remarks:			text2			
Number of Intervals:			1			
Application:			RHEOPLUS/32 V3.21 21003688-33024			
Device:			MCR301 SN80350866; FW3.41D110330; Slo			
Measuring Date/Time:			1/1/2007; 2:26 AM			
Measuring System:			PP25-SN13717; [d=0.5 mm]			
Accessories:			TU1=P-PTD200-SN80484899			
Calculating Constants:						
- Norm. Csr [min/s]:			1.307468			
- Norm. Css [Pa/mNm]:			327.0941			
- Start Delay Time [s]:			3.891			
- Substance Density [rho]:			1,000			
- Measurement Type:			1			
- Motor Correction Factor:			1			
Interval:			1			
Number of Data Points:			20			
Time Setting:			20 Meas. Pts.			
			Meas. Pt. Duration 6 s			
Measuring Profile:						
Shear Rate			d(gamma)/dt = 50 1/s			

Meas. Pts.	Time	Viscosity	Shear Rate	Shear Stres	Torque	Status
	[s]	[Pa·s]	[1/s]	[Pa]	[mNm]	[]
1	6	49.7	50	2,480	7.59	Dy_auto
2	12	49.5	50	2,480	7.57	Dy_auto
3	18	49.4	50	2,470	7.56	Dy_auto
4	24	49.2	50	2,460	7.52	Dy_auto
5	30	49.4	50	2,470	7.54	Dy_auto
6	36	49.2	50	2,460	7.53	Dy_auto
7	42	49.4	50	2,470	7.54	Dy_auto
8	48	49.5	50	2,470	7.57	Dy_auto
9	54	49.5	50	2,470	7.56	Dy_auto
10	60	49.4	50	2,470	7.54	Dy_auto
11	66	49.4	50	2,470	7.55	Dy_auto
12	72	49.3	50	2,460	7.54	Dy_auto
13	78	49.2	50	2,460	7.52	Dy_auto
14	84	49.3	50	2,460	7.53	Dy_auto
15	90	49.4	50	2,470	7.55	Dy_auto
16	96	49.2	50	2,460	7.53	Dy_auto
17	102	49.2	50	2,460	7.52	Dy_auto
18	108	49.4	50	2,470	7.55	Dy_auto
19	114	49.4	50	2,470	7.55	Dy_auto
20	120	49.4	50	2,470	7.55	Dy_auto

Data Series Information			Hysteresis Loop				
Name:			Ethan Pres 4%				
Number of Intervals:			3				
Application:			RHEOPLUS/32 V3.21 21003688-33024				
Device:			MCR301 SN80350866; FW3.41D110330; Slot4				
Measuring Date/Time:			1/1/2007; 3:17 AM				
Measuring System:			PP25-SN13717; [d=0.5 mm]				
Accessories:			TU1=P-PTD200-SN80484899				
Calculating Constants:							
- Norm. Csr [min/s]:			1.307468				
- Norm. Css [Pa/mNm]:			327.0941				
- Start Delay Time [s]:			3.922				
- Substance Density [rho]:			1,000				
- Measurement Type:			1				
- Motor Correction Factor:			1				
Interval:			1				
Number of Data Points:			33				
Time Setting:			33 Meas. Pts.				
			Meas. Pt. Duration 5 s				
Measuring Profile:							
Shear Rate			d(gamma)/dt = 2 ... 600 1/s lin				
Meas. Pts.	Time	Shear Stre	Viscosity	Shear rate	Speed	Torque	Status
	[s]	[Pa]	[Pa·s]	1/s	[1/min]	[µNm]	[]
1	5	628	314	2	0.765	1,920	Dy_auto
2	10	1,510	72.9	20.71331	7.91	4,610	Dy_auto
3	15	2,120	53.8	39.4052	15.1	6,470	Dy_auto
4	20	2,630	45.4	57.92952	22.2	8,050	Dy_auto
5	25	3,120	40.6	76.84729	29.3	9,520	Dy_auto
6	30	3,560	37.3	95.44236	36.5	10,900	Dy_auto
7	35	3,970	34.8	114.0805	43.6	12,100	Dy_auto
8	40	4,360	32.8	132.9268	50.8	13,300	Dy_auto
9	45	4,730	31.2	151.6026	57.9	14,500	Dy_auto
10	50	5,080	29.9	169.8997	65.1	15,500	Dy_auto
11	55	5,400	28.6	188.8112	72.2	16,500	Dy_auto
12	60	5,730	27.6	207.6087	79.4	17,500	Dy_auto
13	65	6,020	26.6	226.3158	86.5	18,400	Dy_auto
14	70	6,310	25.8	244.5736	93.7	19,300	Dy_auto
15	75	6,560	24.9	263.4538	101	20,000	Dy_auto
16	80	6,810	24.1	282.5726	108	20,800	Dy_auto
17	85	7,050	23.4	301.2821	115	21,500	Dy_auto
18	90	7,290	22.8	319.7368	122	22,300	Dy_auto
19	95	7,490	22.1	338.914	129	22,900	Dy_auto
20	100	7,710	21.6	356.9444	137	23,600	Dy_auto
21	105	7,900	21	376.1905	144	24,100	Dy_auto
22	110	8,090	20.5	394.6341	151	24,700	Dy_auto
23	115	8,260	20	413	158	25,200	Dy_auto
24	120	8,420	19.5	431.7949	165	25,700	Dy_auto
25	125	8,610	19.1	450.7853	172	26,300	Dy_auto
26	130	8,750	18.6	470.4301	179	26,700	Dy_auto
27	135	8,870	18.2	487.3626	187	27,100	Dy_auto
28	140	9,020	17.8	506.7416	194	27,600	Dy_auto
29	145	9,140	17.4	525.2874	201	28,000	Dy_auto
30	150	9,250	17	544.1176	208	28,300	Dy_auto
31	155	9,390	16.7	562.2754	215	28,700	Dy_auto
32	160	9,500	16.3	582.8221	222	29,000	Dy_auto
33	165	9,590	16	599.375	230	29,300	Dy_auto
Interval:			2				
Number of Data Points:			4				
Time Setting:			4 Meas. Pts.				
			Meas. Pt. Duration 5 s				
Measuring Profile:							
Shear Rate			d(gamma)/dt = 600 1/s				
Meas. Pts.	Time	Shear Stre	Viscosity	Strain rate	Speed	Torque	Status
	[s]	[Pa]	[Pa·s]		[1/min]	[µNm]	[]
1	170	9,500	15.8	601.2658	229	29,000	Dy_auto
2	175	9,440	15.7	601.2739	229	28,800	Dy_auto
3	180	9,350	15.6	599.359	229	28,600	Dy_auto
4	185	9,290	15.5	599.3548	229	28,400	Dy_auto
Interval:			3				
Number of Data Points:			33				
Time Setting:			33 Meas. Pts., Reset Strain				
			Meas. Pt. Duration 5 s				
Measuring Profile:							
Shear Rate			d(gamma)/dt = 600 ... 2 1/s lin				
Meas. Pts.	Time	Shear Stre	Viscosity	strain rate	Speed	Torque	Status
	[s]	[Pa]	[Pa·s]		[1/min]	[µNm]	[]
1	190	9,250	15.4	600.6494	229	28,300	Dy_auto
2	195	9,070	15.6	581.4103	222	27,700	Dy_auto
3	200	8,880	15.8	562.0253	215	27,200	Dy_auto
4	205	8,710	16	544.375	208	26,600	Dy_auto
5	210	8,520	16.2	525.9259	201	26,000	Dy_auto
6	215	8,320	16.4	507.3171	194	25,400	Dy_auto
7	220	8,150	16.7	488.024	187	24,900	Dy_auto
8	225	7,960	17	468.2353	179	24,300	Dy_auto
9	230	7,780	17.3	449.711	172	23,800	Dy_auto
10	235	7,590	17.6	431.25	165	23,200	Dy_auto
11	240	7,390	17.9	412.8492	158	22,600	Dy_auto
12	245	7,200	18.2	395.6044	151	22,000	Dy_auto
13	250	7,000	18.6	376.3441	144	21,400	Dy_auto
14	255	6,790	19	357.3684	137	20,800	Dy_auto
15	260	6,600	19.5	338.4615	129	20,200	Dy_auto
16	265	6,390	20	319.5	122	19,500	Dy_auto
17	270	6,160	20.5	300.4878	115	18,800	Dy_auto
18	275	5,930	21	282.381	108	18,100	Dy_auto
19	280	5,700	21.6	263.8889	101	17,400	Dy_auto
20	285	5,470	22.3	245.2915	93.7	16,700	Dy_auto
21	290	5,210	23	226.5217	86.5	15,900	Dy_auto

APPENDIX D

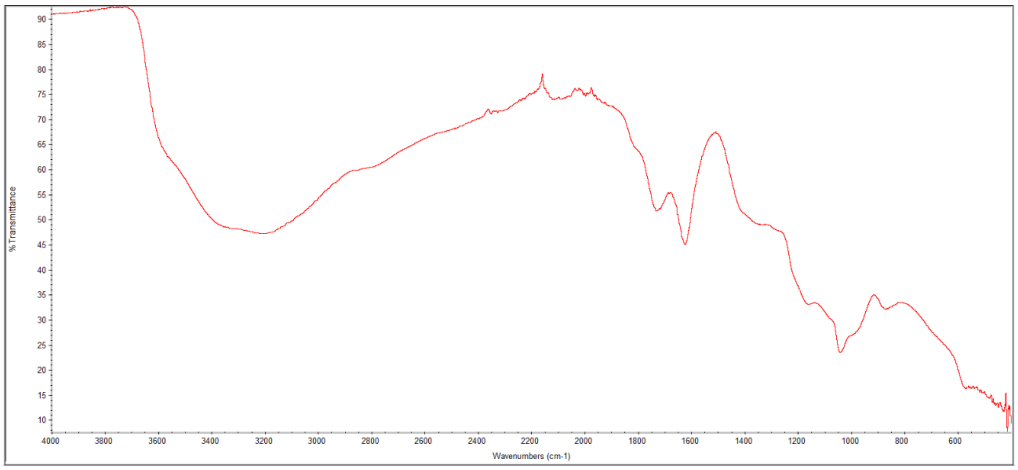

D1: GO FTIR spectrum

APPENDIX E

Sample XRD Data for RGO

*** Basic Data Process ***

Group : MsChew
Data : HRGO

Strongest 3 peaks

no.	peak no.	2Theta (deg)	d (A)	I/I1	FWHM (deg)	Intensity (Counts)	Integrated Int (Counts)
1	12	24.9200	3.57020	100	0.00000	63	0
2	13	25.8000	3.45039	95	0.00000	60	0
3	11	23.5400	3.77629	83	0.00000	52	0

Peak Data List

peak no.	2Theta (deg)	d (A)	I/I1	FWHM (deg)	Intensity (Counts)	Integrated Int (Counts)
1	11.1000	7.96469	3	0.24000	2	36
2	12.9650	6.82287	5	0.05000	3	22
3	16.3600	5.41384	6	0.16000	4	86
4	17.7950	4.98037	6	0.23000	4	109
5	18.5050	4.79085	11	0.15000	7	88
6	19.6000	4.52560	16	1.04000	10	586
7	20.9000	4.24695	33	1.44000	21	2607
8	22.4200	3.96234	57	0.00000	36	0
9	22.9600	3.87035	65	0.00000	41	0
10	23.1000	3.84721	68	0.00000	43	0
11	23.5400	3.77629	83	0.00000	52	0
12	24.9200	3.57020	100	0.00000	63	0
13	25.8000	3.45039	95	0.00000	60	0
14	26.6200	3.34594	83	0.00000	52	0
15	27.3400	3.25943	81	0.00000	51	0
16	28.3000	3.15101	65	0.00000	41	0
17	29.2200	3.05386	46	0.00000	29	0
18	30.0800	2.96848	27	0.00000	17	0
19	30.9200	2.88972	21	0.00000	13	0
20	31.4600	2.84124	22	0.68000	14	708
21	32.8350	2.72543	6	0.05000	4	29
22	35.3600	2.53638	3	0.04000	2	9
23	37.1200	2.42006	3	0.08000	2	15
24	37.8600	2.37444	6	0.12000	4	50
25	39.3450	2.28818	3	0.03000	2	11
26	40.6600	2.21716	10	0.12000	6	106
27	42.8300	2.10971	10	0.34000	6	161
28	43.9900	2.05673	19	0.66000	12	399
29	44.4000	2.03869	3	0.00000	2	0
30	44.7300	2.02441	11	0.14000	7	113
31	46.0500	1.96941	3	0.10000	2	19
32	47.0200	1.93102	6	0.12000	4	46
33	56.3200	1.63221	5	0.04000	3	23
34	57.7200	1.59591	3	0.04000	2	9
35	61.1100	1.51525	5	0.06000	3	32
36	62.6000	1.48272	5	0.08000	3	38
37	63.3000	1.46800	6	0.20000	4	65
38	64.3600	1.44635	37	0.56000	23	636
39	65.4600	1.42469	10	0.32000	6	150
40	66.4200	1.40640	6	0.28000	4	114
41	67.0450	1.39480	6	0.11000	4	73
42	68.5000	1.36868	3	0.04000	2	16
43	69.2300	1.35602	5	0.22000	3	113
44	70.7800	1.33008	3	0.24000	2	47
45	71.3600	1.32069	5	0.12000	3	39
46	75.7050	1.25532	3	0.17000	2	29
47	77.4850	1.23086	62	0.55000	39	1087

```
        ***  Basic Data Process  ***

# Data Infomation
          Group               : MsChew
          Data                : HRGO
          Sample Nmae         : Richardgraphene
          Comment             : Hydrazine Reduced Graphene Oxi
          Date & Time         : 12-04-14 11:04:33

# Measurement Condition
    X-ray tube
          target              : Cu
          voltage             : 40.0 (kV)
          current             : 30.0 (mA)
    Slits
          Auto Slit           : not Used
          divergence slit     :   1.00000 (deg)
          scatter slit        :   1.00000 (deg)
          receiving slit      :   0.30000(mm)
    Scanning
          drive axis          : Theta-2Theta
          scan range          :   10.0000 - 80.0000 (deg)
          scan mode           : Continuous Scan
          scan speed          :    6.0000 (deg/min)
          sampling pitch      :    0.0200 (deg)
          preset time         :    0.20 (sec)

# Data Process Condition
    Smoothing                 [ AUTO ]
          smoothing points    : 51
    B.G.Subtruction           [ AUTO ]
          sampling points     : 51
          repeat times        : 30
    Ka1-a2 Separate           [ MANUAL ]
          Ka1 a2 ratio        : 50 (%)
    Peak Search               [ AUTO ]
          differential points : 51
          FWHM threhold       : 0.050 (deg)
          intensity threhold  : 30 (par mil)
          FWHM ratio  (n-1)/n : 2
    System error Correction   [ NO ]
    Precise peak Correction   [ NO ]
```

APPENDIX F

F1: Varian Cary 100 UV-Vis spectrometer

F2: Nicolet iS 10 ATR FTIR spectrometer

F3: Shimadzu XRD-6000 diffractometer

F4: Renishaw inVia confocal Raman microscope (514nm laser)

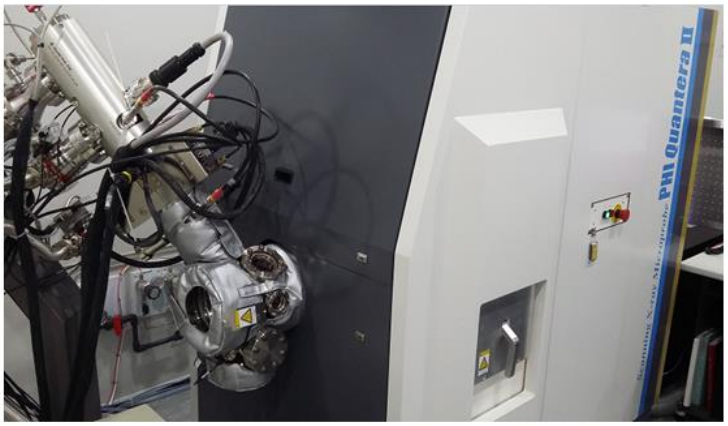

F5: ULVAC-PHI Quantera II Scanning XPS Microprobe

F6: JOEL JSM-6701F FESEM (left) FEI Technai G2 F20 HRTEM

APPENDIX G

Project Timeline: Feb 2014 to Jan 2015

Activities	Period (mths)	Feb '14 1	Mar 2	Apr 3	May 4	Jun 5	Jul 6	Aug 7	Sep 8	Oct 9	Nov 10	Dec 11	Jan '15 12
Phase 1: Chemical reduction of graphene oxide (GO) to graphene	4	X	X	X	X								
Phase 2: Dispersion stability of graphene in DGEBA polymer matrix / Isotropic Conductive Adhesives (ICAs)	4					X	X	X	X				
Phase 3: To measure the electrical conductivity of graphene based DGEBA polymer matrix / Isotropic Conductive Adhesives (ICAs)	4									X	X	X	X